Ph.D. Dissertation

Hári, László Róbert

Széchenyi István University
Győr
2022

Hári, László Róbert

Analysis and Simulation of Non-Stationarities in the Time-Frequency Domain of Road-Induced Vibrations

Ph.D. Dissertation

Supervisor: Prof. Dr. Földesi, Péter

Multidisciplinary Doctoral School of Technical Sciences
Széchenyi István University
Győr
2022

Abstract. The effect of road excitation can be felt in moving vehicles and every transported good are also exposed to this excitation. Products in transport must withstand for shorter-longer periods mechanical conditions for which they were not necessarily designed, if at all. To examine such cases, cost-effective numerical vibration simulations are performed for verification purposes and shaking tests in laboratories for verification and validation. While the success of virtual analysis, via finite element methods or multi-body dynamic systems, depends largely on the conditions considered by the modeling, results obtained in this way are biased in typically complex packaging systems due to unclear mechanical constraints and nonlinear behavior of cushioning materials. While in a model it is necessary to define geometric constraints, in reality, goods may be able to move, slip, jump, etc. The nonlinear behavior of the common packaging materials, e.g., corrugated paper, polyethylene, or polystyrene are also well-known factors. In contrast, the performance of vibration tests requires the use of expensive equipment, fortunately, many national and international standards support their implementation. In the application of such procedures, shaking tests often accompany the goal of packaging optimization, which seeks to balance between over- and under-protection of the cargo. These standards typically generate stochastic, normally distributed noises according to a given power spectral density function. Numerous studies have shown, based on measurements under real conditions, that the vibration acceleration of road-induced vibrations is stochastic, but their state is non-stationary and non-Gaussian. In this sense, therefore, even well-defined standards allow only an approximation of reality.

Absztrakt. Az útgerjesztés hatása érezhető a mozgó járművekben, ugyanígy minden szállított termék ki van téve ennek a dinamikus igénybevételnek. A szállított termékeknek rövidebb–hosszabb ideig olyan mechanikai körülményeknek kell ellenállniuk, amelyekre nem feltétlenül tervezték őket, ha egyáltalán tervezett termékekről van szó. Az ilyen esetek vizsgálatához költséghatékony numerikus szimulációkat végeznek ellenőrzés céljából és rázópróbákat verifikációs, validációs célokból. Bár a virtuális elemzés sikere nagymértékben függ a modellezés által figyelembe vett körülményektől, az így kapott eredmények a jellemzően összetett csomagolási rendszerek esetében torzítottak a nem egyértelmű mechanikai kényszerek és a csomagolóanyagok nemlineáris viselkedése miatt. Míg a modellben geometriai kényszereket kell meghatározni, a valóságban az áruk mozoghatnak, csúszhatnak, ugrálhatnak stb. Az elterjedt csomagolóanyagok, úgy mint a hullámpapír, a polietilén vagy a polisztirol nemlineáris viselkedése szintén jól ismert tényező. Ezzel szemben a rezgésvizsgálatok elvégzése drága berendezések használatát igényli, azonban nemzeti és nemzetközi szabványok támogatják ezek végrehajtását. Az ilyen eljárások alkalmazásakor a rázóvizsgálatok gyakran kísérik a csomagolás optimalizálásának célját, amely a túl- és alulvédelem közötti egyensúlyra törekszik. Ezek a szabványok jellemzően sztochasztikus, normális eloszlású zajokat generálnak egy adott teljesítményspektrum-sűrűség függvényében. Számos tanulmány, valós körülmények között végzett mérések alapján, kimutatta, hogy az útgerjesztés indukálta rezgésgyorsulás sztochasztikus, de állapotuk nem stacionárius és nem-gaussi eloszlású. Ebben az értelemben tehát a szabványok is csak a valóság egy közelítését teszik lehetővé.

Table of Contents

Frequent Abbreviations

3S Statistical spectrogram segmentation. 58

3SB 3S with Bonferroni correction. 75

ACF Auto-correlation function. 12

CF Crest factor. 24

CFT Continuous Fourier transform. 2

CN Condition negative. 77

CP Condition positive. 77

Cp Changepoint. 20

$\mathbf{Cp_c}$ Candidate changepoint. 63

CpD Changepoint detection. 11

CUSUM Cumulative sum scheme. 12

DFT Discrete Fourier transform. 2

EPMF Empirical probability mass function. 123

FD Frequency domain. 100

FN False negative. 78

FWER Family-wise error rate. 43

ibid. The source just cited. 1, 2

id. The author just cited. 4

KCDF Kernel cumulative distribution function. 123

MA Measurement and analysis. 7

MCF Moving crest factor. 24

MHT Multiple hypothesis testing. 39

NS Non-stationarity. 11

OTP One-tenth peak value. 24

PBSS Probability-based spectrogram synthesis. 91

pd Probability density. 100

PDF Probability density function. 27

POI Points of interest. 75

PR Prevalence. 77

PSD Power spectral density. 2

PVT Packaging vibration testing. 1

RA Reverse arrangements test. 11

RMS Root mean square. 20

ROC Receiver operating characteristic. 73

RVV Road vehicle vibration. 1

SLD Segment length distribution. 73

SNS Spectral non-stationarity. 11

SRS Significance reserve surface. 77

STFT Short-time Fourier transform. 13

TD Time domain. 92

TFD Time-frequency domain. 91

TN True negative. 79

TP True positive. 78

List of Figures

List of Tables

Chapter 1

Introduction

The current chapter positions the research and highlights possible use cases. In addition, some of the speculative ideas are supported by an earlier bibliographic study discussing disciplines involved in the simulation of road vehicle vibrations. Notably, the last table, Structure of the dissertation, in this chapter provides a compass for the current dissertation. It excerpts the following chapters with corresponding theses and publications of the author [1–10]. Apparently, the *sources just cited* (ibid.) also mean that the Bibliography begins with the author's publications.

1.1 Road vehicle vibrations

Every passenger, each transported cargo, and the vehicle transporting them are subjected to road-induced vibrations—or as commonly referred to Road vehicle vibrations (RVV). Simply put, a dynamic system is excited by the unevenness of road surfaces being traveled on. We primarily want to reduce these dynamic effects, so one looks for some form of active or passive vibration isolation. We are looking for this, because we want to ensure more comfortable conditions for passengers, postpone the fatigue failure of components, and keep the cargo intact until the destination.

There are analytical, numerical, and experimental approaches to tackle these problems, as suggested later by the bibliographic sample analysis in Table 1.1. In the design phase of products, analytical and numerical investigations are in the foreground to verify the effectiveness of vibration isolation solutions. Later, experimental approaches can be implemented during the prototyping, validating the design. It is, therefore, essential to use effective test signals, both in virtual and real forms. These are underlined mainly by the form of a mathematical model about RVV. Standardized methods cannot and should not be bypassed due to the expected conformity of production. However, at the same time, additional investigations might be implemented in a complementary fashion, increasing our trust in design, whether it can withstand real RVV.

A particular assumption in standardized Packaging vibration testing (PVT) protocols mathematically underpins these endeavors, summarized in Fig. 1.1. A measured RVV is most likely to incur transient events, e.g., at humps, bumps, rail-crossings, rough roads, etc. Also, the vibration intensity can vary at red-light stops, take-overs, and again on bumpy roads. Furthermore, harmonic excitation might be different near the wheels compared to cushioned surfaces. Many of the effects can be seen in Fig. 1.1.*a)* in the time domain. It is well-known that a signal, $x(t)$, can be investigated in the frequency domain, $X(\omega)$, by Fourier transformation. The Continuous Fourier transform (CFT) [11, p.7] is

$$X(\omega) = \int_{-\infty}^{+\infty} x(t)\mathrm{e}^{-\mathrm{i}\omega t}\mathrm{d}t, \tag{1.1}$$

with $\omega = 2\pi f$ denoting the angular frequency in [rad/sec]. Its discrete version, according to the *source just cited* (ibid., p.368), the Discrete Fourier transform (DFT) can be written as

$$X(k) = \sum_{n=0}^{N-1} x(n)\mathrm{e}^{-\mathrm{i}\frac{2\pi k}{N}n}. \tag{1.2}$$

The Power spectral density (PSD) [12]:

$$S(k) = \frac{1}{f_s N}|X(k)|^2 \tag{1.3}$$

of the presented measured signal shows the density of the power in the stochastic signal across a frequency range[1] in pane *c)*. A typical procedure is to join the PSD with a uniformly distributed random phase followed by inverse Fourier transformation to get a stochastic test signal back in the time domain, as in pane *b)*. As a quick check, one might subject the test signal again to Fourier transformation to confront the PSD curves and witness barely any difference in the frequency domain between the actual and test PSD. However, the signals in the time domain remained inherently different; namely, the test signal lacks any intensity-variations or transients. That is, the test signal is stationary and Gaussian, while real RVV is non-stationary and non-Gaussian. This controversy motivated many researchers in the last few decades to propose enhanced simulations, which mimic real-world phenomena in RVV.

1.2 Research on road vehicle vibrations

Not only PVT is fundamentally involved in studying RVV. The results from an earlier bibliographic sample analysis [1] are restated below to paint the broad spectrum of disciplines researching several aspects of the phenomena. In short, a sample consisting of 121 documents was drawn from the Scopus [14] database on March 6th, 2020, with the term constellation:

---

[1] The reader is referred to [12, 13] for a general treatment of spectrum scaling.

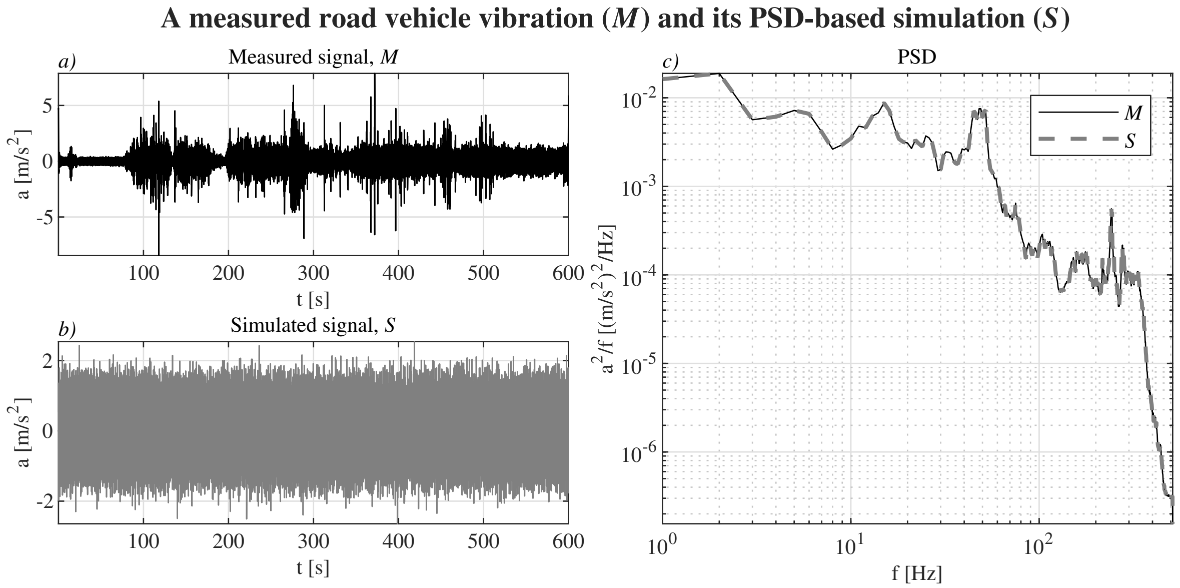

Figure 1.1: Comparison of real-world RVV with its PSD-based simulation. Pane *a)* shows the first 10 min of measurement A from Chapter 2, its Power spectral density in pane *c)* via *black solid* line. The PSD of the measured signal, *M*, had been used to simulate a random signal with uniformly distributed random phase in each iteration of the inverse Fourier transform, for 600 s in total. The resulted synthesized signal, *S*, can be seen in pane *b)* in the time domain, and its re-computed PSD in pane *c)* via *gray dashed* line. The overlap of the two PSD profiles are to be noted, only the PSD of the simulated signal resulted a 28-order smaller difference in the last bin.

```
packag* AND vibration AND road AND ( simulat* OR  test* )
```

applied in the "*article title, abstract and keywords*" search field. The VOSviewer (1.6.14) program [15] extracted the author- and index keywords. A threshold of two, on the minimum number of occurrences yielded 238 from 1229 index keywords. The Pajek64 (5.08) software [16] constructed an adjacency matrix, g, from a network file, analyzed further by

```
FindGraphCommunities[g]
```

built-in Wolfram Mathematica (12.0) [17] command producing six different clusters. In each sub-cluster, the most weighted vertices (terms) are surveyed in Table 1.1. Even from this heuristic and subjective analysis, many topics can be discovered.

Among others, they cover the serviceability statistics used in road profile surveys, which are also research topics. Since road unevenness contributes to road-induced vibration in vehicles, the Noise–vibration–harshness (NVH) circumstances of cars are typically investigated. A unique vertex was vehicles after roads and streets in the same cluster, showing that vehicles are highly discussed research objects. One could be interested in understanding the dynamic behavior of vehicles, traveling on uneven road surfaces, the riding qualities, or ride comfort. Most common techniques use Multibody simulation methods in the software package ADAMS. Examples of Finite element modeling (FEM) and numerical simulation of analytical models also can be found. A secondary meaning of packaging—as circuit packaging—is also present, straying not so far from the topic. Different electronic components are subjected to vibrations during transportation and their entire lifetime under operational conditions. In some cases, fatigue prediction of similar structures is another research area investigated via FEM. Regarding packages as transported goods, many publications describe the Measurement and Analysis (MA) of RVV. A general and widely used measure to quantify RVV is its description via Power spectral density function (PSD). Since MA is a cost-intensive and time-consuming process, virtual simulations also received emphasis, for which multibody dynamic simulation is an example. Operational modal analysis (OMA) might serve as an appealing methodological framework if one cannot measure the excitation signals. The other context of simulations conducted in laboratories has a root in standardized methods of packaging testing. Transported goods are therefore equipped with protective packaging to avoid damage. Examples of mathematical tools, such as machine learning algorithms, wavelet transform, or Hilbert–Huang-transform, are also presented.

1.3 Main path analysis

Another sample is drawn from the Core collection of Web of Science [54] on March 15th, 2020, with the same terms applied in the "*topic*" field [3]. The list yielded 46 publications embracing 28 years. The CitNetExplorer (1.0.0) [55] is used for direct citation analysis, which can use either external[2] or internal citation scores. Internal citation scores used herein, indicate the number of citations of a publication within the citation network. Afterwards, 26 records were identified as *core publications* by CitNetExplorer, being on view in Fig. 1.2. The direct citation network utilizing a timeline-based approach estimates the knowledge transfer in the discipline by the sample. Nooy et al. [56] describe the idea of citation networks as a system of channels transferring information. A junction (article) in this system refers to many other publications and likely synthesize knowledge, implying that knowledge flows through them. Such a main channel in the current sample is visualized in Fig. 1.3. The short thematic connections follow.

Fernando et al. (2019) [57] investigated the mechanical damage to bananas in transport. A discrepancy in PSD curves has been noticed from the ASTM testing standard. The *authors just cited* (id.) explained further that PSD peaks can be influenced by the suspension characteristics, referring to a previous study by Fernando

---

[2] External citation scores indicate the total number of citations of a publication. Citations from all publications in a bibliographic database are counted, including citations from publications outside the citation network being analyzed [55]

Table 1.1: Selected index keywords pro cluster. The reader is referred to [1] for further details of the analysis.

C.	Subject	Method	References
1	roads and streets	computer simulation	[18, 19]
		dynamic response	[20, 21]
		finite element model	[22]
		mathematical models	[19, 23]
		multibody simulations	[24]
		statistical (...)	[25, 26]
		structural analysis	[27]
		transfer function	[19, 28]
2	transportation	damage detection	[20]
		materials testing	[29]
		measurement and analysis	[30–33]
		spectral density (...)	[29–31, 34–36]
		operational modal analysis	[37]
		simulation	[18, 32, 37–40]
3	electronic components	fatigue damage, forecasting	[41]
		industry standards, reliability	[42]
4	pavements	monitoring, road tests	[43, 44]
		vibration measurement, (...)	[43–48]
5	protective packaging	artificial intelligence (...)	[49, 50]
		indexing (of information)	[51]
		wavelet (...)	[51]
		signal processing	[52]
6	customer satisfaction	modal analysis	[53]

C. cluster index
(...) synonyms or closely related terms

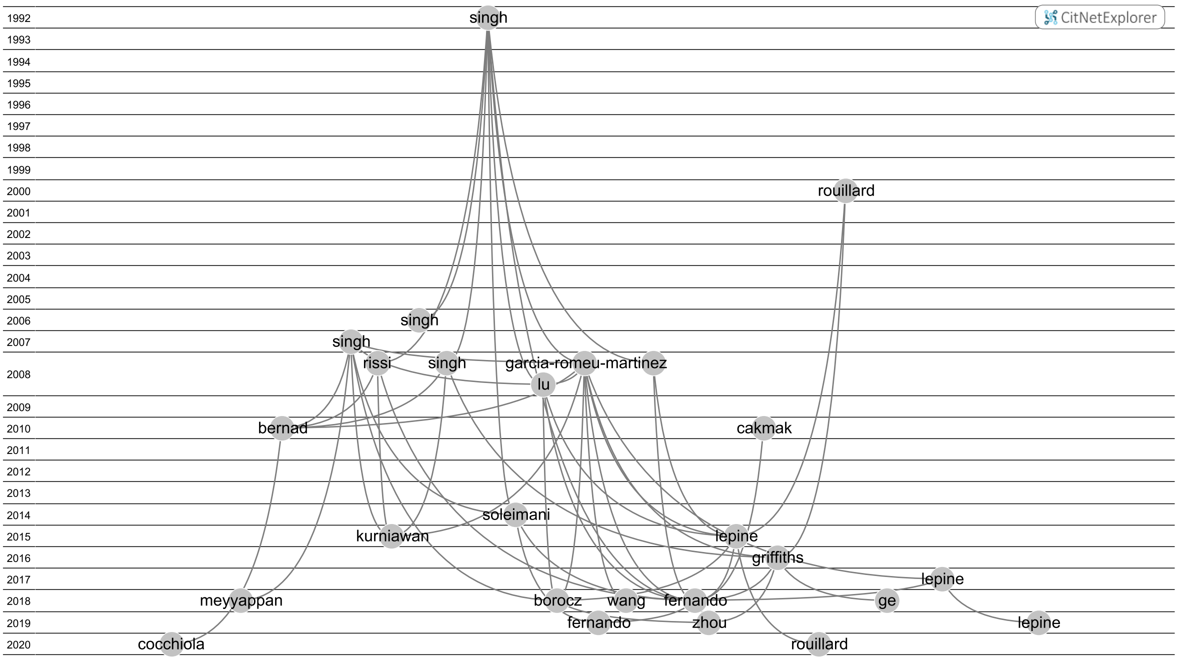

Figure 1.2: The timeline-based network of direct citations among core publications.

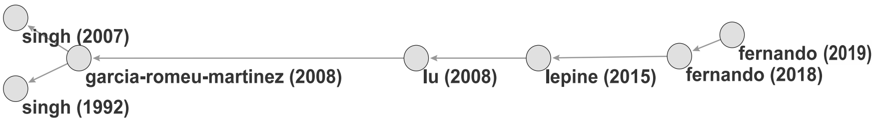

Figure 1.3: Main path analysis in the sample.

et al. (2018) [58]. Ibid. is a review article citing 113 records in order to discuss and identify the main factors of vibrations and their implications on fruit quality. Transient shocks are discussed as one of those critical factors, referring to Lepine et al. (2015) [38], who reviews simulations of PVT. At transient event detection, the method from Lu et al. (2008) [59] is mentioned among many others. Empirical studies are highlighted therein, e.g., from Garcia-Romeu-Martinez et al. (2008) [32], which published *Measurement and Analysis* (MA) results of truck transport in Spain as a function of payload, suspension, and speed. Studies from different countries concerning vibration level measurements are taken into account in the introduction, like a study conducted in India by Singh et al. (2007) [60] or in North America by Singh et al. (1992) [61]. Both cited references describe the measurement and analysis of vibrations of shipments during transport.

Packaging vibration testing has its roots in measurement and analysis of road vehicle vibrations. Studies led to the recognition of RVV being non-stationary and non-Gaussian stochastic processes, still many available vibration testing standards use average PSD profiles leading to stationary Gaussian simulations. The limitation of prior available testing standards had been addressed in different studies; hence, new simulation methods had been established. From this indefinite point, the discipline has reserved the two methodologies, such as RVV Measurement and Analysis and RVV Synthesis.

1.4 Key factors and implications

One of the main factors is the adequate modeling of the excitation signal when examining or designing such dynamic systems as above. Thus, it is advisable to take on *in situ* measurements from specific roads in case of packaging optimization or to derive a representative sample from many different routes when designing for unspecific travels. The series of measurements may then be successfully fed to the following algorithms, which are inherently data-driven solutions. It is also often a good practice to verify the system in question already in the design phase. Once a tangible product or prototype is available, the system should also be validated, e.g., in a shaker laboratory.

Neither the current work can offer guarantees into the future, some speculative ideas might be worth mentioning here. The broad implications of ongoing research in studying RVV can be fruitful in different scenarios. It may be aligned with the goals of packaging material optimization or inherited in passenger comfort studies, to name a few of the author's favorite ideas. Hopefully, those endeavors will successfully contribute to more cost-efficient solutions, considering the narrowing energy and material resources.

As acceleration measurement becomes sufficiently cost-effective, dynamic monitoring systems will be created. Such systems, for instance hypothetically mandated in specific transportation scenarios, could clarify the responsibility for inter-transport damages.

Also, the route- or trajectory optimization can be complemented by evidence-based aspects of road conditions. Perhaps, the most forward-pointing speculation builds upon a possible big data system, where vibration data logging would be the default configuration of future vehicles. At that point, the collected data would provide a unified picture of the state of the national road networks, which would support the related federal economic investments in road renovations.

1.5 Summary

The dissertation presents segmentation and simulation of road-induced vibration signals through realizations of such stochastic processes to assess the spectral descriptors and to offer an enhanced alternative simulation method beyond standard procedures. In this sense, the research object is the Road vehicle vibration (RVV) aimed at defining a novel algorithm for vibration testing. However, this motivation holds other use-cases, as well. Beyond a direct dedication to Packaging vibration testing (PVT), the following methods might also be beneficially implemented as virtual excitation signals in the numerical analysis of the dynamic behaviors of road vehicles. Implicitly, fatigue simulations could also benefit from current studies. The co-occurrence of author- and index keywords from a bibliographic sample of 121 entries concluded [1] that various aspects of the pavement–vehicle–package systems can be investigated. While this cannot supply an exhaustive list, the concerned topics can be viewed from a higher perspective. While this does not contribute to scientific claims, it offers the possibility to form the motivating Proposition behind the dissertation.

Proposition. Based on the heterogeneous research topics of road vehicle vibration studies, the lifetime of installed vehicle components and their design to take on loads from amplitude- and frequency modulated excitation, as well as, the avoidance of aversion in passenger comfort, and the vibration protection of transported loads are central research subjects. Instead of studying the individual subsystems of the road–vehicle–cargo system, it can be imperative to establish a standardized methodology, since the final source of excitation is itself the road-induced vibration. ■ *Ref.*: [1, 3]

1.6 Dissertation structure

Current dissertation is excerpted in Table 1.2. *Segmentation* and *Simulation* are discussed in two different chapters since the introduced methods are designed in a modular manner, i.e., a simulation can use any of the segmentation methods. Conversely, the segmentation techniques can be used independently of simulation for their own purpose.

Table 1.2: Structure of the dissertation.

Chapter	**Objective**	**Methodology**	**T.**[a]	**P.**[b]
Introduction	Accommodation of current work in a broad landscape.	Mathematical motivation is followed by bibliographic analysis.	0.	[1, 3]
Spectral non-stationarity	Technical introduction and discussion on non-stationarity in the frequency domain.	Spectral moments of the short-time Fourier transform of three measurements are segmented by a CUSUM approach. Reverse arrangements tests of spectral moments supply additional support on the non-stationary nature.	1.	[4]
Analysis of prior algorithms	Analysis of prior event detection algorithms in packaging vibration testing.	Previously introduced event detection algorithms in packaging vibration testing are analyzed by process flowcharts.	2.	[5]
Development of segmentations	Establishment of Statistical spectrogram segmentation.	Time-frequency domain of road vehicle vibration is segmented by unpaired- and paired *t*-tests, as well as the CUSUM approach.	3.	[6, 7, 9]
Calibration of segmentations	Verification of the segmentation methods.	The calibration utilizes Receiver operating characteristics accompanied by Segment length distributions.	4.	[8]
Simulation	Development and verification of the simulation method	Segmentation and simulation are introduced in two loops: first, one measurement is simulated three times; second, three series are simulated one times.	5.	[10]
Clustering spectrums	An approach for hierarchical clustering of RVV spectrums.	Different thresholds for the distribution of distances from dendrograms are used to find the separating heights and a new cluster validation index is proposed.	6.	[2]
Summary	Reiteration on main thoughts and milestones.	A cohesive review depicts the path among theses.	-	-

[a] Theses in English, where 0 denotes the Proposition above.

[b] Corresponding publications.

Chapter 2

Spectral non-stationarity

Road-induced vibrations are in the scope of various environmental testing protocols, e.g., for Packaging vibration testing (PVT) purposes. This field matures with well-understood methods for analyzing amplitude-type non-stationarity (NS) in Road vehicle vibrations (RVV). Albeit frequency-type NS is well known, only suggestions are provided for processing the phenomenon in PVT. Both types of NS can be jointly investigated in the time-frequency domain; thus, the current study initiates the investigation of Spectral non-stationarities (SNS) in RVV. Three vibration series were recorded from 118 km traveled distance supplying an empirical insight.

2.1 Introduction

Statistics, econometrics, and acoustics are typically concerned with the challenge of time series' stationarity. It may be impractical to indulge in a comprehensive listing; instead, the current chapter discusses the results in the context of Packaging vibration testing. The discipline of PVT is fundamentally involved with non-stationarity present in RVV. Scholars have presented various methods accounting for amplitude-type NS. Albeit the phenomenon of frequency-type or spectral non-stationarities is pointed out, mostly suggestions are provided. Therefore, the current article presents an empirical validation of the presence of SNS in RVV obtained by three measurements in a passenger car, such as

$$\begin{cases} H_0 : \text{SNS does not exist in RVV;} \\ H_A : \text{SNS exist in RVV.} \end{cases} \tag{2.1}$$

It is assumed under H_0 that spectral moments of the measured RVV are stationary over time. The reverse arrangements test (RA) is used to assess the null hypothesis, and the study is augmented by changepoint detection (CpD).

A stochastic process is said to be stationary in the strong sense if its unconditional joint probability distribution does not change when shifted in time [62]. On the other hand, the exact process is said to be stationary in the wide sense if its mean and auto-covariance do not vary with respect to time. Simply put, if the mean and Auto-correlation function (ACF) of a stochastic process is time-invariant, the process is weakly stationary; and the process is strictly stationary if all moments are time-independent [63, p.74].

Parametric models frequently used for stationarity testing cover: the augmented Dickey and Fuller test for a unit root [64], the KPSS test [65], the Leybourne and McCabe stationarity test [66] and the Phillips and Perron test for one unit root [67]. The above tests, however, rely on model assumptions in a form of auto-regressive integrated moving average (ARIMA) processes. Therefore, in lack of a specific model to be evaluated, one might turn toward alternative solutions. A semi-parametric analysis is the variance ratio (VR) test for random walk, originally suggested in [68]. The VR tests the random walk hypothesis against stationary alternatives [69].

Non-parametric methods also devoted for stationarity problems include the runs test [70, p.52], the reverse arrangements (RA) test [11, p.97] and the modified RA test [71]. The three non-parametric tests can show inconsistencies, as discussed later.

The current study suggests the changepoint detection in spectral descriptors from the time-frequency domain of recordings to strengthen the investigation of stationarity. Control charts introduced in [72] are typical examples in manufacturing to monitor and control capable processes. Statistical process control (SPC) can be enhanced by CpD. While SPC can be updated at each incoming sample, CpD can be performed once all data points are collected. SPC detects abnormal observations and major changes, but CpD can also find minor changes and controls the change-wise error rate [73].

The establishment of CpD can be contributed to Page [74–76], who developed a test for a change in a parameter occurring at an unknown point. The setup of the problem consists of independent observations x_n for $n = 1, \dots, N$ ordered in time, incurring a changepoint at $n = m$. The procedure investigates whether all the observations are from the same population with the distribution function $F(x|\theta)$, i.e., under the alternative $x_{n=1,\dots,m}$ are from $F(x|\theta)$ and $x_{n=m+1,\dots,N}$ come from $F(x|\theta')(\theta = \theta')$. The cumulative sum (CUSUM) schemes are further discussed in Section 2.2.5, which are commonly sharpened by resampling methods. In short, the probability of the changepoint's actual existence can be assessed by a corresponding p-value from a resampling technique.

2.2 Materials and methods

The current section presents first the details of experiments and the pre-processing of the recorded vibration series. It is accompanied by introducing the considered spectral descriptors, the RA test, and the CpD—the latter including a permutation resampling method.

2.2.1 Experimental

Three measurements are recorded on routes A,B,C reported in Fig. 2.1. Capitals denote the experiments, and lower-case letters signify sub-figures throughout the chapter. Common factors are the passenger car (Suzuki Swift Sedan 1.3 GLX year 2002), the personnel (one chauffeur and one experimenter $\sim$ 150 kg in total), the GPS position recorder (Columbus P1, $f_s = 1$ Hz), the DC MEMS accelerometer (Recovib Tiny 15G, $f_s = 1024$ Hz, effective bandwidth 250 Hz). The accelerometer's placements are: A) in the coin toss attached with thick double-sided tape, B) on the right-hand side upper plane of the cockpit attached with thin double-sided tape, and C) in the trunk on the right-hand side attached to the chassis with magnets. The traveled distances are: A) 35.50, B) 29.88, and C) 52.53 km, respectively.

2.2.2 Preprocessing

The current method relies on the short-time Fourier transform (STFT) with one-sec non-overlapping Boxcar windows yielding equidistant 1 Hz and 1 sec resolution. The power spectral densities (PSD) in Fig. 2.1.*d)* are given up to the Nyquist frequencies. In other cases, STFT spectrograms are band-limited to [1, 250] Hz with an ideal numerical band-pass filter. Fig. 2.2 depict only [1,175] Hz intervals for further readability.

2.2.3 Spectral moments

The first four spectral moments are considered for RA test and CpD. These are signified by μ_i for $i = 1, 2, 3, 4$, respectively the spectral centroid, -spread, -skewness and -kurtosis [77, p.371, 281, 299, 317] respectively. The frequency-weighted sum of s_k spectral values normalized by the unweighted sum is the spectral centroid:

$$\mu_1 = \frac{\sum_{k=b_1}^{b_2} f_k s_k}{\sum_{k=b_1}^{b_2} s_k}, \tag{2.2}$$

where f_k is the frequency in Hz corresponding to bin k. The spectral centroid is calculated between the band borders b_1 and b_2. It is used in music interpretation and genre identification, as a brightness measure [78]. The spectral spread is defined as the standard deviation across the spectral centroid which stands for the spectrum's instantaneous bandwidth

$$\mu_2 = \sqrt{\frac{\sum_{k=b_1}^{b_2} (f_k - \mu_1)^2 s_k}{\sum_{k=b_1}^{b_2} s_k}}, \tag{2.3}$$

showing the most dominant tone. The spread, widens as the tones diverge and narrows as they converge.

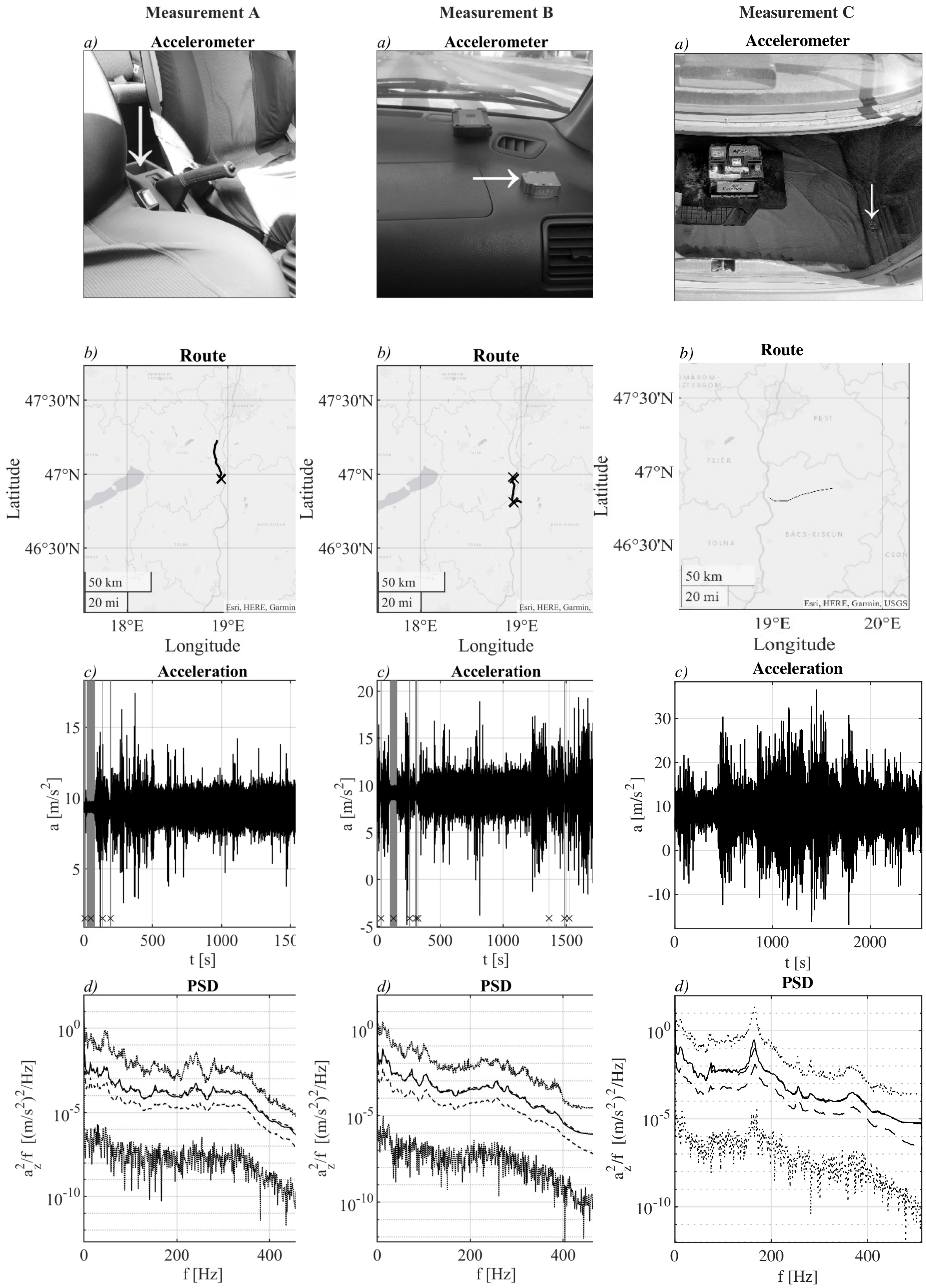

Figure 2.1: A,B,C measurements per columns. Each measurement is accompanied per rows by *a)* place of accelerometer, *b)* GPS coordinates, stops marked by (×), *c)* vertical acceleration with symbolization of stops (× on *gray intervals*), and *e)* power spectral density: average (*solid*), 25th, 75th percentiles (*dashed*), max-min envelopes (*dotted*) over time. Note that 75th percentiles are likely to overlap with averages.

Spectral skewness is a metric that calculates symmetry around the centroid

$$\mu_3 = \frac{\sum_{k=b_1}^{b_2} (f_k - \mu_1)^3 s_k}{\mu_2^3 \sum_{k=b_1}^{b_2} s_k}. \tag{2.4}$$

Spectral skewness can discern the articulation point [34], showing the relative frequency of higher and lower harmonics in harmonic signals. The spectral kurtosis is a measure of the spectrum's flatness (or non-Gaussianity) around the centroid

$$\mu_4 = \frac{\sum_{k=b_1}^{b_2} (f_k - \mu_1)^4 s_k}{\mu_2^4 \sum_{k=b_1}^{b_2} s_k}, \tag{2.5}$$

indicating the peakedness of a spectrum. Therefore, an increasing white noise on tonal components yield a decreasing kurtosis, indicating a spectrum with less peaky character. Other frequency domain measures also exists like entropy, flatness, crest, flux, slope, decrease and roll-off point, discussed in [4]. However, let us note that higher order moments above the 4th moment are not given.

2.2.4 Reverse arrangements test

The RA test [11, p.97] is a non-parametric test, not assuming any underlying distribution, trend, or model. It evaluates a sequence of ordered data obtained from independent observations of the same random variable by deciding if the observations undergo a significant trend. The n-th reverse arrangement A_n is the number of times that $x_n > x_m$ for $n < m$ given a sequence of N observed values of a random variable, x_n for $n = 1, \ldots, N$. Then, A_n is summed to get the total number of reverse arrangements, $A = \sum_{n=1}^{N-1} A_n$. Given x_n is a collection of N independent observations of the same random variable, A is a random variable with the mean of

$$\mu_A = N\frac{N-1}{4}, \tag{2.6}$$

and variance

$$\sigma_A^2 = N(N-1)\frac{2N+5}{72}. \tag{2.7}$$

Then, A is expected to be above or below of μ_A when an increasing or a decreasing trend underlies the data, respectively. Albeit tabulated values of A is available, the tendency to normality is extremely rapid for $N \geq 14$ and

$$z = \frac{A - \mu_A}{\sigma_A} \tag{2.8}$$

approximately follows the standard normal distribution.
The z-value is used to reject H_0, thus the Eq. 2.1 can be written as

$$\begin{cases} H_0 : \mu_A = 0; \\ H_A : \mu_A \neq 0. \end{cases} \tag{2.9}$$

2.2.5 Changepoint detection

The method is individually set up in Matlab based on the work presented in [73]. The CpD is applied here on $\mathbf{x} = x_n = \mu_i$, such as:

$$S_n = \sum_{n=1}^{N} (x_n - \overline{\overline{\mathbf{x}}}) \tag{2.10}$$

where

$$\overline{\overline{\mathbf{x}}} = \frac{1}{N} \sum_{n=1}^{N} x_n, \tag{2.11}$$

that is the cumulative sum of differences between x_n and its total mean, $\overline{\overline{\mathbf{x}}}$, is computed. The extremum $\hat{S}_n$ yields a candidate changepoint at $\mu_{i,m}$ and the permutation loop decides upon the significance[1]. Each reference set comprises $R = 10^4$ permutation (resampling without replacement) and an $\alpha = 0.05$ significance limit is chosen for demarcation. A difference compared to [73] emanates from using the same S_n statistic in Eq. 2.10 at each permutation, instead of $\max S_n - \min S_n$. Given a significant changepoint μ_{i,m^*}, the series μ_i is divided into two parts: $n = 1, \ldots, m^*$ and $m^* + 1, \ldots, N$. Both sections are submitted to the same changepoint-detection algorithm until no more changepoint is found.

The cardinality of significant changepoints per the i-th spectral moment is symbolized by $\gamma_i = \#\{m^*\}$. The total number of unique significant changepoints for the set of μ_i is

$$\Gamma = \# \left\{ \bigcup_{i=1}^{4} \gamma_i \right\}. \tag{2.12}$$

Finally, the temporal density of changepoints is proposed:

$$\Gamma^\circ = \frac{\Gamma}{T}, \tag{2.13}$$

where T is the length of the recording. The following reporting scheme is recommended for RVV analysis accommodating the method in large-scale experiments and cross-validation studies:

$$\Gamma^\circ = \Gamma^\circ(\mu_\mathrm{i}, R, \alpha, \Delta t, \Delta f)\,[1/s]\,, \tag{2.14}$$

---

[1] The interested reader is referred to [79] for a comprehensive overview of resampling methods.

with $\Delta t, \Delta f$ time- and frequency resolution of the DFT-based spectrogram, respectively.

2.3 Results

The results supported the investigated alternative hypothesis in Eq. 2.1. The spectral moments $\mu_i^{(j)}$ for $i = 1, 2, 3, 4$ in measurements $j = A, B, C$ show at least cv $\left(\mu_2^C\right) = 5.41\%$ and at most cv $\left(\mu_3^C\right) = -461.32\%$ coefficient of variations. The null hypothesis of stationarity in Eq. 2.9 is rejected in favor of the alternative hypothesis by the RA test at the $\alpha = 0.05$ significance level in all cases but μ_1^A, μ_3^A, and μ_4^C. Therefore, measurements A,B,C can undergo spectral non-stationarity since at least one of four spectral moments per experiment is non-stationary. It is worth recalling that SNS is present regardless of the accelerometer's fixture and position.

While RA tests confirmed SNS in most cases, the CpD delivers further insights into the non-stationarity since no changepoints would be expected under H_0. First, let us not consider the spatial- or temporal distribution of changepoints in Fig. 2.1. Then, 2.65, 3.35, 2.46 [1/km] unique changepoints per kilometer for routes A,B,C show that roughly each traveled kilometer incurred two to three different spectral characteristics, on average.

Here, $\Gamma^{\circ}(A) = 5.44 \cdot 10^{-2}$, $\Gamma^{\circ}(B) = 5.29 \cdot 10^{-2}$ and $\Gamma^{\circ}(C) = 5.11 \cdot 10^{-2}$ 1/s for $(\{\mu_1, \mu_2, \mu_3, \mu_4\}, R = 10^4, \alpha = 0.05, \Delta t = 1\text{s}, \Delta f = 1\text{Hz})$ are found.

Changepoints' temporal density is lower than spatial density [1/km]. Still, vibration testing protocols are also extended, e.g., "*the exposure duration for common carrier/truck is 60 minutes per 1609 kilometers* (...) *of road travel (per axis)*" [80, p.514.8C-16].

Results from Table 2.1 signified by (*) imply, that RA test did not yield test statistics extreme enough, thus it failed to reject H_0. However, CpD found several changepoints, considered significant. The three instances marked by (*) are further discussed in the next section.

2.4 Discussion

In principle, one could choose only the spectral centroid for changepoint detection, since $\mu_2 = f(\mu_1)$, $\mu_3 = g(\mu_1)$, and $\mu_4 = h(\mu_1)$.). However, it is interesting that a change in μ_1 does not imply changes in other descriptors and vice versa. Albeit the necessary number of spectral descriptors remains out of the scope, it is recommended to consider higher-order moments simultaneously.

Slight inconsistencies between the RA test and the CpD are pointed out by (*). Namely, changepoints have been found in series deemed stationary in the RA test. Beck et al. [81] showed that the runs test, RA test, and modified RA test showed false negative and false positive results.

Table 2.1: Statistics of the spectral moments and their coefficients of variation, reverse arrangements tests, changepoints, unique changepoints, and temporal density of changepoints of measurements A,B,C.

	Results	**A**	**B**	**C**
(a)	$\mu_1 \pm \sigma(\mu_1)$	83.06 ± 10.36	80.52 ± 12.30	105.77 ± 14.11
	$\mu_2 \pm \sigma(\mu_2)$	72.68 ± 4.62	72.31 ± 3.94	69.82 ± 3.77
	$\mu_3 \pm \sigma(\mu_3)$	0.85 ± 0.24	0.87 ± 0.28	-0.07 ± 0.34
	$\mu_4 \pm \sigma(\mu_4)$	2.51 ± 0.62	2.63 ± 0.62	1.79 ± 0.31
(b)	cv_1	12.47	15.28	13.34
	cv_2	6.36	5.45	5.41
	cv_3	28.86	32.24	-461.32
	cv_4	24.77	23.44	17.63
(c)	$z_1(p)\,[H]$	(*) 0.17 (0.87) [0]	16.85 (0.00) [1]	-10.67 (0.00) [1]
	$z_2(p)\,[H]$	-11.37 (0.00) [1]	7.59 (0.00) [1]	3.75 (0.00) [1]
	$z_3(p)\,[H]$	(*) 1.91 (0.06) [0]	-17.21 (0.00) [1]	9.45 (0.00) [1]
	$z_4(p)\,[H]$	3.20 (0.00) [1]	-15.16 (0.00) [1]	(*) -1.14 (0.25) [0]
(d)	γ_1	38	35	49
	γ_2	29	35	49
	γ_3	35	42	51
	γ_4	33	41	38
(e)	Γ	94	100	129
(f)	Γ°	$5.44 \cdot 10^{-2}$	$5.29 \cdot 10^{-2}$	$5.11 \cdot 10^{-2}$

(a) mean ± standard deviation [m/s^2].
(b) coefficient of variation $\mathrm{cv}_\mathrm{i}\,[\%] = 100 \cdot \sigma(\mu_i)/\overline{\mu_i}$
(c) z-value (two tails significance) $[= 0 \text{ if } H_0; = 1 \text{ if } H_A]$ at $\alpha = 0.05$.
(d) significant changepoints at $\alpha = 0.05$.
(e) number of unique changepoints in $\{\mu_1, \mu_2, \mu_3, \mu_4\}$.
(f) degree of non-stationarity [1/s].
(*) Non-significant RA tests, further discussed in Fig. 2.3.

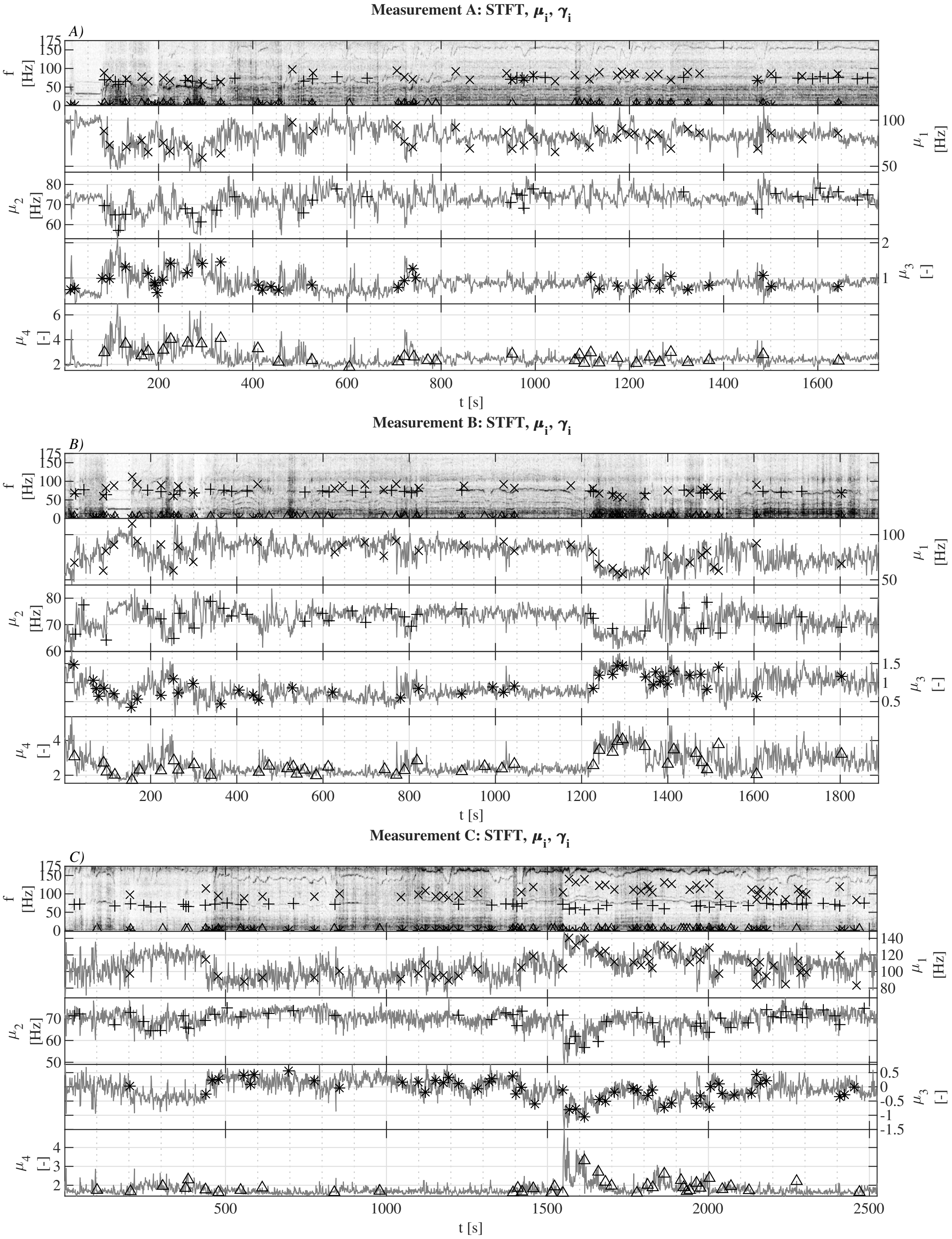

Measurement A: STFT, μ_i, γ_i

Measurement B: STFT, μ_i, γ_i

Measurement C: STFT, μ_i, γ_i

Figure 2.2: Short-time Fourier (STFT) transform of measurements A,B,C. Below each STFT, spectral moments μ_i for $i = 1, 2, 3, 4$ corresponding to the spectral centroid, -spread, -skewness, and -kurtosis are plotted. The first panes also show the changepoints by different symbols.

Id. deduced that these tests are not always reliable for stationarity testing. The hypothesized reason was that the above three trials had been primarily designed for checking randomness under H_0 or deciding the existence of an underlying trend under H_A. Therefore, it is also possible in the current experiment, that results marked by (*) are false negatives since changepoints are present. Furthermore, the auto-correlation of the corresponding spectral moments shows variation with respect to time, as presented in Fig. 2.3.

Rouillard [82] presented his approach by using runs tests on the moving Root mean square (RMS) series from RVV measurements, which can detect only amplitude-type NS. However, the window width should be justified if one wishes to use moving statistics. In contrast, the current method analyzed the time-frequency domain of measurements, which can address amplitude- and frequency-type NS at the same time. Id. presented his solution based on the runs test. Stationary Gaussian vibrations were also subjected to the runs test as falsification trials, which produced true negative results in three of four cases of different moving RMS time histories of stationary signals. However, a similar falsification trial by Beck et al. [81] produced consecutively false positives in all their six stationary cases.

This paragraph takes the occasion and offers future speculations on the usefulness of segments. If every changepoint is accepted as it is, segments can be defined in a series of μ_i since each (Cp) indicates a border. After that, the distribution of spectrally homogeneous segment lengths may be studied. In parallel, each segment can be described by an average DFT or PSD profile. Therefore, given a hypothetic database of many segments from several journeys, the segment length distribution joint with typical spectral shapes can lead to *spectral non-stationary* vibration simulations.

2.5 Conclusion

This chapter presented three experiments investigating the hypothesis of whether SNS exists in RVV. The RA tests showed good confirmation of SNS corresponding to the four spectral moments derived from STFT. Auto-correlation functions further discussed the three cases of stationarity. In conjunction, CpD found significant changepoints in the series of each investigated spectral descriptors of the measurements. Besides, an SNS metric was proposed for RVV analysis in the long term.

It was concluded that RVV could undergo changes in STFT because changepoints are present in the first four spectral moments. Since PSD-based vibration simulations are stationary in time- and in the frequency domain, the broad implication of current research leads to the necessity of spectrally non-stationary simulations—whereby amplitude-type NS has been an active field of study in PVT as of date. These findings might supply a potential contribution to a mechanism for further non-stationary vibration simulations.

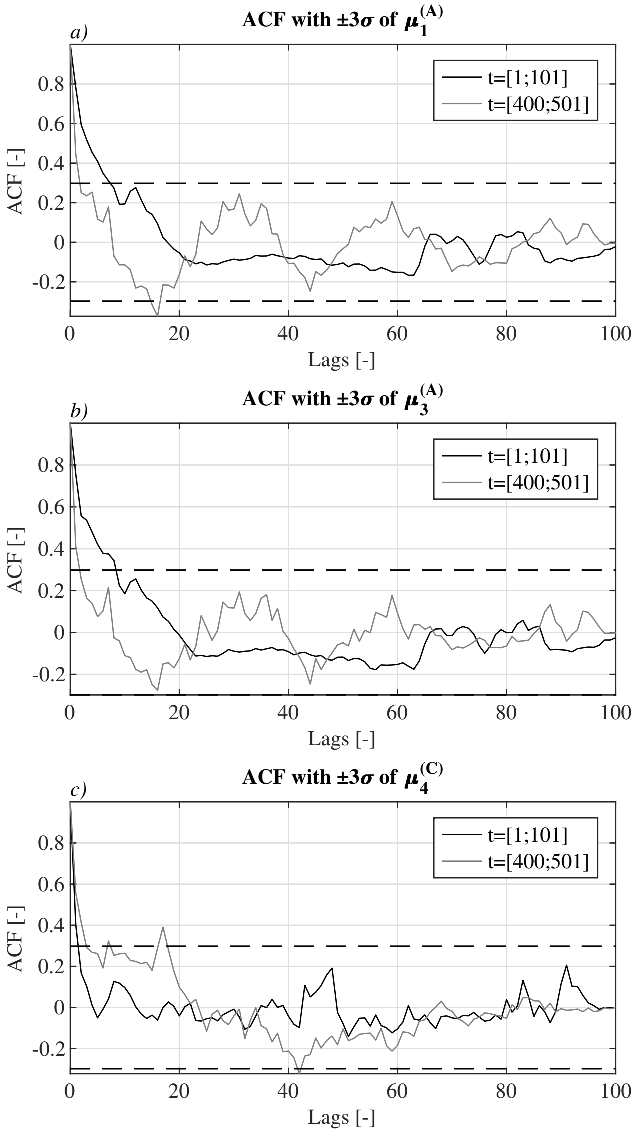

Figure 2.3: Examples of changing Auto-correlation functions (ACF) (*solid*) showing confidence intervals estimated by ± three standard deviations (*dashed*): Pane *a)* spectral centroid of short-time Fourier transform (STFT) from measurement A; pane *b)* spectral skewness of STFT from measurement A; and pane *c)* spectral kurtosis of STFT from measurement C. Note, how ACF changes at different intervals.

Thesis 1. I have presented that the shape of amplitude spectrum function is not constant over time, due to the variation of the spectral shape manifested in the time-frequency domain, which is due to transient events, and harmonic excitation in accordance with the driving speed, compared to the spectral shapes of the steady-state vibration intervals. The changes, therefore, occur locally on the time or space horizon of the journeys, thus, for practical reasons it is reasonable to separate them into homogeneous intervals. ■ *Ref.*: [4]

Chapter 3

Analysis of prior algorithms

Bibliographic analysis can offer an upper perspective on a discipline. In order to understand the physical–mathematical structure behind the bibliographic landscapes, the analytic review of proposed methodologies is inevitable. This chapter reviews in the first place the columns of changepoint detection algorithms applied before non-stationary simulations in PVT. Whereby possible, process flow diagrams are reproduced. The reader can see this evolution through the collocations of time-, frequency-, and time-frequency domain approaches; finally, the contemporary mixed methods are highlighted. Each method is queued along: (i) *introduction*, (ii) *discussion*, and (iii) *summary.*

3.1 Segmentation in time domain

Let $x[i]$ denote the i-th element of a realization of the $x(t)$ continuous process sampled with an equidistant sampling, Δt, on $T = N\Delta t$ period for $i = 1, 2, ..., N$. Segmentation aims at finding changepoints within $x[i]$, such that sections can be considered homogeneous with respect to a certain criterion in-between and different from adjacent sections. The following methods are established on various measures of $x(t)$ considering the time domain characteristics.

3.1.1 Moving statistics

(i) Different moving statistics can be evaluated in windows sliding over the time domain. Common approaches are the moving root mean square, -crest factor, and -kurtosis [83]. If a predictor reaches a predetermined threshold, an event can be detected.

(ii) Moving statistics can be calculated in different window lengths, which might seem an appealing solution accounting for short–long variations over time. This advantage, however, implies a drawback when defining a justifiable window size, which is similarly true for the threshold values. The reader is referred to [84] for the sensitivity of factors in the presence of non-stationarities, shocks, and harmonics.

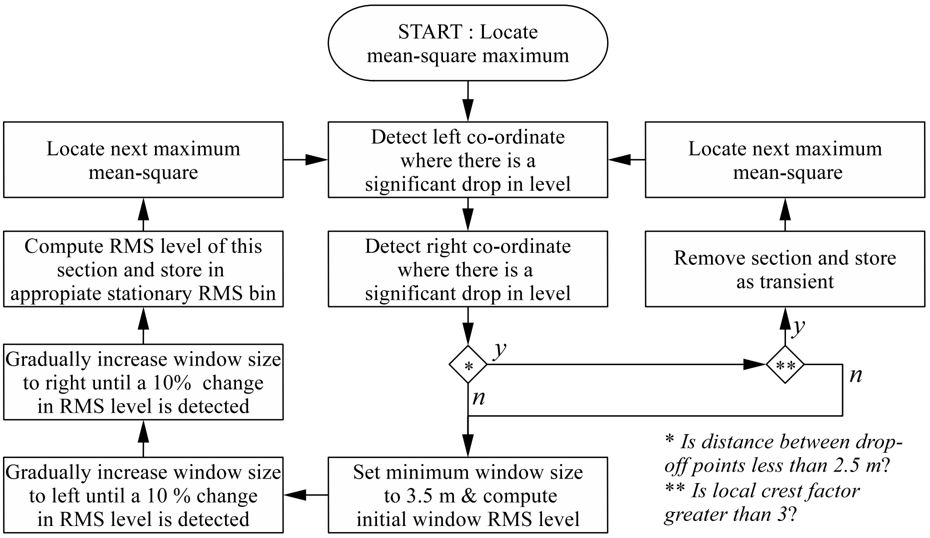

Figure 3.1: Flowchart for stationary and transient identification, reproduced from [86].

(iii) The moving statistics are heuristic approaches for signal segmentation. Still, it can assert the non-stationary nature of RVV. The simultaneous use of different window sizes of the same statistics can be implemented, as well.

3.1.2 RMS drop-off distance

(i) Constant RMS sections and transients in the spatial acceleration domain had been separated in [85] consisting of 415 km records, which utilize the mean square and kurtosis. The mean square gives an unbiased estimate of the power of a signal.

(ii) Due to scanning resolution, the process arrows had been lost. Thus, a subsequent article is used here to visualize the referred process diagram [86] in Fig. 3.1. Transients are detected by "*sufficiently short moving mean square drop-off distance*" and "*sufficiently large spatial acceleration local crest factor.*" The transient-free road segments are classified into bins of quasi-constant RMS levels [mm/m^2].

(iii) The presented method deploys arbitrary window size, bin widths, RMS levels, and Crest factors (CF) as carefully selected parameters. The authors admit that "*different values may affect the results*" but claim the remaining validity of the procedure.

3.1.3 Shock extraction method

(i) Shock extraction method is introduced in [87]. The original signal is decomposed into a series of approximated Gaussian segments and one shock segment, based on the Moving crest factor (MCF) and the One-tenth peak value (OTP) approaches.

(ii) The method is further studied in [88]. Albeit a "*pseudo code*" is provided, the authors remain silent about the algorithm. But it is apparent that events with $x_\kappa[k]$

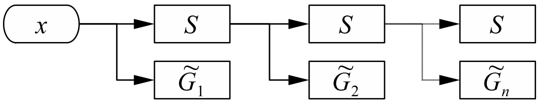

Figure 3.2: The decomposition workflow of Shock extraction method, S referring to shock, $\widetilde{G}_n$ denoting the n-th approximately Gaussian vibration. An individual representation inspired by [87].

greater than a threshold are extracted. A "*code*" calculates the optimal threshold value, such that κ of the remainder part is close to three. Another parameter (Hsize max. 0.5 s) is introduced to extract shocks, and ± 0.25 s around the peak location is found to be the duration of a shock. The lower limit on the duration of segments 5 s reflects on vibration table sensitivity. For simulation purposes, segments are simulated as stationary Gaussian signals, concatenated to match the total simulation time. Uniquely, segments are ordered ascending according to their RMS, and one shock segment is appended at the end.

(iii) It is reckoned that the One-tenth peak value (OTP) is equivalent to drop-off distance; however, a confusing definition is provided: "*a horizontal line drawing from one-tenth of the wave height intersects with the shock spectra, the time distance of those two intersection points is deemed to be the duration, t, of that shock spectra*" [87]. It is unclear how the time domain is interpreted on a spectra; or what wave height points out the estimation's initial point. *Wave* is also under-defined: if the vibration acceleration is meant, OTP is hard to define since shocks tend to fluctuate around an equilibrium. Albeit Moving crest factor (MCF) is often used to index transients, it is not always reliable and is often inappropriate for signals containing strong non-stationarities [50]. Fatigue life prediction may also be unrealistic since suffered damages may vary by the sequence of high- and low-, or low- and high-stress fluctuations [89, p.365]. An individual representation of the decomposition is depicted in Fig. 3.2.

3.1.4 Bayesian detector

(i) Thomas introduced a Bayesian detector to find homogeneous sections separated by changepoints within International roughness index (IRI) and rutting measurement series from different countries [90], according to the process visualized in Fig. 3.3. The resulted segments of the measurement series are considered homogeneous "*with respect to a certain criterion if the associated measurement series can be described by a single first-order auto-regressive process*" (ibid.).

(ii) The Box-Cox transformation brings the series closer to the model assumption of normal distribution. The heuristic At-most-one-change (AMOC) algorithm expresses the probability of inserting a changepoint $p(\text{change})$; secondly, selecting the location with the highest posterior support $p(\text{location}|\text{change})$. Heuristics are motivated by

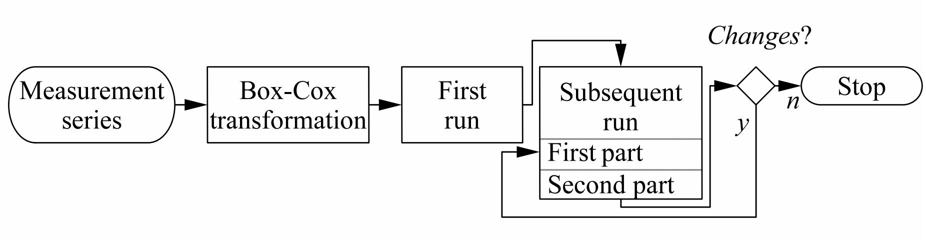

Figure 3.3: Steps in the execution of the algorithm, reproduced from [90].

placing changepoints sequentially instead of simultaneously to avoid a numerical burden by the binomial coefficient. The *first run* scans the series block-wise, obtaining the probability of the overall existence of a change somewhere. Given a changepoint, the block steps further; otherwise, the block slides to the right with an overlap. Blocks containing one changepoint are further analyzed in *subsequent runs*. The first part seeks for additional changepoints between preliminary borders. The second part checks the changepoint's actual necessity given the neighboring ones and its correct position. If neither the number nor the location of the changepoints is altered, the algorithm is terminated.

(iii) The method is a fast iterative algorithm that needs to undergo further experimentation [38]. Sometimes the method can get into an endless cycle of recurrent partitions. The approach objectively allows probability-based decision-making, even though various coefficients need to be determined.

3.1.5 Random Gaussian sequence decomposition

Charles formulates the idea of Random Gaussian Sequence Decomposition (RGSD), as non-Gaussian RVV can be decomposed into random Gaussian distributions [91]—Lepine reports in [38]. The idea is worked out later by Rouillard [92]. Sek in [93] summarizes other procedures of environment descriptions recommended by Charles. Rouillard uses Hilbert transform to obtain the magnitude of a vibration signal [94]. The reduced form of the magnitude is called vibration intensity, which can describe the statistical characteristics of an RVV. Id. introduces a different form of data reduction technique in [95] by a so-called dynamic bin width. Following, id. works out the RGSD [92] and later presents a cumulative-sum/bootstrap algorithm to find stationary segments in an RVV [96]. The synthesis of non-Gaussian RVVs is presented by id. in his thesis [97], which is currently under permanent embargo; still, the research [98] is published in the same year, presenting RGSD with the changepoint detecting algorithm and introduces the concept of modulation function. Id. introduces different distributions to characterize the non-stationary nature of RVV in [99].

Reduction of the analytic signal

(i) Rouillard and Sek hypothesize that a non-stationary random vibration signal can be modeled as the amplitude-modulated version of a steady-state random signal [94]. Given a time-series a, the analytic signal $\widetilde{a}$ is obtained by Hilbert-transform. The magnitude M of $\widetilde{a}$ is reduced and named vibration intensity, VI, which can be later used for amplitude modulation of a stationary Gaussian series.

(ii) Two methods are given for data reduction: a) M_{i+1} is eliminated, if $|M_i - M_{i+k}| < \Delta M$, where the selected magnitude bin is denoted by ΔM. Thus, consecutive M_i can be thought redundant, where those are between a tolerance limit; b) the VI can be further compressed according to the Probability density function PDF of VI, thus $\mathrm{PDF}_{\mathrm{VI}}$.

(iii) Ibid. is concerned in first place with reduction of M; however, a–b) are also reprehensible as segmentation methods, albeit ΔM and $\mathrm{PDF}_{\mathrm{VI}}$ bin width are subjective parameters.

Dynamic reduction of the analytic signal

(i) Segmentation with peak-valley considerations is presented in [95] to characterize the non-stationarity of RVV. Given a signal and its Hilbert-transform, the magnitude of the analytic signal is obtained. The magnitude is smoothed and fed to an algorithm to detect quasi-stationary sections. The algorithm reduces the number of points in M but utilizes a dynamic segmentation bin width and considers the peaks and valleys, M_{pv} .

(ii) The absolute difference |dM| between current VI_n and the subsequent $i+1$-th magnitude peak/valley $M_{\mathrm{pv}_{i+1}}$ is computed. The "*dynamic segmentation bin width*", VI^b is, simply put, a bin size to differentiate regions on the magnitude axis. If $|dM|$ is greater than the actual bin size corresponding to VI_n, a new segment is initiated at the investigated $M_{\mathrm{pv}_{i+1}}$ being the new initiative VI. If the difference is smaller than the actual threshold, the $M_{\mathrm{pv}_{i+1}}$ is included in the VI average and $M_{\mathrm{pv}_{i+1}}$ is discarded. An operation "$*I$" is not discussed.

(iii) The smoothing algorithm needs a window width, but the parameter is not introduced. Neither the identification of $M_{\mathrm{pv}_{i+1}}$ is discussed, nor the derivation of VI^b is available, whereas $b = 0.5$ exponent is found to "*produce very satisfactory results*".

Random Gaussian sequence decomposition

RGSD is a theoretical framework proposed by Charles and implemented by Rouillard [92]. The fundamental hypothesis covers that RVV is composed of zero-mean Gaussian processes with varying standard deviation. It is tested by comparing the sum of Gaussian estimates against the PDF of the original RVV. The algorithm does not provide changepoints within a measurement series; thus, it cannot indicate stationary segments' place and duration.

CUSUM–Bootstrap algorithm

(i) Rouillard presents a changepoint detection algorithm to find the length of stationary segments in RVV [96]. Instantaneous magnitude computed by Hilbert transform is subjected to a cumulative sum-bootstrapping method. The algorithm assesses the probability of a changepoint being present, thus deals with amplitude-type non-stationarities. A variety of RVV measurements and simulated time domain signals were used to derive a distribution of segment lengths.

(ii) In lack of a process diagram, the script is quoted here in the next six points (ibid.):

1. "*The instantaneous magnitude of vibration is computed using the Hilbert Transform.*
2. *Compute the cumulative sum of the instantaneous magnitude vector normalized with respect to the mean magnitude.*
3. *Apply the bootstrap algorithm sequence whereby the entire instantaneous vibration vector is randomly re-samples a number of times and the cum-sum re-computed for each re-sampled vector.*
4. *The maximum and minimum envelopes from the bootstrap samples are computed.*
5. *The largest extremum of the original record is detected and identified as a changepoint. Its value is compared with that of the bootstrap sample* (...).
6. *The change point is identified as significant or valid if the ratio of the largest extremum to the bootstrap extremum exceeds a predetermined value. In all cases studied, the ratio threshold of 5.5 was identified as adequate* (...)."

The record is bisected at a valid changepoint, and resulting segments are subjected to the same CUSUM-bootstrap procedure until no more changepoints are identified, or a minimum segment length is reached. It is worth noting that CUSUM here refers to the cumulative sum of differences between each value and the total mean of the series[1]

$$c_k = \sum_{i=1}^{k} (x_i - \bar{x_i}) \tag{3.1}$$

for $i = 1, ..., k$. The validity of candidate changepoints must be quantified, for which bootstrapping is applied. Certain factors are unknown, such as the number of replications for the reference set or whether a resampling[2] with- or without replacement

---

[1] An upward- or downward trend in c_k indicates values tending above or below the overall average.

[2] Bootstrapping and permutation are resampling with- and without replacement, respectively [79].

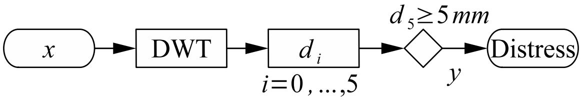

Figure 3.4: Wavelet decomposition. An individual representation inspired by [100].

is implemented. Usually, resampling is applied to derive the significance level of a changepoint being present in x, such as

$$\tilde{p} = \frac{1}{R} \# \{\underline{\hat{c}}_K < \underline{\hat{c}}_r\} \tag{3.2}$$

where $\tilde{p}$ is the estimated p-value, R is the number replications, $\# [\cdot]$ denotes number of elements, such that $\underline{\hat{c}}_K$ extremum is greater than the extrema from $\underline{\hat{c}}_r$ in replications $r = 1, ..., R$. Id. uses a different approach:

$$\underline{\hat{c}}_K > 5.5 \cdot \underline{\hat{c}}_r, \tag{3.3}$$

seemingly heuristically, since the 5.5 multiplier is found "*adequate*". Against too many changepoints, individual thresholding was necessary instead of significance levels.

(iii) Albeit the algorithm skips the possibility of significance levels, and some factors are hidden, several RVV signals subjected to this algorithm had produced consistent estimates on the probability density function of segment lengths by considering amplitude-type non-stationarities.

3.2 Segmentation in frequency domain

Following methods consider spectral characteristics, for which Fourier-, wavelet-, and Hilbert-Huang transform is often favored. Their introduction is set aside here, whereby the reader is referred to consult the actual references.

3.2.1 Wavelet decomposition

(i) Wei et al. introduce a wavelet decomposition procedure, supplying supplementary information to pavement roughness indices [100]. Id. investigates the capability of wavelets in the detection of local pavement distresses and provides the following algorithm.

(ii) International roughness index (IRI) signal given in the distance domain is decomposed by DWT into frequency sub-bands d_i. A supra-threshold amplitude in the sub-band d_5 indicates possible surface distresses for field inspection. An individual representation can be found in Fig. 3.4.

(iii) The decomposition given Daubechies wavelet (DB3) is found proper until the fifth sub-band. The specific number of sub-bands shows that the necessary number of decomposition levels must be investigated per application, just like the threshold's justification. Unfortunately, the detection capability has been presented only on International roughness index (IRI) series having artificial distresses. Despite the manual transients in the signals, the article served as initial points in later research to investigate the wavelets in high-sampled time-series, such as vertical acceleration vibrations.

3.2.2 Separation by filtering

(i) Rouillard et al. present separation by filtering in [101] for rail car vibration environment. Shocks are removed in frames from the time domain signal via thresholding. Filtering in the frequency domain is introduced as an alternative approach, for which different assumptions are necessary. The simulation superimposes intermittently occurring structural vibrations (transients or shocks) onto the rigid-body random vibrations.

(ii) A numerical low-pass filter separates the rigid-body- and structural vibrations at the cut frequency. Id. believes that impulsive vibrations can be described by their "*amplitude and their statistical likelihood of occurrence*" given their similar characteristic. It is assumed that a) rigid-body motions are band-limited up to a cut-off frequency and intermittent vibrations lie within a different frequency band; b) rigid-body motions have the same frequency characteristics, i.e., quasi-stationarity throughout the record. Finally, the similar characteristics of impulsive vibrations must be investigated—unfortunately, no guidance is provided.

(iii) From a simulation perspective, this is the Shock-on-random method. Shocks are simulated according to their amplitude PDF and triggered by a random clock. Random vibration is modeled as a steady-state Gaussian signal from the average rigid-body PSD. Here, I presume that assumptions *a-b)* are closely related to the investigated scenario of rail-car vibrations, whereby those cannot be guaranteed in RVV.

3.2.3 Intrinsic mode functions

(i) Rouillard introduces the Hilbert-Huang transform (HHT) for the analysis of rail-car vibrations aimed to describe prevalent frequency-type non-stationarities [102].

(ii) By HHT, the random signal is sifted into intrinsic mode functions (IMF), and the analytic signal from each IMF is computed. The absolute value of the analytic signal corresponds to instantaneous magnitude. Id. assumes that modes 1–4 represent higher, modes 5–7 represent lower frequency components, and modes 8–12 are ignored, describing very low frequencies. It is concluded that the method has a special significance in the simulation of rail-car vibrations since it may be well advantageous to simulate these two processes separately. The superior resolution of IMF is highlighted, and a spectrogram is presented, but methods for changepoint detection are not offered.

(iii) The paper successfully corresponds to the introduction of HHT in PVT; however, no process is offered to identify changes in the spectrogram.

3.3 Segmentation in time-frequency domain

Following methods operate in the time-frequency domain. Typical choices are continuous wavelet- and Hilbert–Huang transform, whereby short-time Fourier transform is rarely used in the presented methods.

3.3.1 Wavelet-based Gaussian decomposition

(i) Griffiths et al. developed the Wavelet-based Gaussian decomposition (WBGD) to decompose RVV into series of segments with different kurtosis, which can be separately simulated and concatenated to obtain a non-stationary random vibration in total [103, 104]. The approach uses the continuous wavelet transform (CWT), evaluating the frequency spectra' variation through time.

(ii) The process can be articulated along the following ideas in Fig. 3.5. Slightly different notations are used here to help the understanding. Given a vibration signal y_m and its power spectral density $S_{y,m}$, an equivalent stationary Gaussian vibration x_m can be derived. The CWT of each signal is obtained by a complex wavelet, resulting in positive and negative absolute coefficients $C_{y,m}(a, b)$ and $C_{x,m}(a, b)$. A decomposition envelope DE is derived from the extrema through the translation b of $C_{x,m}(a, b)$. Regions of $C_{y,m}(a, b)$ outside DE are candidates of non-Gaussian regions; in turn, *in-lying* regions are considered Gaussian parts. "*The data windows surrounding locations that exceed the envelope are extracted from the vibration signal,*" here at shortest 1 s. Out- and *in-lier* regions $C^O_{y,m}(a, b)$ and $C^I_{y,m}(a, b)$ are concatenated, forming two signals, and their wavelet coefficients are inversely transformed, yielding y^O_m, and y^I_m, respectively. If the kurtosis $\beta_2(y^O_m)$ is smaller than a threshold β_{2T}, the vibration signal $y_{m=1}$ is replaced by the outlier y^O_m, and the decomposition is repeated from 1–7), yielding $y = y^I_1||...||y^I_M||y^O_M$. The iteration continues until the iteration limiting number M is reached or $\beta_2(y^I_m) < \beta_{2T}$. The second stage of iteration might begin to form

$$y^I_{i_1}(t) = \sum_{i_2=1}^{S} y^{I,I}_{i_1,i_2}(t) + y^{I,O}_{i_1,S}(t), \text{for } i_1 = 1, ..., M \tag{3.4}$$

$$y^O_M(t) = \sum_{i_2=1}^{S} y^{O,I}_{M_1,i_2}(t) + y^{O,O}_{M,S}(t) \tag{3.5}$$

Steps 1–8) are repeated given a supra-threshold kurtosis or until the iteration limiting number S per component i_1. Through simulation, final components can be simulated by individual $S_{m,s}$ corresponding to the duration $T_{m,s}$ ordered in a desired sequence. y_M^O is likely to contain most of the high-level shock events, which can be further decomposed in the second stage arriving at $y_{M,S}^{O;O}$, which still encompass most of the non-Gaussian characteristics, constituted by mainly the high-amplitude events. "*These segments will have highly non-Gaussian distributions, thereby strengthening the limitation that the wavelet decomposition method will always produce one Gaussian approximation that is highly non-Gaussian*" [103, p.190].

(iii) WBGD operates in the scale-translation domain, and in an iterative manner, partitions the CWT of an RVV into quasi-Gaussian- and remaining parts concerning the kurtosis. The main idea to highlight here is that a section is labeled as Gaussian if its CWT fits within the CWT extrema of a Gaussian equivalent at any iteration stage. The simulated signal has a good match in PSD and kurtosis to the measured RVV, albeit the RMS distributions of the original and simulated signals are significantly different, although it is expected by id. [104, pp.788–789]; however, it remains inconsistent with other empirical studies concerned with the RMS distribution of Gaussian segments.

3.3.2 Hilbert amplitude spectrum

(i) Mao et al. presented their method based on the Hilbert amplitude spectrum to characterize and simulate non-stationary random vibrations [105], as in Fig. 3.6. Note that the current section chooses slightly different notations for readability.

(ii) Given an $s(t)$ sample, the Hilbert-Huang transform yields the $H_S(\omega, t)$ time-frequency domain. The CUSUM approach is responsible for changepoint detection per each frequency bin over time. The instantaneous magnitudes between changepoints are fitted by five different distributions P_Θ as gamma, exponential, Rayleigh, log-normal, and Weibull distributions for $\Theta : G, E, R, Ln, W$. The Kullback–Leibler divergences for P_Θ of instantaneous magnitude within segments $h(\omega_i, t)$ are calculated:

$$\delta\mathrm{KL}_\Theta(P_\Theta || h(\omega_i, t)) = \int P_\Theta \log_{10} \frac{P_\Theta}{h(\omega_i, t)} dt \geq 0, \tag{3.6}$$

and averaged through segments of each frequency yielding $\overline{\delta\mathrm{KL}}_\Theta(\omega_i)$. The idea to highlight here is that each frequency section is characterized by one family of fits having the lowest $\overline{\delta\mathrm{KL}}_\Theta(\omega_i)$. By simulation, random variables are generated according to P_Θ, and in conjunction with a phase function $\Psi(t)$, finally $x(t)$ can be simulated.

(iii) Further improvements might be obtained by choosing the best-from-the-five fits directly in each segment. This can be justifiable if $\overline{\delta\mathrm{KL}}_\Theta(\omega_i)$ are biased by the outlier $\delta\mathrm{KL}_\Theta$. Besides, the method is capable of segmentation in the time-frequency domain, however, as the virtue of the fitted distributions, it can also be considered a random

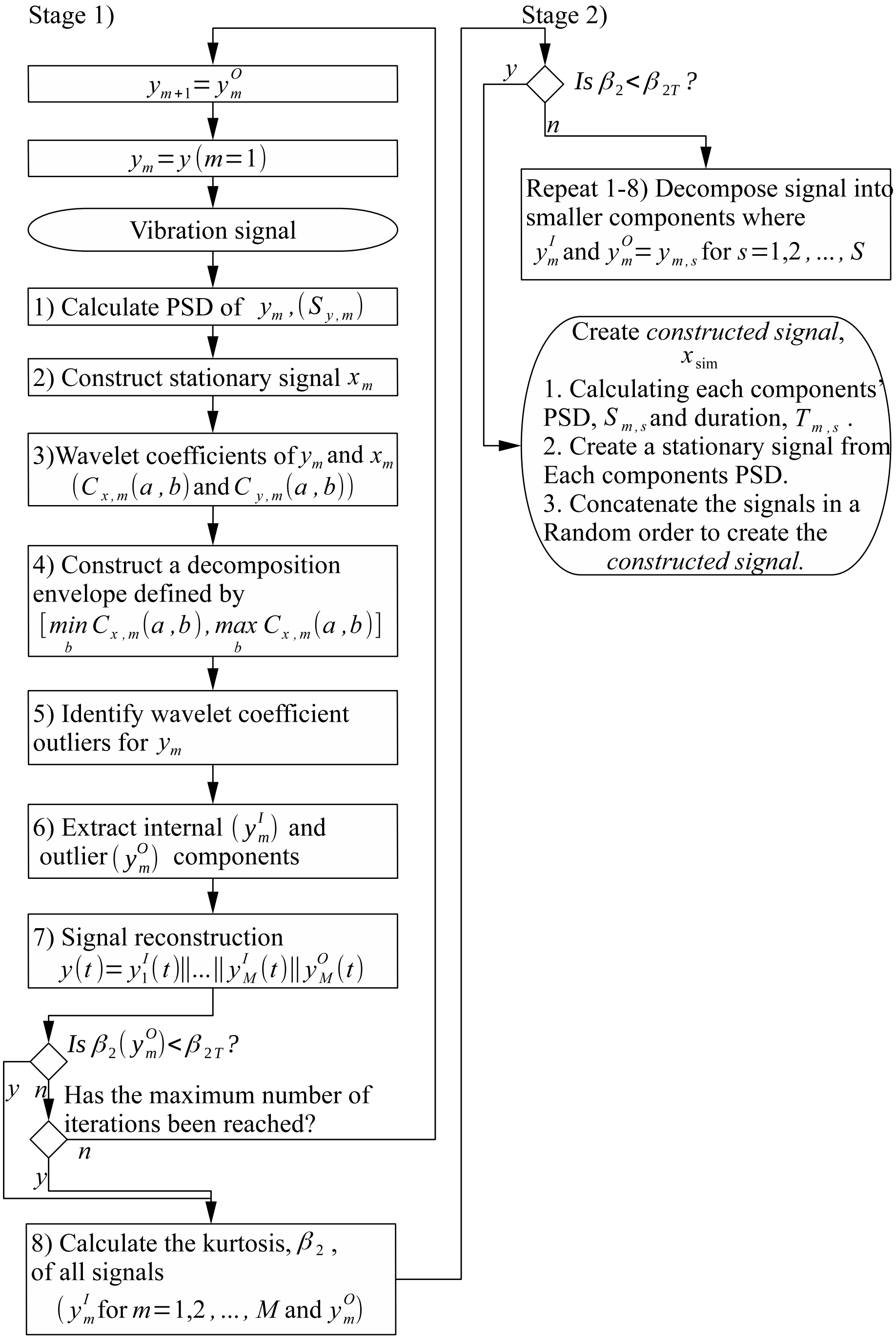

Figure 3.5: Wavelet-based Gaussian decomposition, reproduced from [104].

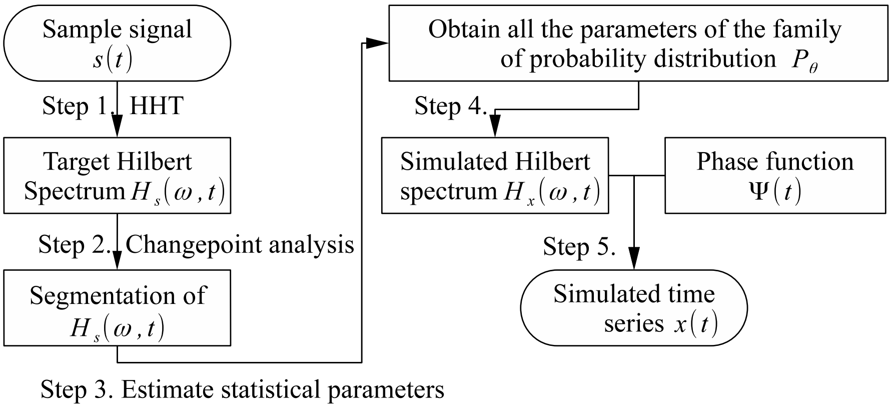

Figure 3.6: Flow diagram of simulation method, reproduced from [105].

simulative approach.

3.4 Mixed methods

Here an algorithm is referred to as a mixed-method if it can consider time- and frequency domain characteristics simultaneously.

(i) Lepine presented a continuous contribution to PVT by studying Machine learning classifiers (MLC) to detect shocks in RVV. The foundation of MLC is presented in the thesis [84]. The support vector machine (SVM) had been compared to the moving crest factor via receiver operating characteristics (ROC) in [50]. Four different MLC (decision tree, k-nearest neighbors, bagged ensemble, SVM) are investigated by synthetic RVV in [106], as in Fig. 3.7. Ibid. is constituted by a detection enhancement algorithm in Fig. 3.8. The above MLC are further analyzed, and validation by real RVV is proposed in [49].

(ii) RVV measurements with registered shocks are mostly unpractical. Thus artificial RVV might be generated [106]. The synthesis mimics natural RVV as far as the dynamic model is accurate. Different predictors are used, such as $x_{\text{rms}}, x_{\text{cf}}, x_\kappa$, DWT, instantaneous amplitudes, and frequencies of the IMF from HHT. The validation and calibration of MLC hold several possibilities, such as ROC curves, the distribution of absolute peak acceleration of shocks can be compared among the validation signal and detections, the purpose-developed Pseudo energy ratio–fall-out (PERFO) curves. Optimal operating point (OOP) definition has various possibilities; however, OOP by synthetic calibration is inadequate for real RVV applications in [49]. In consequence, a synthetically setup MLC may not be directly suitable for real-world applications. Definition of shock also has special considerations as of application, e.g., "*sudden and severe accelerations of a finite and measurable duration*" [50]; or "*a sequence of data points instead of individual data points*" together with the "*detection has to overlap at least 75% of the shock duration to be considered true*" in the validation [49]. The

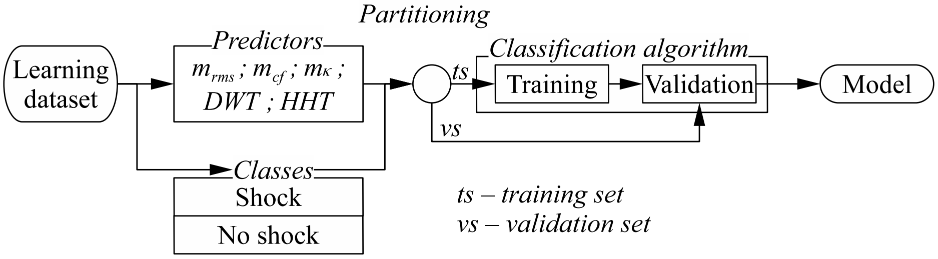

Figure 3.7: The workflow of the classification algorithm, reproduced from [106].

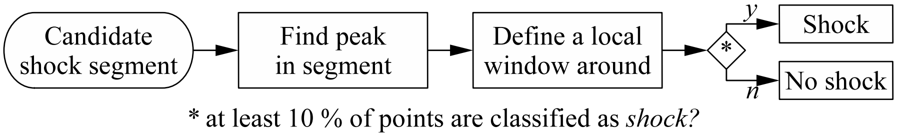

Figure 3.8: Detection enhancement algorithm, individual representation from [106].

enhancement algorithm covers a window size in [106]. All data in the window is classified as a shock if it contains “at least 10% of data points”.

(iii) A “*considerably more accurate and reliable*” detection performance of the MLC is claimed against the conventional moving crest factor (64 s), producing 13% better area under the ROC curve (AUC index) [50]—but one should consider the numerical expenses of this improvement. Development of performance assessment methods is presented, such as ROC- and PERFO curves, distribution of absolute maximum accelerations of shocks. Furthermore, the definition of shock might be necessary to adjust. Since inconsistencies are shown for synthetically setup MLC in real-world applications, validation on real-world RVV was proposed [49]. Consequently, the on-site measurements with a precise indication of shock-inducing instances are hardly avoidable. Additional validation of the MLC must be undertaken for the general implementation of MLC to specific RVV (ibid.).

3.5 Discussion

A concise appraisal platform is provided in Table 3.1, discussing various aspects of the dilemma of adaptability. Each method is investigated by *a)* reproducibility, *b)* heuristics, *c)* subjective thresholds and *d)* accompanying simulations, discussed in the followings. A method is considered reproducible *a)* if it can be translated into programming languages solely on the published information, given the same dataset is on-hand. For instance, a method being silent about sub-steps in the reference cannot be considered reproducible in the author’s eyes. Point *b)* corresponds to the need for manual parameters and settings in the approach. While some algorithms are designed for heuristic solutions (e.g., to avoid computational overflow) and others had to experiment with the method itself *anno*, one can have preferences now toward data-driven solutions, as well. However, the new adoption of such techniques and some form of heuristics does not mean obsoleteness. Question *c)* investigates unexplained threshold values, while a few of them have traditional uses noted in the table notes. Finally, question *d)* reflects mainly on the early adoption of the segmentation methods in the simulations. Papers devoted only to detection still possess an important place in the history of technology. In conclusion of the appraisal platform, it is advised to perceive the legend entries of Table 3.1 as state-switches or toggles instead of scores. The following paragraphs discuss and summarize the above methods.

Moving statistics have the longest history because of simple implementation, thus, an early introduction to the discipline, as well. The window size and the threshold value often need heuristics to arrive at a sufficient solution. RMS drop-off distance partially uses such techniques thoroughly investigated in the thesis. Shock extraction method is a young algorithm, mostly relying on older approaches. It is not easily implementable, until new insights in the algorithm are provided. Bayesian approaches represent a traceable procedure with transparent insight into decisions. Its performance must be presented on high-sampled datasets, as well. The Section 3.1.5, including subordinate methods have the strongest establishment in PVT. However, a few details are only provided on a seemingly investigatory basis.

Frequency characteristics are often in the interest, relying on Fourier-, wavelet- and Hilbert- transforms. Apart from theories applied to arrive in this domain, distinctive approaches can be mentioned here. The Wavelet decomposition [100] uses thresholds to find transients. Separation by filtering is a well-established method, leaving the cut-frequency the only investigatory parameter beside general necessities (e.g., windowing) in discrete Fourier transform. Albeit no changepoint detection had been presented above in regard to Intrinsic mode functions, it is still regularly used nowadays because of its superior resolution. Wavelet-based Gaussian decomposition [103] presents a unique approach, utilizing CWT. The concerns addressed in terms of simulated signals must be investigated on an individual basis before implementation. Hilbert amplitude spectrum by [105] is successful both in segmentation and simulation.

MLC applications show promising results but only in a costly manner. The presented PVT applications show good accuracy on shock detection; presumably, further developments are ahead. In summary, moving statistics are recommended only in an explanatory phase of the analysis. For detection in time domain, the CUSUM–Bootstrap- along with the Bayesian approaches are favorable. The sample of frequency domain approaches is smaller; thus, a try can be given for any of the three procedures. Both time-frequency domain methods produce transparent results, therefore those encompass preferably successful implementations. Hence, a favorable algorithm is numerically parsimonious, utilizes as few heuristics and subjective thresholds as possible, and prefers data-driven solutions. It provides a transparent decision-making and remains reproducible.

Table 3.1: Appraisal matrix of previous segmentation methods proposed before non-stationary simulations or introduced as standalone methods, investigated by *a)* Reproducible? *b)* Avoid of heuristics? *c)* Avoid of subjective thresholds? *d)* Accompanied by simulation?

Domain	**Segmentation method**	**R.**	***a)***	***b)***	***c)***	***d)***
Time	Moving statistics[1]	[83]	●	○	○	○
	RMS drop-off distance	[85]	●	∗[2]	●	●
	Shock extraction method	[87]	○[3]	∗[4]	○	●
	Bayesian detector	[90]	●	○	●	○
	Reduction of analytic signal	[94]	●	∗[5]	●	●
	Dynamic reduction of analytic signal	[95]	●	●	∗[6]	●
	CUSUM-Bootstrap algorithm	[96]	●	∗[7]	∗[8]	●
Frequency	Wavelet decomposition	[100]	●	∗[9]	○	○
	Separation by filtering	[101]	●	●	○	●
	Intrinsic mode functions	[102]	●	∗[10]	∗[11]	○
Time-Frequency	Wavelet-based Gaussian Decomposition	[103]	●	∗[12]	●	●
	Hilbert amplitude spectrum	[105]	●	●	∗[13]	●
Mixed	Machine learning classifiers	[84]	∗[14]	●	∗[15]	●

Legend: **R.** - first reference; ● - yes; ∗ - conditionally yes; ○ - no

[1] Noting, that it is a cross-disciplinary technique.

[2] Apart from the moving window size.

[3] Since "*pseudo code flow*" remains unexplained, e.g., Hsize.

[4] Apart from unexplained steps, the algorithm seems to work autonomously.

[5] Accepting the selected magnitude bin ΔM , as a data driven solution.

[6] The threshold value is derived from a subjective parameter, VI^b

[7] Apart from Eq. 3.3 above.

[8] Apart from Eq. 3.3 above.

[9] Accepting, that type of wavelets and the level of decomposition are inherent to DWT.

[10] Since the number of IMFs separating low- and high frequencies are only "*assumed*".

[11] If the "*assumed*" number of IMFs—separating low- and high frequencies—are accepted.

[12] Accepting, that type of wavelets and the level of decomposition are inherent to CWT.

[13] Accepting, that significance limits in hypothesis testing have traditional uses.

[14] Accepting, that the "*skills*" of machine learning classifiers depend on the training.

[15] Since some predictors are moving statistics.

3.6 Conclusion

It is agreed that packaging systems set up a safety factor in the assurance of the transported goods' quality. However, different costs can be associated to over- and under-insurance of the shipment. Therefore, the academic community developed various vibration simulation methods beneath standardized procedures, each containing unique signal segmentation practices.

Standardized methods in PVT remain in position for the expected conformity toward standards. Concurrent new methods emerge to account for the deficiencies of PSD-based methods, viz., the produced random vibrations are stationary and Gaussian. No universally accepted method for RVV simulations exist as pointed out by [38], who also addressed some segmentation techniques. In line with this, the applied changepoint detection algorithms present a wide toolbar. Harmonic excitation in RVV is still hardly discussed; the above approaches can partially address the phenomena. Thus, the discussed methods mainly apply to transient event- and non-stationary segment border detection. Unfortunately, some algorithms are hardly reproducible, which does not facilitate the acceptability of proposed methods and delays improvements in standards.

The amplitude- and frequency-type non-stationarities in RVV can be simultaneously approached from the time-frequency domain. Frequency modulation detection is less discussed than amplitude disturbances, as apparent from the number of methods. Numerically parsimonious methods are mostly heuristics, based on window statistics and thresholds, which may produce satisfactory results, given the corresponding parameters are justifiable. Sophisticated signal processing methods still often encounter some form of subjective thresholds. Therefore, data driven approaches are favorable.

Thesis 2. I have observed that previous segmentation algorithms have been uncalibrated and designed along heuristic considerations in several cases. Calibration of detection algorithms is essential when investigating road-induced vibrations. For verification purposes, the segment length distribution should be investigated on a test sample, as a necessary complementary investigation beneath the receiver operating characteristic. ■
Ref.: [5]

Chapter 4

Development of segmentations

This chapter introduces three different segmentation methods. First, the short-time Fourier transform plane is segmented by paired t-tests in Section 4.1 as of [7]. A subsequent variant investigates the two-sample t-test in the multiple comparison procedure in Section 4.2 according to [6]. Finally, the spectral moment segmentation, foreshadowed in Chapter 2, is discussed in more details by Section 4.3 [4, 10].

4.1 Multiple hypothesis testing by paired samples

Segmentation of road vehicle vibration (RVV) signals can occur by the need to analyze or synthesize vibrations obtained in passenger cars or on the stowage of vans, trucks. A general and widely used measure to quantify RVV signals is its description via power spectral density (PSD). From a given PSD a Gaussian signal can be generated in a shaker testing laboratory. However, actual RVVs tend to have a non-Gaussian and non-stationary nature, which can be modeled as a composition of different segments, each with a different length and RMS content. For simulation purposes of non-stationary vibration signals, various approaches had been introduced yet each with its unique signal segmentation. Here, a signal segmentation method is proposed working in the time-frequency domain for finding segments within an RVV signal, where each segment has similarity in-between and are dissimilar to neighboring segments according to the paired t-test [107, p.1560]. For this purpose, multiple hypothesis tests (MHT) had been utilized between the Short-time Fourier transforms (STFT) applied on given fractions of an RVV. Different countermeasures had been applied against the Type I. error inflation [107, p.1574].[1]

---

[1] Further details on erroneous statistical decisions can be found in Table 4.1 and 4.2, the interested reader also finds valuable summaries in [107, pp.1574–1581].

4.1.1 Introduction

A hypothesis testing-based RVV segmentation method is introduced in the followings, in order to systematically assess the information contained in the time-frequency domain of a given measurement series. The current procedure consists of the interpretation of paired sample t-test [107, p.1560] and the Wilcoxon signed rank test [108, p.25-17] in order to find spectrally similar segments within the waterfall plot of the Discrete Fourier transforms (DFT) calculated per 2 s of an RVV. After the multiple hypothesis procedures, two different methods will be introduced against Type I. error inflation, which is accountable in multiple hypothesis testing. Different agglomerate diagnostics of the yielded segments will be briefly compared with an emphasis on the *post hoc* tests [109].

4.1.2 Methods

The independence of samples must be ensured before evaluating hypothesis tests in the current method. Therefore, the auto-correlation function of the acceleration signal had been examined first in Fig. 4.1. The acceleration signal is strongly auto-correlated within 2 s, which has the practical consequence that the smallest time resolution of the current segmentation algorithm is limited to 2 s, and shorter segments within STFT cannot be detected. Smaller fluctuations of the ACF exceeding the confidence interval are also noticeable in higher lags, which are assumed here non-significant, as if the signal was not auto-correlated above lags corresponding to 2 s.

The given signal in Fig. 4.2 represents the waterfall plot of the DFTs of an RVV signal measured on a passenger car's cockpit sampled with 1 kHz during a 600 s long journey in the study of [110]. A window frame equal to 2000 samples used for the calculation of DFTs yielded 300 timeframes.

The time-frequency domain is interpreted on an equidistant grid per axis with 0.5 Hz and 2 s resolution. The following calculations are limited to the [0,100] Hz bandwidth. The DFT vectors have the same resolution over time; thus, it can be interpreted as the paired observations of the same frequency bins over time.

The paired sample t-test and its non-parametric variant, the Wilcoxon signed rank test are utilized here to find the dissimilarities between consecutive DFT distributions. Two vectors of the spectrum lines will be compared on the $\alpha_0 = 0.10$ preliminary significance level. Afterwards, the resulted series of p-values are compared to differently adjusted significance levels.

Paired sample t-test

Using a one-sample t-test, statistical inference can be made about the null hypothesis that the data comes from a population with a mean equal to μ. The alternative

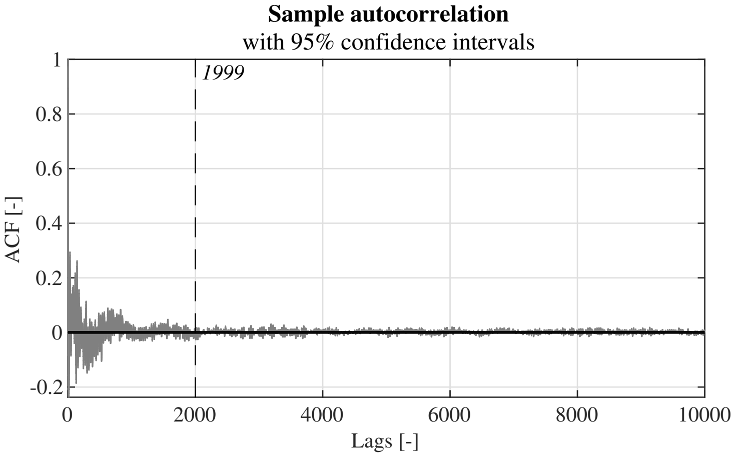

Figure 4.1: Auto-correlation function of the acceleration signal (*black*), with 95% confidence interval (*grey*), where dashed vertical at lag 1999 denotes the subjective border, above which ACF is considered minor.

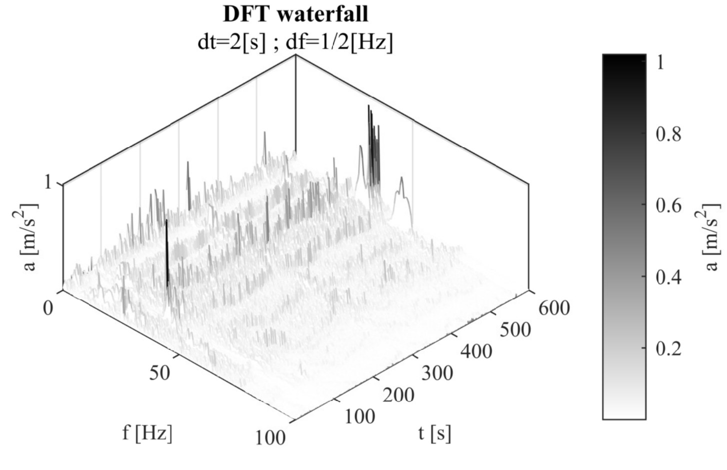

Figure 4.2: Waterfall plot of the discrete Fourier transforms per 2 s, where the resolution is 0.5 Hz in the frequency domain and 2 s in the time domain.

hypothesis can be formulated as that the population distribution does not have a mean equal to μ. The one-sample t-test is a parametric test of the location parameter when the population standard deviation is unknown. Under the null hypothesis, the test statistic has a Student's t-distribution with $n-1$ degrees of freedom [111]. The corresponding hypothesis pair for a two-sided test is, as follows

$$\begin{cases} H_0 : \text{data has a mean equal to } \mu, \\ H_A : \text{data does not have a mean equal to } \mu. \end{cases} \tag{4.1}$$

The observations in each group are paired with another observation from the other group. The distribution of differences did not follow a normal distribution from the total 299 sets based on Anderson–Darling tests on 0.10 significance level. The assumption of normality of the differences is harmed in every case. However, paired t-test are *robust* to the assumption of normality [108]. The chapter proceeds with the paired t-test despite the possible effects of the outliers, since the reason for outliers being present remains unknown; on the other hand, changes in spectral peaks (on the reason of either frequency- or amplitude modulation) are in the major interest of the current examination. Alongside the non-parametric Wilcoxon signed rank test [112] is also implemented in another MHT, which are more suitable to the testing of non-normal data. The differences between each of the paired observations serve as the input to conduct a one-sample t-test, and the non-parametric Wilcoxon signed rank test. The paired sample t-test assess the null hypothesis, that the data in $d = x - y$, comes from a normal distribution with mean equal to 0. The paired sample t-test is practically a one-sample t-test of the mean of differences between the paired observations, to test the null hypothesis that the pairwise differences d between data vectors x and y has a mean equal to 0, such as

$$\begin{cases} H_0 : \text{data in } d = x - y \text{ has a mean equal to } \mu, \\ H_A : \text{data in } d = x - y \text{ does not have a mean equal to } \mu. \end{cases} \tag{4.2}$$

The p-value is the probability of the test statistic being at least as extreme as the one observed, given that the null hypothesis is true. The choice of α is somewhat arbitrary, although in practice values of $0.10, 0.05, 0.01$ are commonly used. The significance level will not be considered here as a part of either the acceptance or the rejection areas. It is also examined that no p-value falls on the significance limits in Fig. 4.9.

After completing STFT with 2 s window lengths resulted in Fig. 4.2, the current design can be considered as the paired observations of DFT values a_i in the $2i$-th seconds, in-between 0.5 Hz resolution. Let j denote the j-th difference vector and the

j-th hypothesis pair takes the form

$$\begin{cases} H_0^{(j)} : d_j = a_i - a_{i+1} \text{ has a mean equal to } 0, \\ H_A^{(j)} : d_j = a_i - a_{i+1} \text{ does not have a mean equal to } 0. \end{cases} \tag{4.3}$$

When we fail to reject the $H_0^{(j)}$, that would indicate that two consecutive DFT vectors have the same mean, which could indicate that these vectors are associated through their mean statistics, and those will be grouped in the same segment. In case of a significant finding, namely we reject an $H_0^{(j)}$ in favor of $H_A^{(j)}$ would indicate that the two consecutive DFT vectors do not have the same mean, which could indicate dissimilarity among the mean statistics of the vectors, hence they are not associated in this sense, and the initial point of a new segment can be defined.

Wilcoxon signed rank test

The non-parametric Wilcoxon signed rank test is utilized here for two populations being paired. The test statistic, W is the sum of the ranks of positive differences between the observations in the two samples, d_j. The returned $p_W^{(j)}$-value corresponds to a paired, two-sided test for the null hypothesis that d_j comes from a distribution with a median equal 0. In case the sample size is large, or the method is approximate, the test function calculates the p-value using the z-statistic [111].

α adjustment

The preliminary significance limit is set to $\alpha = 0.10$ in current example. Even though a high number of tests found significant *a priori*, not all of them may be considered truly significant due to α inflation. This section introduces the Type I. error inflation and the following two sections deal with two different *post hoc* procedures to control the Family-wise error rate (FWER).

The Type I. error rate or significance level is the probability of rejecting the null hypothesis, given that it is true [107]. If the null hypothesis is false, then it is impossible to make a Type I. error [113]. The incorrect rejection of the null hypothesis is referred to as a false positive. The probability of correctly accepting a true null hypothesis equals $S = 1 - \alpha$ and is called specificity.

The incorrect acceptance of the null hypothesis is called Type II. error [107], which can only occur if the null hypothesis is false, and the probability of committing this error is called β. This second type of error is often called a false negative. The probability of correctly rejecting a false null hypothesis is $P = 1 - \beta$ and is called power. Type of the possible statistical inferences are given in Table 4.1.

In the simultaneous multiple comparisons of more than two groups, e.g., e,B,C the following $j = 1, \ldots m$ hypotheses can be formulated, and the set of comparisons is

Table 4.1: Types of conclusions in a statistical hypothesis test.

		Statistical inference	
		H_0 true*	H_0 false
Actual fact	H_0 true	Correct decision, $S = 1 - \alpha$	Type. I error, α
	H_0 false	Type II. error β	Correct Decision, $P = 1 - \beta$

* Precisely, fails to reject H_0
Specificity, S; power or sensitivity, P.

Table 4.2: Framework of multiple hypothesis tests.

		Statistical inference	
	Total, m	H_0 true Not rejectd, $m - R$	H_0 False Rejected, R
Actual fact	H_0 true m_0	Correct decision, $m_0 - U$	Type. I error, U
	H_0 false $m - m_0$	Type II. error $m - R - (m_0 - U)$	Correct Decision, $R - U$

* Precisely, fails to reject H_0.
$m, m_0, R, U, \ldots$ denote the number of hypotheses in the cell.

referred to as a family of test. In the current case, $m = 299$ comparisons per MHT had been made. Table 4.2 introduces the framework for simultaneous hypotheses testing [114], given at least two hypotheses to be tested.

When more than one hypothesis has simultaneously tested the probability of committing false statistical inferences increases considerably. Utilizing the same Type I. error rate in an increasing number of comparisons will result in an ascending family-wise error rate[2] FWER $= P(U > 0)$, i.e., it will increase the probability of at least one Type I. error during the MHT. The Bonferroni inequality can be expressed for a set of tests, as $\alpha_\mathrm{f} \leq m \cdot \alpha_\mathrm{p}$. The overall error level for the family of tests α_f differs from the α_p error level for one comparison. If the same α_p error level is adopted for each comparison in m multiple hypothesis, the overall α error level for the family of tests α_f is calculated as the following procedure in Eq. 4.4–4.5 [109]: The probability of no α error per one comparison is $S_{pc} = 1 - \alpha_\mathrm{p}$, and the probability of no α error for the overall family of m tests is

$$S_\mathrm{f} = (1 - \alpha_\mathrm{p}) \cdot \ldots \cdot (1 - \alpha_\mathrm{p}) = (1 - \alpha_\mathrm{p})^m \tag{4.4}$$

---

[2] Other measures for accounting Type I. errors [114], like the per-comparison error rate, such as PCER $= E(U)/m$, where $E(\cdot)$ denotes the expected value; or the false discovery rate, such as FDR $= \{E(U/R)$, if $R > 0$; otherwise FDR $= 0$,if $R = 0\}$ are not discussed here.

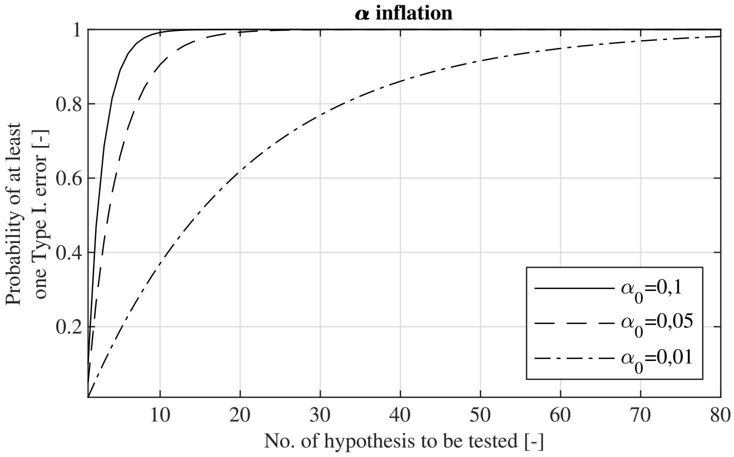

Figure 4.3: Alpha inflation. Probability of at least one Type I. error as a function of the number of comparisons for cases of applying the same 0.10, 0.05 and 0.01 significance levels per comparison.

for comparisons independent of each other. The family-wise Type I. error rate is

$$\alpha_{\mathrm{f}} = 1 - (1 - \alpha_{\mathrm{p}})^{m} \tag{4.5}$$

The Eq. 4.5 is also known, as α inflation and is visualized in Fig. 4.3 for three different preliminary chosen typical $\alpha_0 = \alpha_{\mathrm{p}}$ levels.

Different α adjustment techniques can be introduced as countermeasures to overcome the issue of the inflating likelihood of a Type I. error. The following subsections discuss two of the possible processes, namely the most straightforward—sometimes referred to as over-conservative—Bonferroni adjustment and its less conservative variant the Holm–Bonferroni adjustment.

Here shall be noted that for the goal of current signal segmentation method, the MHT is not utilized in the same manner as some of the typical *post hoc* tests following an ANOVA design, where the tests are interested in all pairwise comparison (e.g. A–B, A–C, B–C). The number of hypotheses to be tested is relatively high; on the other hand, the design of the current experiment is only interested in the comparison of neighboring vectors (e.g. A–B, B–C). Therefore, a consecutive setup conforms best the approach of this method.

Bonferroni adjustment

The Bonferroni method [115] is a simple technique that makes it possible to make several comparison statements while ensuring that an overall confidence coefficient is preserved. The significance level is divided by the number of hypotheses tests, and each

p-value is compared to the new significance level

$$\alpha_{\mathrm{B}} = \frac{\alpha_0}{m} \tag{4.6}$$

The more hypotheses to be tested, the criterion gets more stringent and lowers the Type I. error per comparison, but also lowers the test's power.

Holm–Bonferroni adjustment

Holm adjustment [116] was subsequently proposed with less conservative character [117] and more power [109]. The method computes the significance levels α_{HB} depending on the rank of p-value. A step-down procedure is performed according to the ascending ordered $p^{(s)}$ value compared to successively increasing significance limits. The procedure similarly to [114] is as follows. The adjusted significance limit for the s-th hypothesis is

$$\alpha_{\mathrm{HB}} = \frac{\alpha_0}{m - s + 1} \tag{4.7}$$

and $H^{(1)}, \ldots, H^{(m)}$ are tested from the smallest to the largest p-values. The comparison stops at the first $p^{(s^*)} \geq \alpha_{\mathrm{HB}}^{(s)}$ and $p^{(s^*)}$ with subsequent hypotheses are directly declared non-significant, viz. let s^* be the minimal index, such that

$$p^{(s^*)} \geq \frac{\alpha_0}{m - s^* + 1} \tag{4.8}$$

all the hypotheses $H^{(1)}, \ldots, H^{(s^*-1)}$ are declared significant.

4.1.3 Results

Multiple paired t-test and Wilcoxon signed rank test of consecutive DFT vectors a_i have been assessed to find similarities in the mean tendencies of neighboring DFT vectors of the waterfall plot. The a_i values had been considered as paired observations of the same frequency bins over time. The initial segmentation processes showed high fragmentation of the signal, due to the high fluctuation of p-values around α_0 preliminary significance limit. The segmentation algorithm rejects many of $H_0^{(j)}$ implying that the DFT mean tendencies do vary significantly between many of the neighboring spectrum vectors. Practically the number of shorter segments (in-between spectrally similar) increased.

Controlling the FWER, the Bonferroni and the Holm–Bonferroni adjustment have been applied *post hoc*. Therefore, new significance levels have been calculated, and $H_0^{(j)}$ and $H_0^{(s)}$ have been reassessed.

Since the significance limits aim to lower the FWER, i.e. Type I. errors, many of *a priori* p_t- and p_W-values from the different tests were considered non-significant *post*

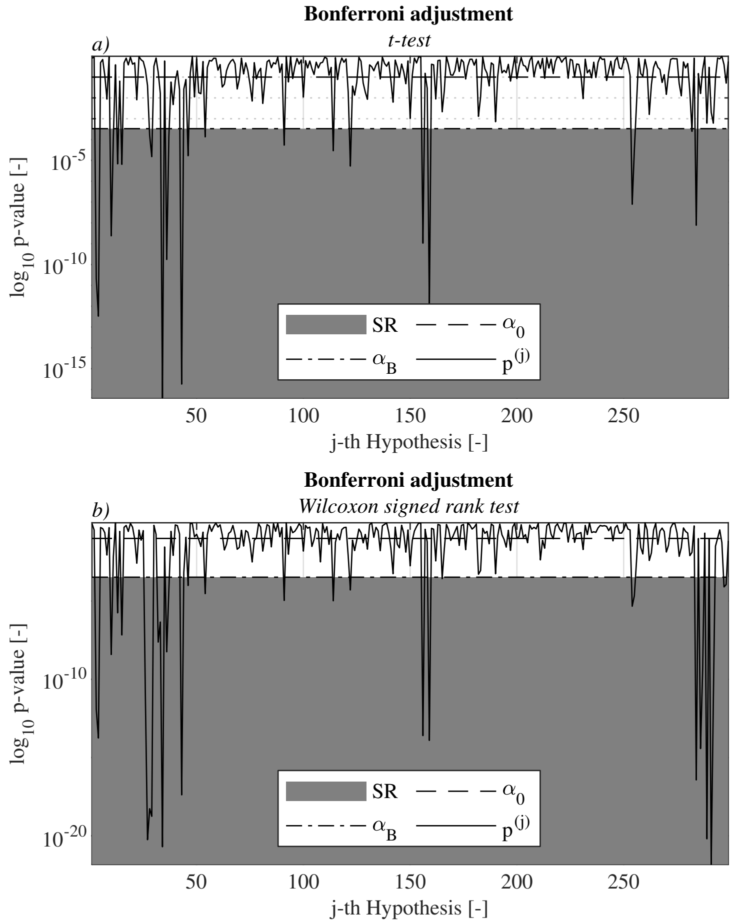

Figure 4.4: Multiple hypothesis tests with Bonferroni adjustment. The $p_{\mathrm{t}}^{(j)}$ and $p_{\mathrm{W}}^{(j)}$ are the j-th p-value from the paired t-tests, and the Wilcoxon signed rank tests respectively; α_0 and α_{B} denote the *a priori* and the Bonferroni adjusted significance limits respectively and SR denotes the significance region.

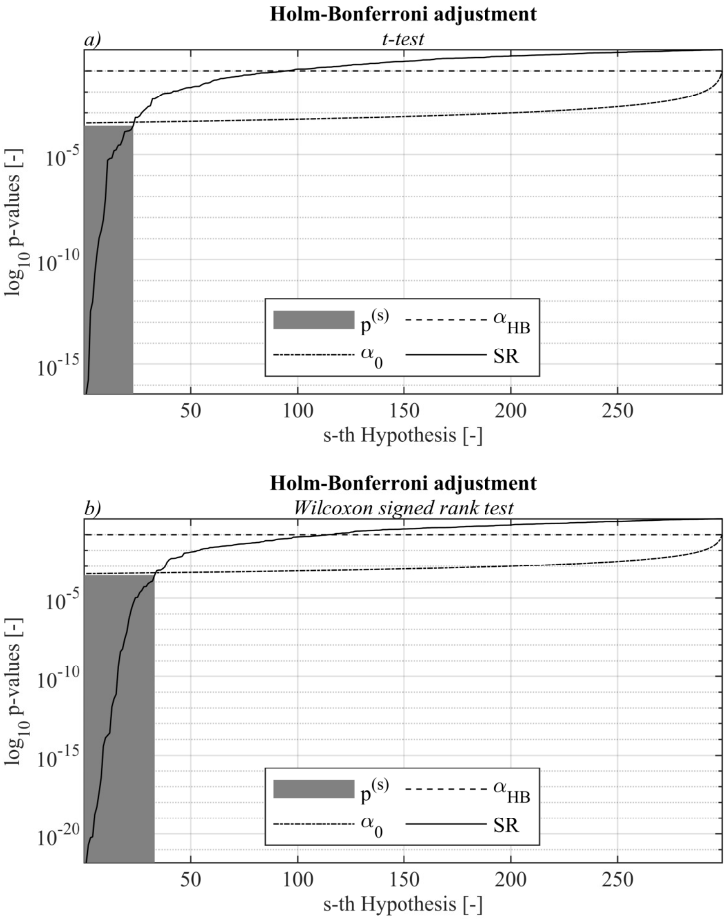

Figure 4.5: Multiple hypothesis tests with Holm–Bonferroni adjustment, with S_t and S_W significance regions for the *t*-tests and the Wilcoxon signed rank tests respectively. $p_\mathrm{t}^{(s)}$ and $p_\mathrm{W}^{(s)}$ are the sorted *p*-values from the paired *t*-test and the Wilcoxon signed rank test respectively; α_0 and α_HB denote the *a priori* and the Holm–Bonferroni adjusted significance limits respectively.

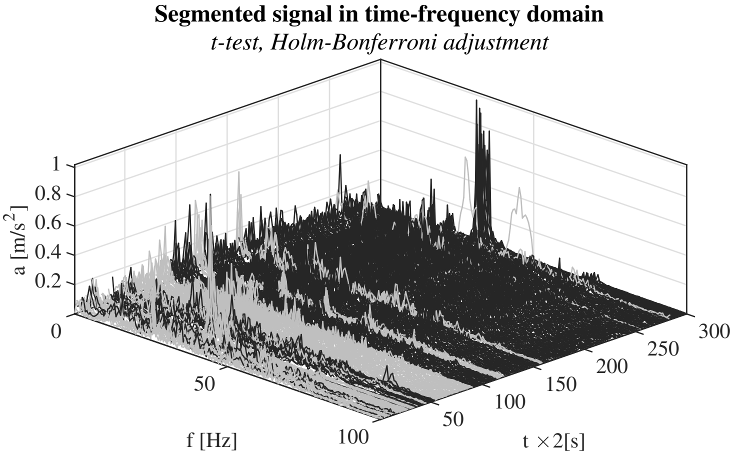

Figure 4.6: Exemplar of the segmentation results in the time-frequency domain. Different colors indicate different segments.

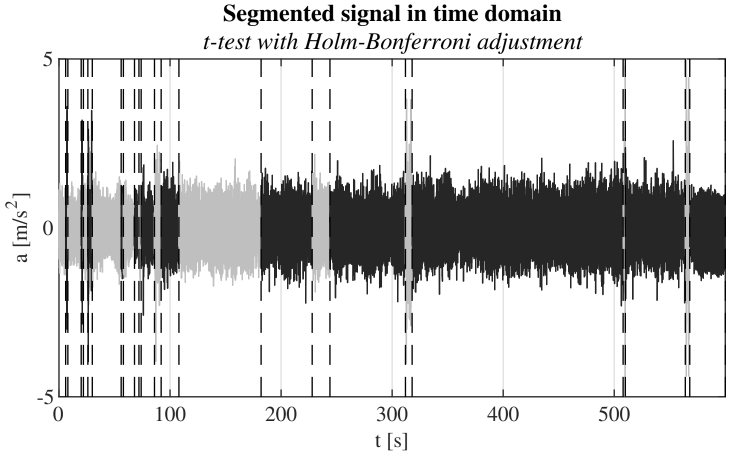

Figure 4.7: Exemplar of the segmentation results in the time domain. Vertical lines denote the section borders

hoc. Fewer truly significant findings within the same period mean that the ratio of longer segment duration increased.

The segment lengths, **L**, and -root mean squares, **RMS**, characterize the resulted segments itself, offering the possibility for the assessment of new aggregated statistics regarding their attributes, presented in Fig. 4.8. Note that the two different *post hoc* procedures gave the same solutions within either the t-test or the Wilcoxon signed rank test, which involves that the same hypotheses had been assessed as significant findings by the different α adjustments. However these identical results per *post hoc* procedures are not necessarily identical, which is further explained in the Discussion and on Fig. 4.9.

Segments lengths **L** tend to have still many shorter duration with only a few sub-series from more extended periods in both *post hoc* procedures. The **RMS** distributions show a not so fragmented picture in total. The testing of the shape of distributions is not investigated here, since the 10 min duration of current measurement is not considered significant here to draw wide-term conclusions about RVVs in general.

4.1.4 Discussion

The identical results of the two different α adjustment processes can be attributed to the same p-values in the hypotheses rejection areas per MHT, which is not a general conclusion, rather than an individual result of the current experiment. Namely, the two adjustments do not have to give necessarily the same solution (per MHT). The most condensed explanation of this can be comprehended on Fig. 4.9: first, $p_{\mathrm{t}}^{(s)}$ and $p_{\mathrm{W}}^{(s)}$ do not have values meeting any of α_{B} or $\alpha_{\mathrm{HB}}^{(s)}$. Secondly on the exemplar of $p_{\mathrm{t}}^{(s)}$, the same values are obtained above and below α_{B} and $\alpha_{\mathrm{HB}}^{(s)}$, which is the case for $p_{\mathrm{W}}^{(s)}$, as well. Therefore, in current dataset the result of segmentation has not changed between the *post hoc* procedures per type of MHT (t- or Wilcoxon-test), thus:

$$\mathbf{L}_{\mathrm{t,B}} - \mathbf{L}_{\mathrm{t,HB}} = 0 \tag{4.9}$$

$$\mathbf{RMS}_{\mathrm{t,B}} - \mathbf{RMS}_{\mathrm{t,HB}} = 0 \tag{4.10}$$

$$\mathbf{L}_{\mathrm{W,B}} - \mathbf{L}_{\mathrm{W,HB}} = 0 \tag{4.11}$$

$$\mathbf{RMS}_{\mathrm{W,B}} - \mathbf{RMS}_{\mathrm{W,HB}} = 0 \tag{4.12}$$

where the first sub-indices t or W denote the paired t-test and Wilcoxon signed rank test respectively; the second sub-indices B or HB denote the Bonferroni and Holm–Bonferroni *post hoc* procedures respectively. However, the results of segmentation approaches differentiated by the type of MHT (t- or Wilcoxon-test) do differ, which is explained by the different p-values for the hypothesis between the same neighboring DFT vectors paired. Note in Fig. 4.8 how dotted and solid lines differ at each color which is a consequence of the test statistics being different in the t-test and its non-parametric variant the Wilcoxon signed rank test.

4.1.5 Conclusion

A multiple hypothesis test procedure had been introduced in the current section in order to find spectrally similar segments within the time-frequency domain of a road vehicle vibration signal. The spectral values of neighboring DFT vectors a_i have served as the inputs of paired t-test and its non-parametric variant the Wilcoxon signed rank test. Two different *post hoc* procedures, namely the Bonferroni and the Holm–Bonferroni adjustments had been introduced after both types of test, as countermeasures against the accountable α inflation in case of MHT.

The following section will investigate the use of different statistical tests for MHT, such as the two-sample t-test and its non-parametric variant the Wilcoxon rank-sum test.

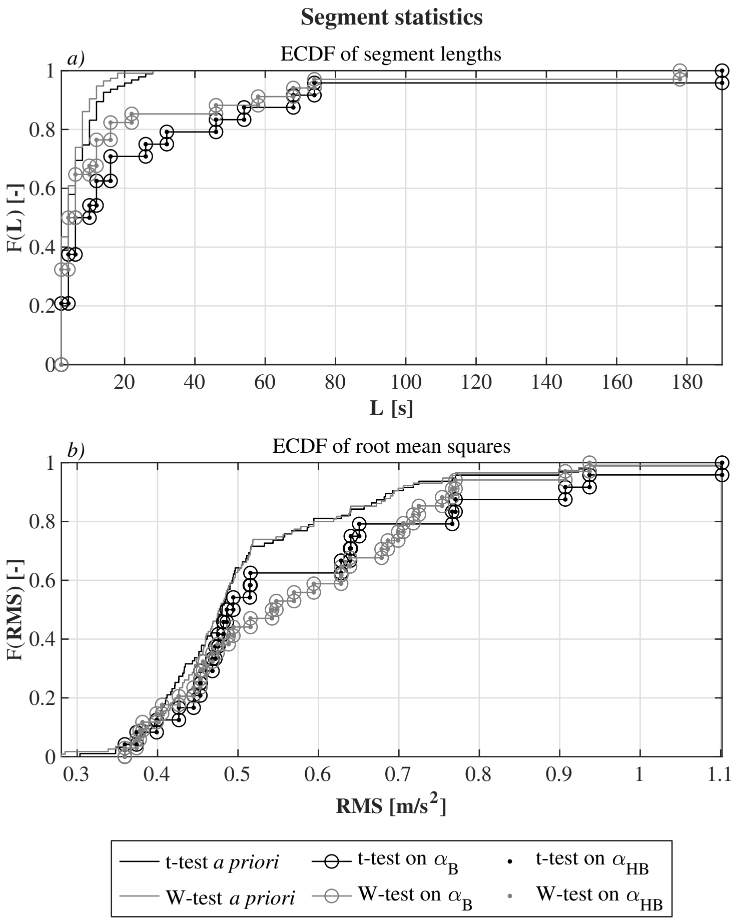

Figure 4.8: Empirical cumulative distribution functions of *a)* segment lengths, and *b)* segment RMS. The *black* lines indicate *t*-tests, *gray* shows W-tests. The symbolless *continuous* line refers to *a priori* tests. The *circles* denote the Bonferroni *post hoc* tests overlapped by *points* from the Holm–Bonferroni *post hoc* tests. Note the concentricity of *dots* and *circles*.

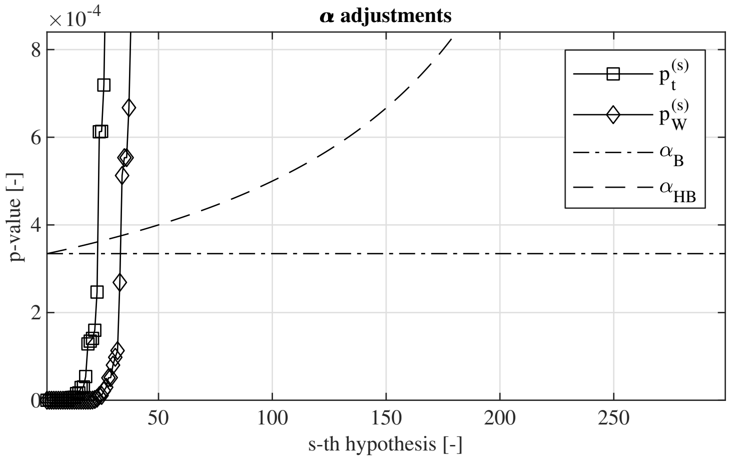

Figure 4.9: Comparison of the ascendingly sorted p-values from the t-tests (*rectangles*) and the Wilcoxon signed rank tests (*rhombus*), denoted by blue and purple lines respectively; displayed around the Bonferroni- (*dashdot*) and the Holm–Bonferroni (*dash*) adjusted α levels.

4.2 Multiple hypothesis testing by unpaired samples

Several methods have been developed for simulating non-stationary and non-Gaussian processes in packaging vibration testing, encompassing unique methods for the segmentation of road vehicle vibrations. However, only a limited number of those consider spectral characteristics. Thus, the current section introduces a novel segmentation algorithm conducted in the time-frequency domain. The spectral characteristics obtained by short-time Fourier transform are compared by Multiple hypothesis tests (MHT) to find changepoints in a RVV sample. Again, *post hoc* procedures are investigated against the inflating Type I. error.

4.2.1 Methods

Investigation of the auto-correlation function (ACF) determines a limit above which the signal is considered independent of previous periods. The STFT uses this limit. One vector is a discrete Fourier transform (DFT) with elements $a_{i,k}$ over the bandwidth $i = 0, 1, \ldots, 100$ Hz at instants $k = 1, 2, \ldots, 600$ s. The idea to highlight here is that $a_{i,k}$ has individual distributions at any k. Note that this is not a spectral density but a probability density of the DFT magnitudes, see Fig. 4.10. The logarithm on base 10 of the STFT serves as input for the MHT procedures. Two sample t-tests MHT_t and Wilcoxon rank sum tests [108, p.25-3], MHT_W, assess the similarities among adjacent sections of log-STFT. Afterward, the Bonferroni and Holm–Bonferroni adjustments are introduced against the inflating Type I. error. Hypotheses considered truly significant *post hoc* yield the borders of segments.

The RVV signal [110] is measured on a passenger car's cockpit sampled with 1 kHz during a 10 min long journey. Its auto-correlation is investigated in Fig. 4.11 and a one second limit is assumed sufficiently long to ensure a quasi-independent state of samples for the MHT. Thus, STFT in Fig. 4.12 is obtained with 1 s long windows. Because the distribution of the original STFT is heavily skewed towards lower magnitudes, a logarithmic transformation is applied to the STFT, yielding a more symmetric representation of the magnitude histograms per second in Fig. 4.10.

The STFT resulted in $K = 600$ sections, offering $J = 599$ comparisons per MHT. Despite the higher Nyquist frequency, the STFT are band-limited to the [0,100] Hz interval. Central tendencies are compared by the t- and rank sum tests to find similar segments among neighboring magnitude densities per second on the preliminary significance level of α_0. The resulted series of p-values are compared to differently adjusted significance levels introduced in the α adjustment section.

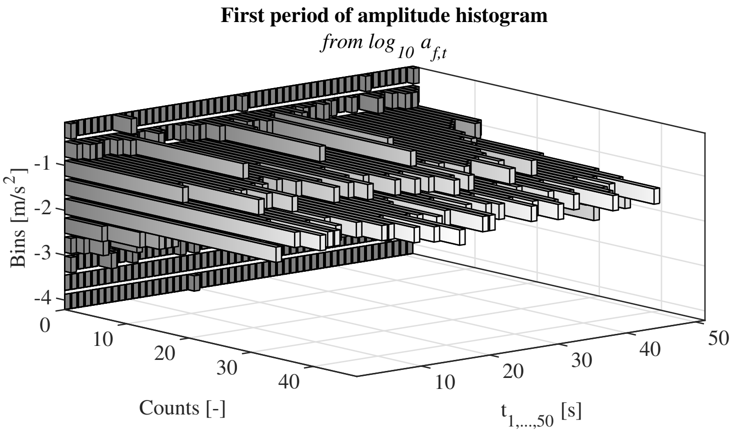

Figure 4.10: Histogram of DFT magnitudes in the first 50 s of log-STFT vectors.

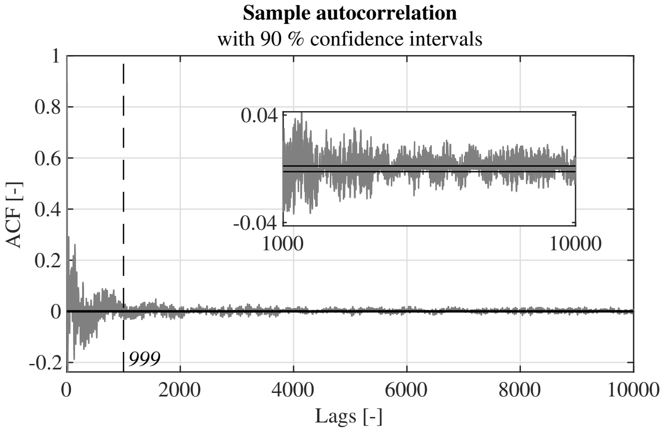

Figure 4.11: Indication of the chosen limit of high auto-correlation at 999 lags; auto-correlation function of the signal (*gray*) and 90% confidence interval (*black*).

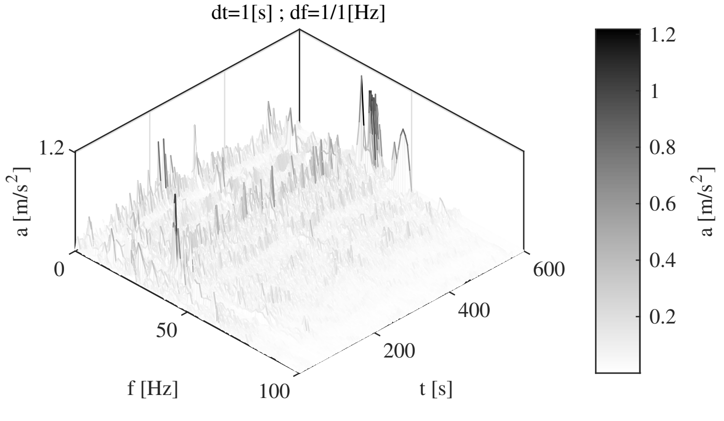

Figure 4.12: Short-time Fourier transform of the vibration signal.

Two-sample t-test

Statistical inference can be made about the null hypothesis of two samples, x, y having the same mean, using the two-sample t-test (also known as unpaired t-test). The alternative hypothesis formulates inequality among the means

$$\begin{cases} H_0 : \overline{x} = \overline{y}; \\ H_A : \overline{x} \neq \overline{y}. \end{cases} \tag{4.13}$$

The two-sample t-test is a parametric test that compares location parameters of two independent samples. Assuming equal variances of populations, the test statistic under H_0 has Student's t-distribution with $\nu = n_x + n_y - 2$ degrees of freedom, and the pooled standard deviation replaces the sample standard deviations. Assuming unequal variances of the two samples, the test statistic under the H_0 has an approximate Student's t-distribution with the number of degrees of freedom given by Satterthwaite's approximation. This test is sometimes called Welch's t'-test [118].

Wilcoxon rank sum test

The Mann-Whitney U-test "*is the non-parametric equivalent of the t-test for means*" [119]. Albeit not the same procedure, the "*Wilcoxon rank sum test is equivalent to the Mann-Whitney U test*" [120]. If t-test criteria cannot be entirely met, the non-parametric Wilcoxon rank sum test may be implemented to assess the null hypothesis that two samples belong to populations with equal medians.

Multiple hypothesis testing

This section investigates the assumptions of the t-test and formulates the MHT configuration. The Bartlett test of the null hypothesis assuming homoscedasticity returned a p-value of 0.00. That is, the log-STFT function does not have equal variances over time, which is not surprising. Still, two adjacent log-DFT vectors might have equal variances, which remains uninvestigated. This is done on purpose, as it is not suggested to automate the choice of test (parametric or non-parametric) based on the test of variances [121, p.298]. Also, there is not a consensus choosing a test in case of heteroscedasticity (ibid.). Since already a log-transformation is introduced, the current chapter stays at t-test, assuming equal variances. The Anderson–Darling tests of the log-DFT vectors showed normality 188 times; still, the t-test is robust to the assumption of normality [108]. Under the same circumstances, the Wilcoxon rank sum test is utilized in another MHT. The MHTs are formulated as

$$\begin{cases} H_0^{(j)} : \overline{a}_{i,k} = \overline{a}_{i,k+1}; \\ H_A^{(j)} : \overline{a}_{i,k} \neq \overline{a}_{i,k+1}. \end{cases} \tag{4.14}$$

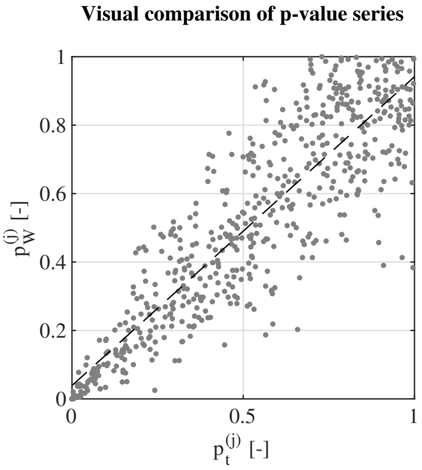

Figure 4.13: Least squares fitted line (*dashed*) to emphasize similarities between p-values from t-tests $p_t^{(j)}$ and rank sum tests $p_W^{(j)}$.

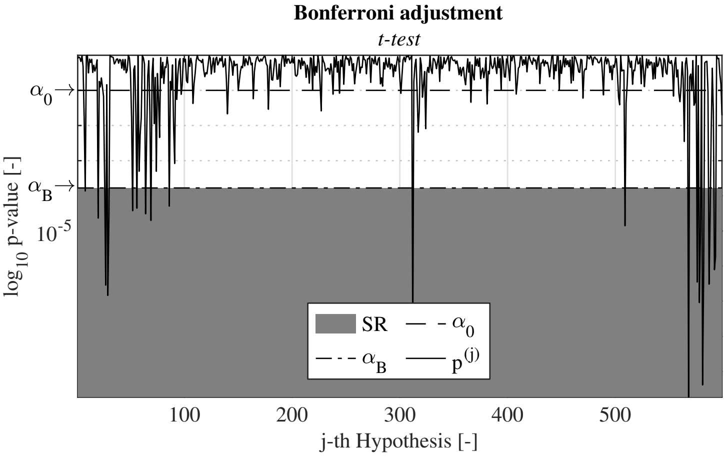

Figure 4.14: Bonferroni adjustment α_B of the preliminary significance limit α_0 beneath $p_t^{(j)}$ yielding SR significance region.

for $k = 1, 2, \ldots, J$, expressing the test of central tendencies (subsequently centers) among the k and $k+1$-th vectors. Not rejecting $H_0^{(j)}$ shows two consecutive DFT vectors having the same centers, hence an association among the vectors. Conversely, rejecting $H_0^{(j)}$ in favor of $H_A^{(j)}$ indicates neighboring vectors not having the same centers, thus a dissimilarity among them. In the case of a significant result, a new segment is initiated. Current MHT are deployed on $\alpha_0 = 0.10$ preliminary significance limits. Although many tests are found significant preliminary, not all of them may be considered truly significant due to α inflation resulting from simultaneous testing.

Countermeasures against α inflation, as the Bonferroni adjustment in Sec. 4.1.2 and the Holm–Bonferroni adjustment in Sec. 4.1.2 are similarly investigated here, depicted in Fig. 4.14 and in Fig. 4.15, respectively.

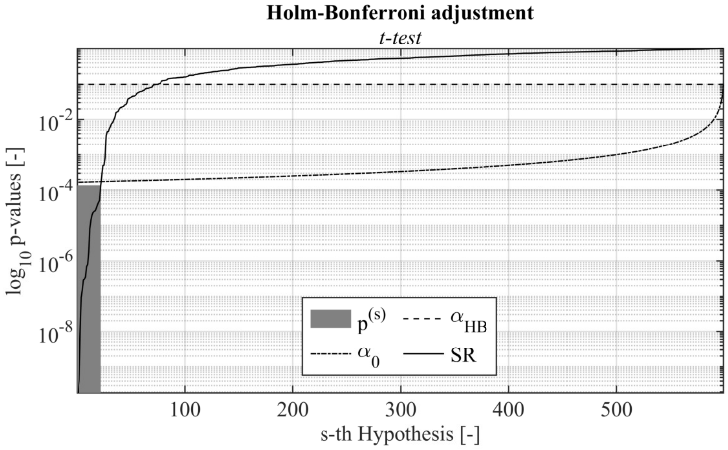

Figure 4.15: Holm–Bonferroni adjustment α_{HB} of the preliminary significance limit α_0 beneath $p_t^{(s)}$ yielding SR significance region.

4.2.2 Results

The findings of current investigations are summarized as follows:

a. $\mathrm{MHT_t}$ and $\mathrm{MHT_W}$ behave similarly (Fig. 4.13), yielding similar but not identical *p*-values for hypotheses at the same locations.

b. Given $\mathrm{MHT_t}$, the Bonferroni and Holm–Bonferroni *post hoc* procedures yield the same hypotheses significant in $p_t^{(j)}$ and $p_t^{(s)}$.

c. Similarly, given $\mathrm{MHT_W}$, $p_W^{(j)}$ and $p_W^{(s)}$ declares the same hypotheses significant.

d. *Post hoc* currently, one difference is noticeable between $\mathrm{MHT_t}$ and $\mathrm{MHT_W}$, observable between Fig. 4.19.*b-c)* at $j = 8$, thus between $t = (7, 8]$ and $(8, 9]$ s.

e. *Post hoc* tests result in fewer segments compared to the preliminary tests.

f. Frequency modulation does not affect the presented method, e.g., 100–300 s.

g. Magnitude modulation affects the presented method, e.g., $j = 593$, thus between $t = (592, 593]$ and $(593, 594]$ s. By magnitudes, the Fourier coefficients are understood.

4.2.3 Discussion

This section introduced variations on MHT procedures supplemented by the same *post hoc* tests to find segments in the spectrogram. The methods provide the following contributions.

a. The t-test assumes normality, the rank sum test requires symmetry in distributions. Despite the above-discussed assumptions assured to a certain extent, this is considered a good sign of the robustness of $\mathrm{MHT_t}$ and $\mathrm{MHT_W}$, yielding preliminary only 15 differences.

b. $\mathrm{MHT_t}$ *post hoc* corrections do not yield different alternative hypotheses because the same p-values are in the different significance regions.

c. It is similarly valid for $\mathrm{MHT_W}$ per *post hoc* adjustments.

d. The scattering in Fig. 4.13 presents that the MHT procedures do not yield the same p-value series, as expected. This scattering is also observable in the low p-value regions between $p_t^{(8)}$ and $p_W^{(8)}$.

e. The moderated number of significant p-values *post hoc* is again an expected behavior since it is aimed to reduce the family-wise error rate. A thought experiment in Fig. 4.18 shows the *post hoc* test's behavior as a function of number p-values for 599 and 5990 instances. With an increasing number of tests, *post hoc* procedures yield stricter limits.

f. It is not good observable from the data (Fig. 4.16) but theoretically justifiable that the simple rearrangement of the elements in a log-DFT corresponding to, (e.g., at 34 s) would hold the same elements with different peak location. This should not yield a different magnitude distribution of the DFT vector.

g. Strong magnitude modulation occurring in the spectrogram can significantly manifest itself in the magnitude distribution of log-DFT elements (Fig. 4.17), representing the algorithm's capability to detect magnitude modulation.

Albeit the current findings apply only to the given 10 min long measurement (which cannot be referred to as a representative sample of RVV worldwide) the approach demonstrates promising results. Nevertheless, the method allows declaring segment-borders by well-established hypothesis tests instead of a heuristic *try-and-error* weighting of parameters.

4.2.4 Conclusion

Segments within a spectrogram can be found, in-between homogeneous to a specific criterion. Different spectrums might simulate homogeneous segments in packaging vibration testing. Only a few segmentation methods investigate spectral properties, considering the discipline of PVT. Nevertheless, the number of techniques using objective hypothesis test is alarmingly low. Thus, the current section introduced Statistical Spectrogram Segmentation (3S), an algorithm capable of detecting magnitude modulation in the

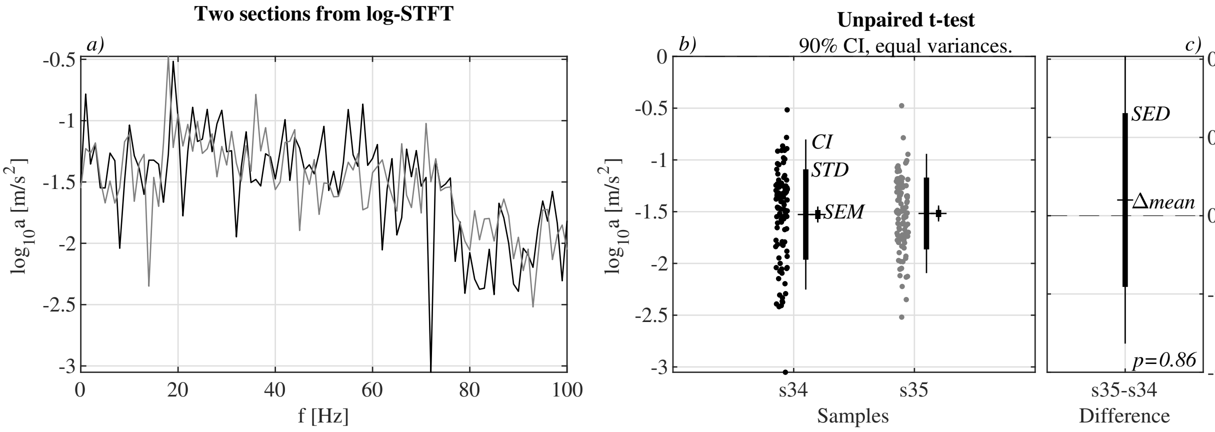

Figure 4.16: The unpaired t-test between 34–35th log-DFT vectors showing a slight frequency modulation; STD (standard deviation), CI (confidence interval), SEM (standard error of the mean), SED (standard error of difference).

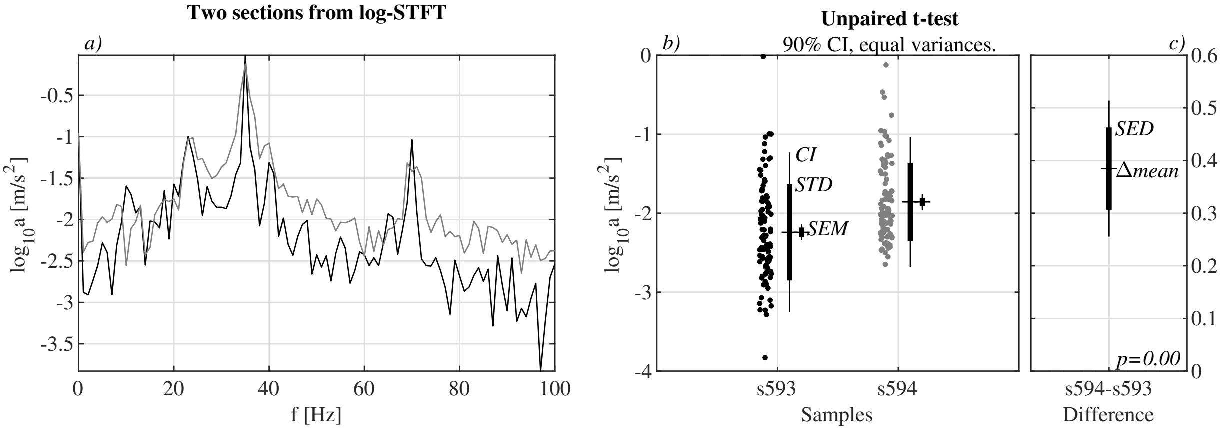

Figure 4.17: The unpaired t-test between 593–594th log-DFT vectors showing magnitude modulation, notations similarly to Fig. 4.16

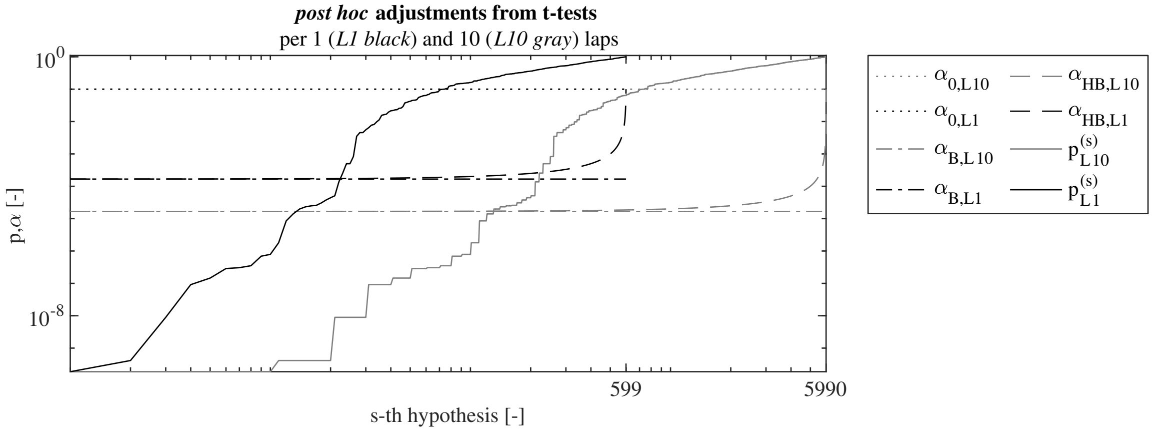

Figure 4.18: A thought experiment of traveling the same rounds resulting in the same p-values per laps, but the significance limits from the Bonferroni and Holm–Bonferroni procedures differ at every round, e.g., $\alpha_{\mathrm{B},L_1} \neq \alpha_{\mathrm{B},L_{10}}$ or $p^{(s^*)}_{\mathrm{HB},L_1} \neq p^{(s^*)}_{\mathrm{HB},L_{10}}$.

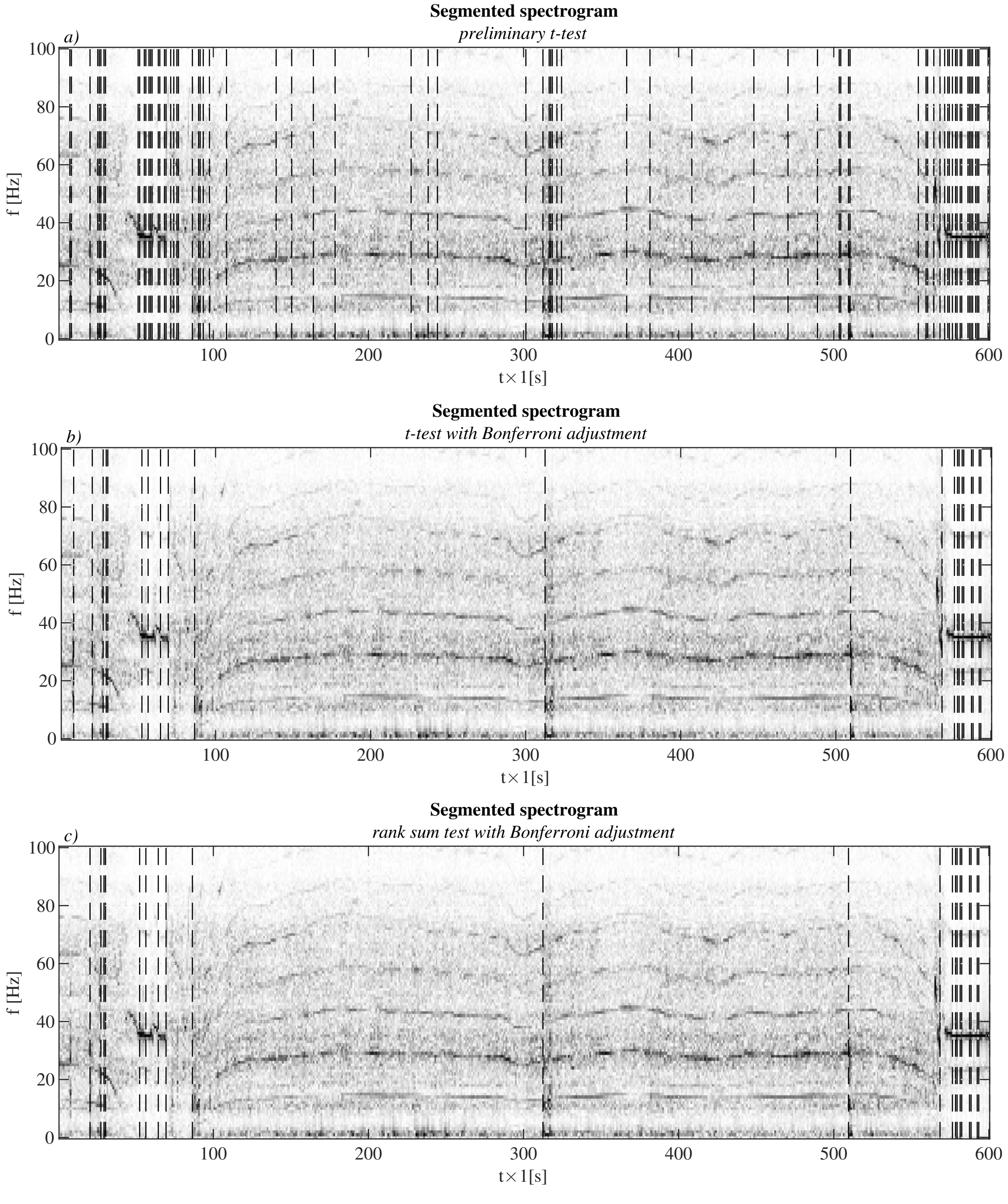

Figure 4.19: Result of segmentation projected on the STFT surface. Dashed vertical lines denote segment borders; *a)* t-test on the preliminary significance limit α_0; *b)* t-test with Bonferroni adjustment; and *c)* rank sum test with Bonferroni adjustment.

time-frequency domain of RVVs. The segmentation is achieved by two MHT procedures supplemented by *post hoc* corrections. Overall, four implemented variations show good agreements. Therefore, the idea of MHT for RVV segmentation accounting magnitude modulation shows a straightforward and objective solution.

Thesis 3. The surface formed by short-time Fourier amplitude spectrum can be segmented in the time-frequency domain due to the temporal variation of the inherited spectral shape. This can be done by applying paired-sample- and two-sample t-tests to the Fourier coefficients of adjacent-to-adjacent amplitude spectra. ■ *Ref.*: [6, 7]

4.3 CUSUM-type changepoint detection

Non-stationary random vibrations gained increasing interest in vibration testing. A changepoint detection procedure often manages the decomposition of Road vehicle vibrations (RVV) when analyzing the recorded series. The current chapter introduces the CUSUM-type changepoint detector (CpD) from Chapter 2. Some sub-steps are restated for completeness, while others are investigated in more detail. In fact, this section serves as a bridge toward the forthcoming methods.

4.3.1 Methods

The same source signal [110] is analyzed to present the detector comparably. Main concepts are also restated below for completeness. The changepoint detector operates on one-dimensional vectors; therefore, the two-dimensional short-time Fourier transform (STFT) matrix should be described uniquely. For this reason, the spectral centroid, -spread, -skewness, and -kurtosis, respectively $\mu_{i,j}$, for $i = \{1,2,3,4\}$-th spectral moments, at $j = 1,2,\ldots,J$ seconds across each $k = 1,2,\ldots,K$ frequency bins. For completeness Eq. 2.2–2.5 are recalled:

$$\mu_1 = \frac{\sum_{k=b_1}^{b_2} f_k s_k}{\sum_{k=b_1}^{b_2} s_k}$$

$$\mu_2 = \sqrt{\frac{\sum_{k=b_1}^{b_2} (f_k - \mu_1)^2 s_k}{\sum_{k=b_1}^{b_2} s_k}}$$

$$\mu_3 = \frac{\sum_{k=b_1}^{b_2} (f_k - \mu_1)^3 s_k}{\mu_2^3 \sum_{k=b_1}^{b_2} s_k}$$

$$\mu_4 = \frac{\sum_{k=b_1}^{b_2} (f_k - \mu_1)^4 s_k}{\mu_2^4 \sum_{k=b_1}^{b_2} s_k}$$

are calculated [77, pp.371, 281, 299, 317], on view in Fig. 4.20. The four spectral descriptors of a sample are introduced to the algorithm in Fig. 4.23. The resulting four series of changepoints are concatenated and handled as the final segmentation in the time-frequency domain. In a CUSUM scheme, the cumulated sum of differences $\mu_{i,j} - \overline{\mu_j}_i$, such as Eq. 2.10,

$$S_{i,k} = \sum_{j=1}^{J} (\mu_{i,j} - \overline{\mu_j}_i). \tag{4.15}$$

can evaluate sudden changes in the mean tendency, indicating a Candidate changepoint ($\mathrm{Cp_c}$), a corresponding exemplary depiction can be found in Fig. 4.22. As introduced in

Chapter 2, the following step excavates resampling techniques to assess the significance of $\mathrm{Cp_c}$. The method is based on Eq. 3.2 such that an actual sub-series $\mu_{i,j}, j \in [L_j, R_j]$ is rearranged as of j, an N number of times. Every time a permuted sample produces a more extreme test-statistic, $\hat{S}_r$, than the observed one, $\hat{S}_{(i,j)}$, from the original sample, the approximated p-value increases by $1/N$ starting from $p = 0$:

$$\tilde{p} = \frac{1}{N} \# \left\{ \hat{S} < \hat{S}_r \right\}. \tag{4.16}$$

The test statistic utilizes the same equation above (Eq. 2.10). Given that the approximated p-value stays below the threshold α, the changepoint is considered positive, i.e., $\mathrm{Cp_c} \rightarrow \mathrm{Cp}$. Finally, each subsection is subjected to the same steps until any exit conditions are encountered.

Once all four spectral moments are segmented, the series of changepoints are concatenated, unique elements are sorted out, then ordered ascending

$$\Gamma = \# \left\{ \bigcup_{i=1}^{4} \gamma_i \right\}.$$

Fig. 4.20 presents the STFT matrix overlaid by CP from the four spectral moments, beneath, individual spectral moments with corresponding changepoints are indicated. The CpD is run at $\alpha = 0.05$ significance level, using $R = 10^4$ permutations.

4.3.2 Results

The STFT matrix is segmented over time, and each changepoint is considered valid in the whole width of the frequency domain. The underlying reason is that agglomerate statistics are analyzed in the form of spectral moments, i.e., any of Eq. 2.2–2.5 uses every frequency bin in the summation. The result of segmentation is depicted in Fig. 4.21, revealing mostly plausible results. The strong harmonic components around $\sim$ 75 s and $\sim$ 550 s are found, each being segment. The latter recording section holds another changepoint at $\sim$ 575 s found by spectral skewness in Fig. 4.20.*d)*. Other instances in the STFT might be judged by human eyes as they were lacking changepoints, e.g., harmonic components decrease until 300 s, after that increase. Also, an intermittent frequency modulation can be found in the whiter region around $\sim$ 75 sec. It is apparent that neither the current procedure escapes false negatives. Besides, one could rightly suppose also false positives, investigated in the next chapter.

Although, the fact of changepoints being present is not always enough. The current thesis aims to provide a simulative approach based on the spectral characteristics, but the question of how long a spectrum should be simulated is partially postponed to Chapter 6. The most convenient appraisal remains the distribution of the segment

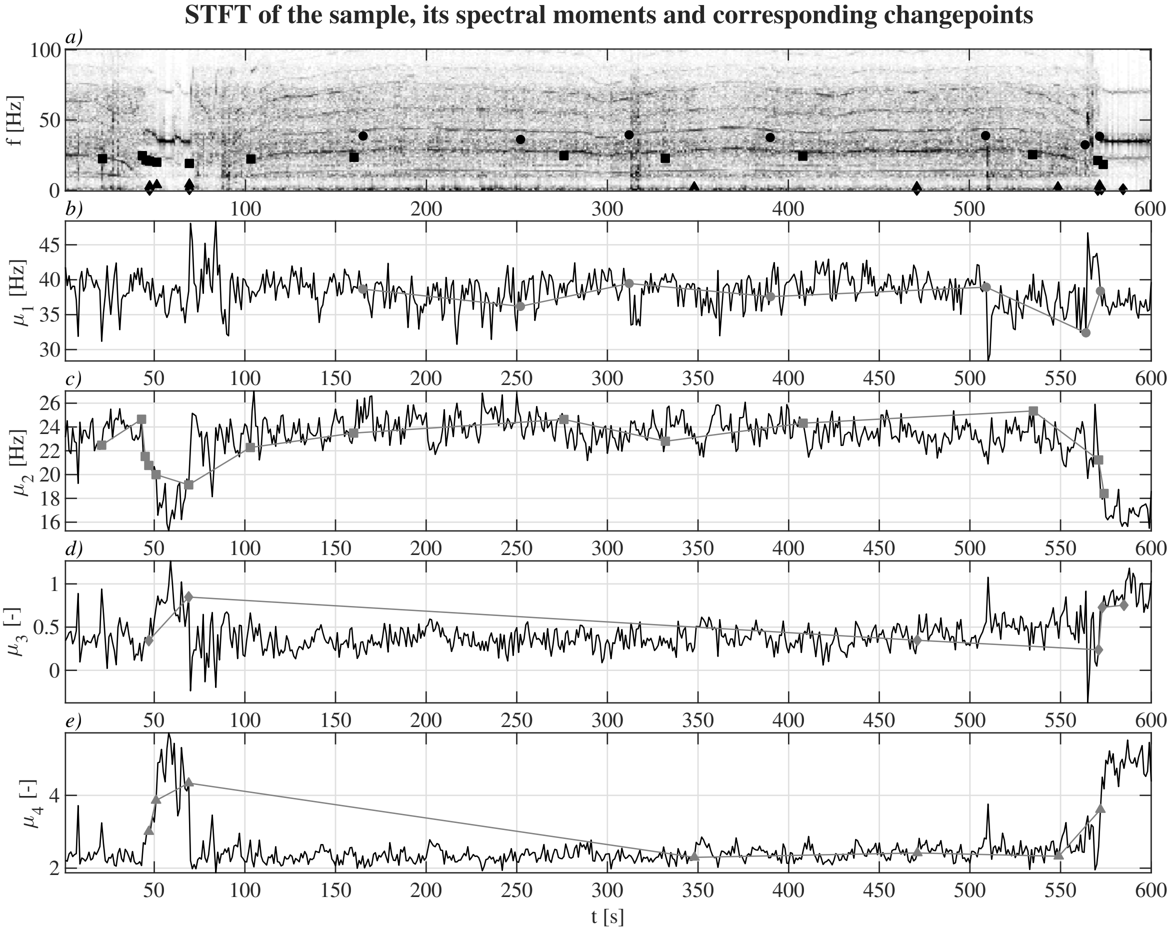

Figure 4.20: Segmentation by CUSUM of recording [110]. Pane *a)* shows the short-time Fourier transform (STFT) plane overlaid by changepoints (*black*). Subsequent panes show the spectral moments (*black*), such as: *b)* spectral centroid, *c)* spectral spread, *d)* spectral skewness, and *e)* spectral kurtosis, with the corresponding changepoints (*gray*). Note that changepoints are connected by solid gray lines only to ease the readability.

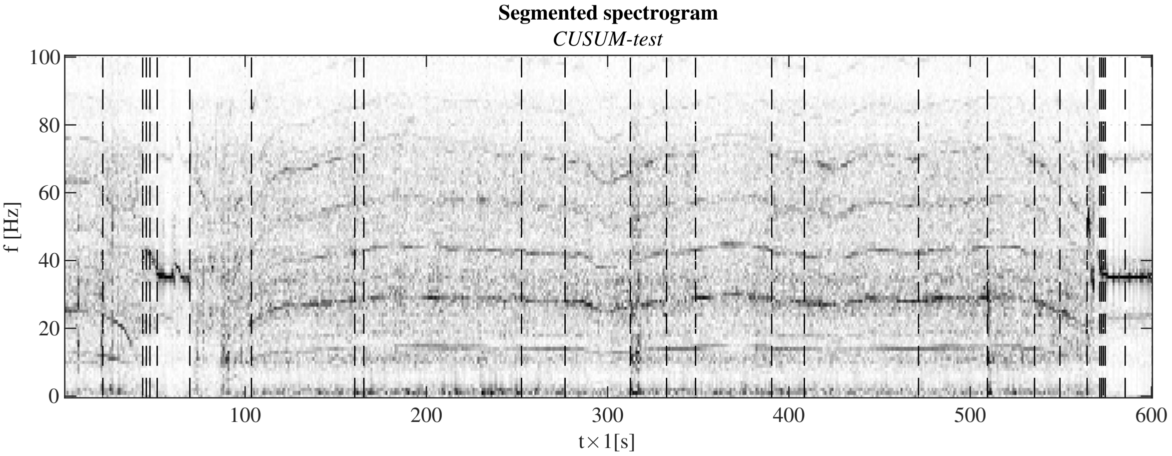

Figure 4.21: Segmented spectrogram by the CUSUM method, *dashed* lines indicating global changepoints.

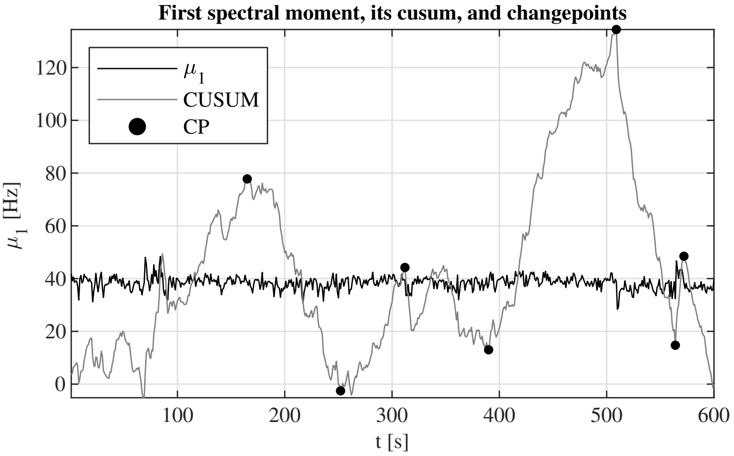

Figure 4.22: The spectral centroid of the recordings (*black*) with its first, total cumulative sum (*gray*) and the found changepoints (*circles*).

lengths, L, accompanied by the RMS content, R. The probability mass functions of the two statistics are to be found in Fig. 4.24. Interestingly, the typically assumed normal- or uniform distributions would have been a seriously departed guess from the actual observations. While the current section does not aim to fit distributions and overlooks the test for normality or uniformity, a quick look at them should be a subjective but sufficient justification. Its practical consequence holds that

a. the spectral characteristic does not vary in such usual patterns (normal or uniform),

b. the segment length distribution is heavily left-skewed,

c. the RMS content distribution is moderately right-skewed.

One can expect many short segments and only a few long-sustained segments. Also, one can expect only a few low RMS sections during a trip, a typical vibration level, and some higher RMS sections. The joint distribution will be introduced in the Discussion.

4.3.3 Discussion

It can be understood that the CpD inherently uses prior statistics; in fact, the two steps of spectral moment calculation and the changepoint detection are fundamentally different. Therefore, much of the efficacy in CpD is predestined by its inputs. To find candidate changepoints, thus, sufficiently varying inputs are necessary. Chapter 2 derived the degree of non-stationarity, which is a posterior observation. Prior analyses may understand the variability, first, in the FD moments. Fig. 4.20.*b–e)* showed this variability in a promising fashion. Those are assessed in Fig. 4.24 in the probability domain, appended to the segment RMS distribution. Of course, not every segment length can mimic any RMS content; therefore, the joint distribution is favorable. Such

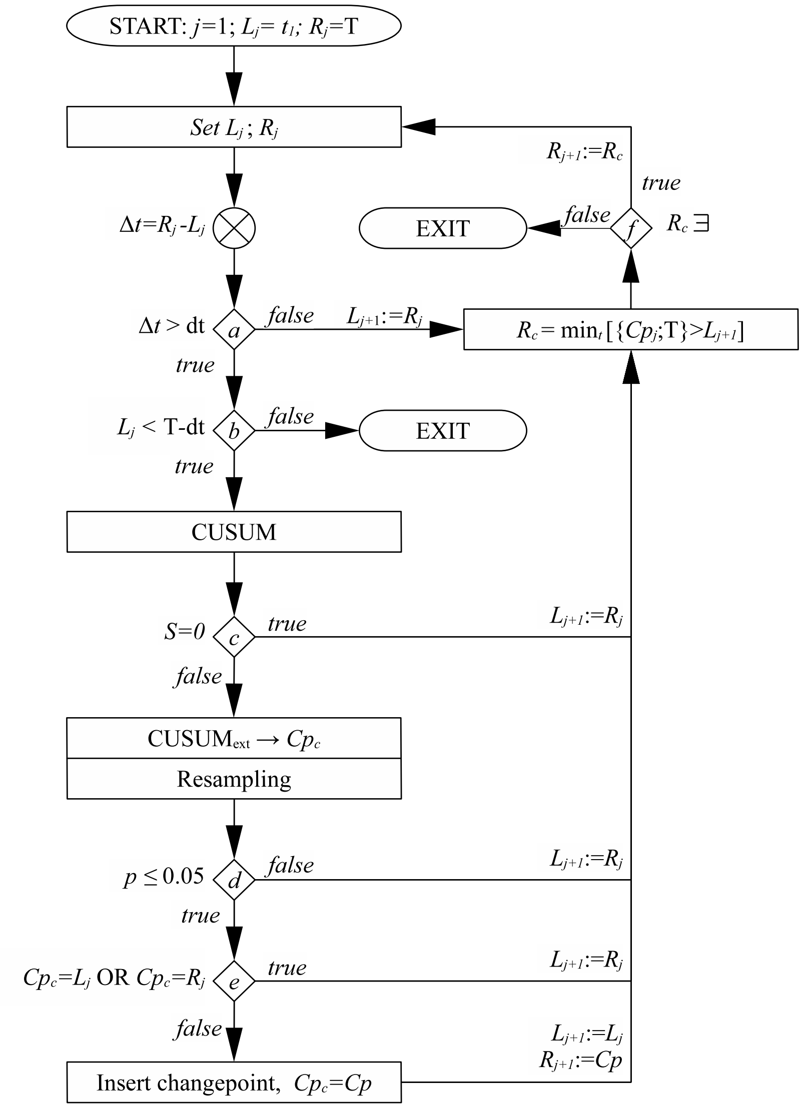

Figure 4.23: A CUSUM-type changepoint detection framework. Let L_j and R_j denote respectively the left and right boundaries of a sample of length T or its sub-sample. Also, let dt denote the minimum segment length, here 1. The CUSUM points to a candidate changepoint $\mathrm{Cp_c}$, which, if considered significant, becomes Cp. The procedure runs until no more changepoint can be found, or an exit condition is met.

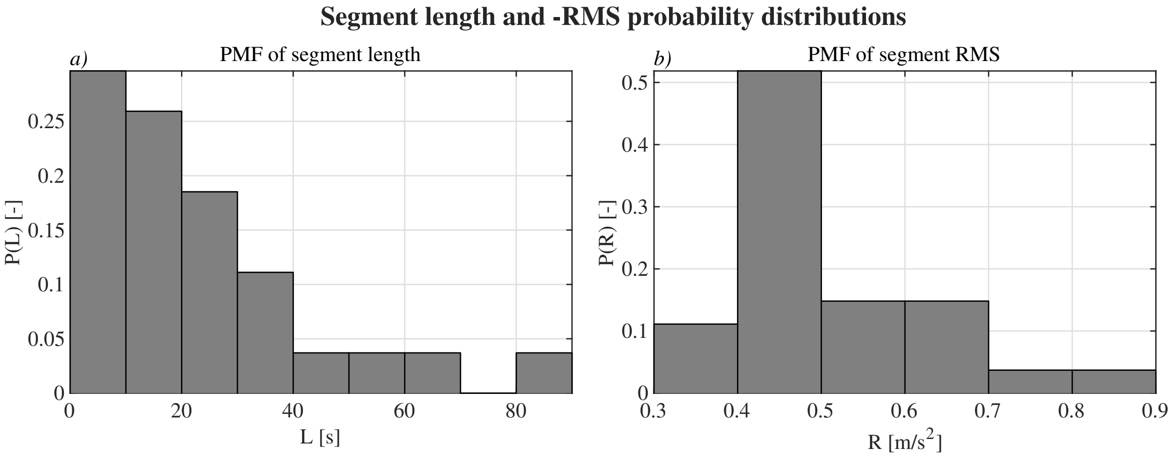

Figure 4.24: Probability mass function of segment lengths in pane *a)*; and -RMS in pane *b)*.

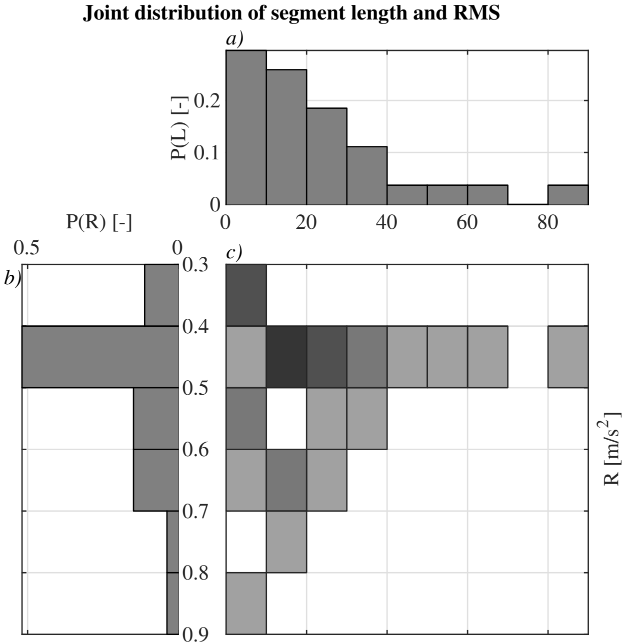

Figure 4.25: Joint distribution of probability mass functions in pane *c)*. Pane *a)* shows the probability mass function of segment RMS contents, and pane *b)* the probability mass function of segment lengths. Note, we cannot assume any pair of segment length and RMS content.

Table 4.3: Coefficients of variation [%] for the first four spectral moments in two measurements.

[%]	cv [μ_1]	cv [μ_2]	cv [μ_3]	cv [μ_4]
[110]	6.32	9.14	47.42	27.02
B	13.97	7.03	42.07	25.61

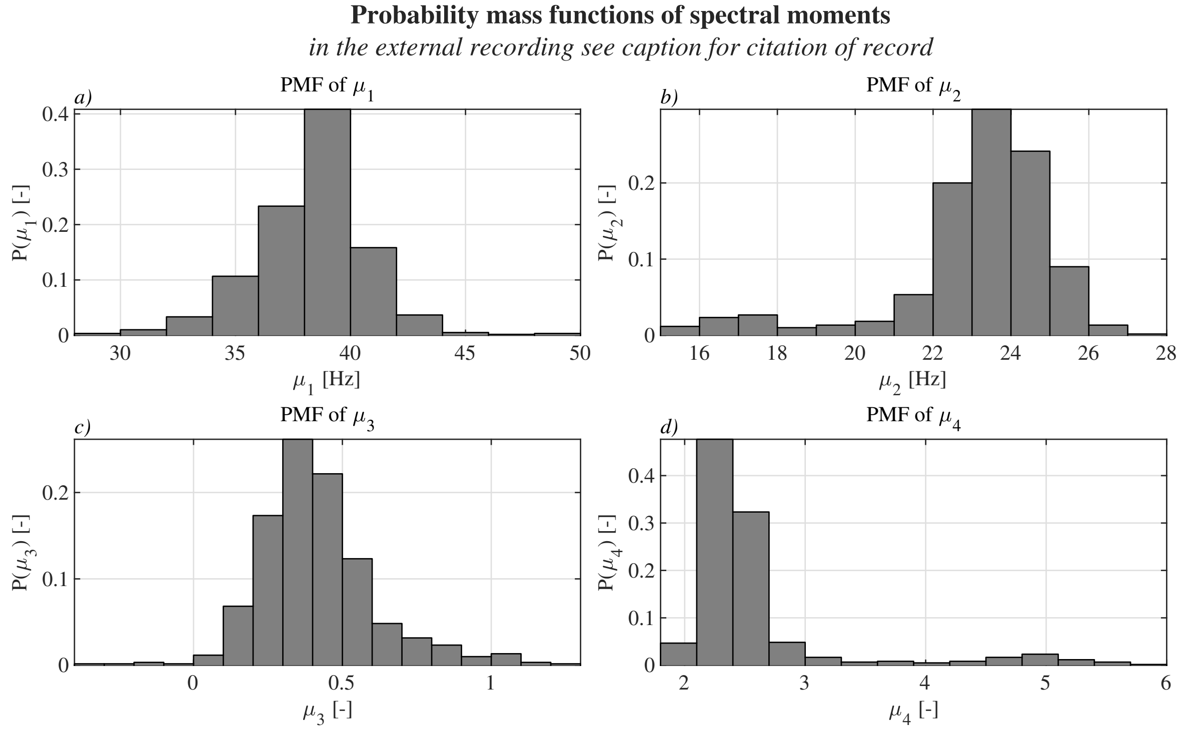

Figure 4.26: Spectral moments' distributions of recording [110], such as *a)* spectral centroid, *b)* -spread, *c)* -skewness, and *d)* -kurtosis.

a map is illustrated in Fig. 4.25. Sample B from Chapter 2 is chosen for verification because it has similarly one longer stop at a red light during the trip, and the gauge was also installed on the cockpit. The pre-processing covered the numerical elimination of the DC frequency but had been band-limited up to 100 Hz to facilitate the comparison with measurement in [110]. The spectral moments in the two measurements are in certain proximity regarding central and range tendencies. The shape of distributions in Fig. 4.26 better expresses the mix of travel and presumably stop sections; Fig. 4.27 shows that tendency moderately. It is worth noting the severe coefficient of variations, cv $= \sigma/\overline{x}$, reported in Table 4.3.

4.3.4 Conclusion

The most widely used assumptions—when facing an unknown phenomenon—of normality and uniformity has been alleviated by the analysis regarding the segment length and -RMS distributions. In fact, the referred distributions are respectively heavily- and

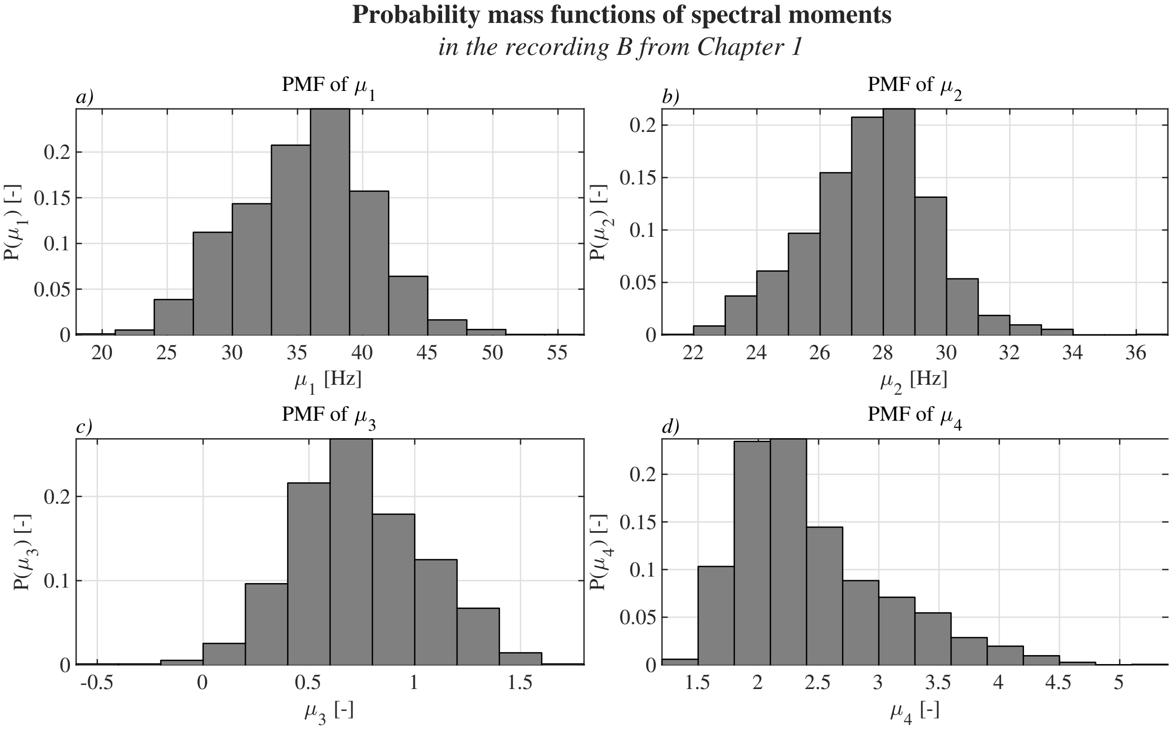

Figure 4.27: Spectral moments' distributions from the measurement B (in Chapter 2), such as *a)* spectral centroid, *b)* -spread, *c)* -skewness, and *d)* -kurtosis.

moderately right-skewed. Thus, it necessitates investigating the joint distribution to find pairs of typical RMS content on typical length. The word, typical is emphasized.

The spectral moments in RVV are likely to show up severe coefficient of variations, which facilitates changepoint detection. If changepoints exist, the introduced algorithm shows the borders, where the mean of the input signal is likely to change. Therefore, the mean varies in subsections, and it rightly suggests a varying probability structure, hence non-stationarity.

4.3.5 Postscript

Chapter 2 introduced available tests for non-stationarity and pointed out inconsistencies. The principal definition of strong and wide sense non-stationarity of stochastic processes is cumbersome to justify either from one realization, even from an ensemble.

Let us suppose that an infinitely long measurement is obtained. Apart from the DC component, i.e., observing only the relative accelerations, the travel would be most likely to start and end at zero accelerations. We may conclude in practical terms that the process is stationary.

Let us further suppose that the infinitely long measurement could be reproduced many times, perfectly in the same trajectories, so we may obtain an ensemble. If the distributions along the *randomness*, Ω, do not change with time, we may conclude also in statistical terms, that the process is stationary.

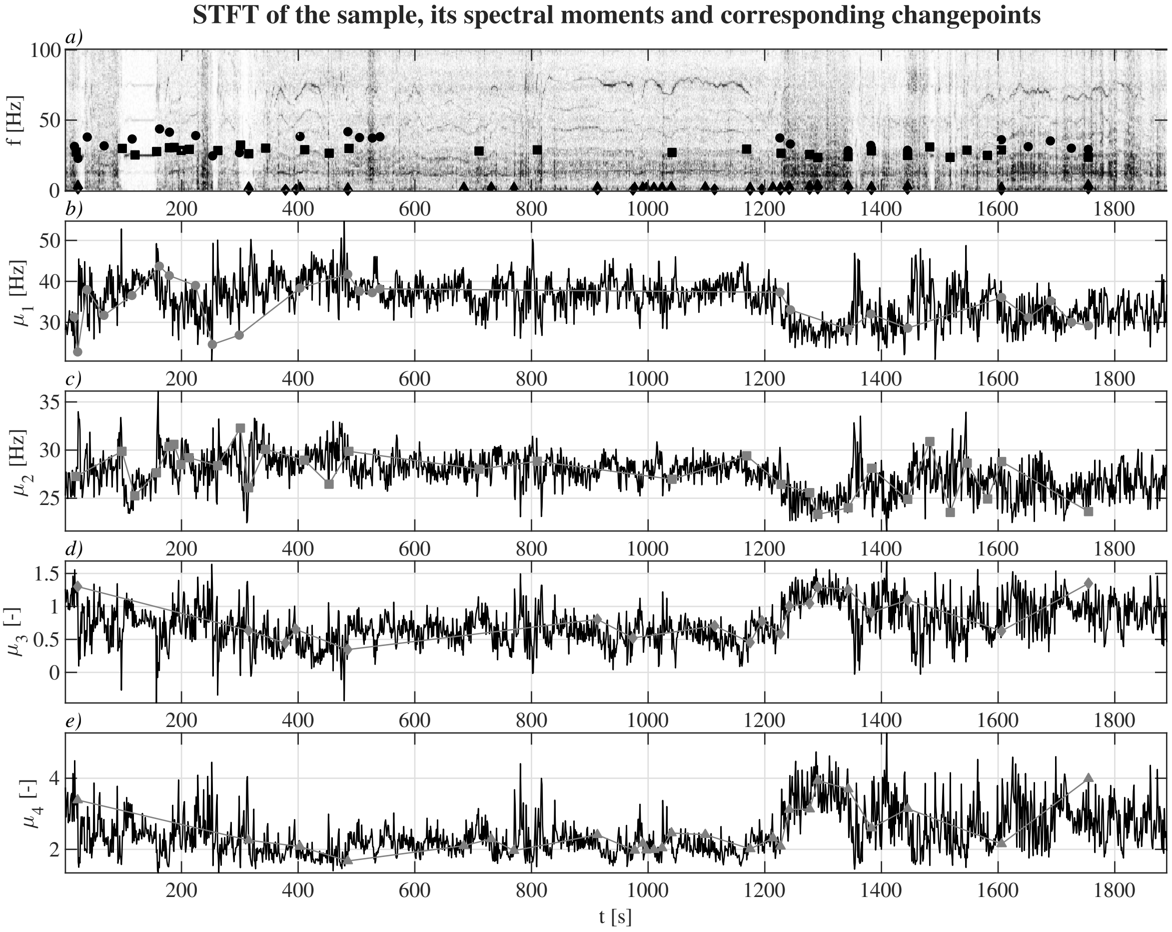

Figure 4.28: Segmentation by CUSUM of recording B. Pane *a)* shows the short-time Fourier transform (STFT) plane overlaid by changepoints (*black*). Subsequent panes show the spectral moments (*black*), such as: *b)* spectral centroid, *c)* spectral spread, *d)* spectral skewness, and *e)* spectral kurtosis, with the corresponding changepoints (*gray*). Note that changepoints are connected by *solid gray lines* only to ease the readability.

What we cannot assume neither in practical nor in statistical terms, that the probability structure will be time-independent during the travel. That is, variability of the vertical accelerations changes with time in the presence of surface discontinuities, by stopping the car at red-lights, etc. Therefore, the assumption of being subjected to the same vibrations, e.g. constant RMS, is against common sense and practical experiences. While RMS variations had been studied extensively in the literature, the current dissertation has presented various spectrograms also showing-up frequency modulations, hence, not only the vibration levels but also frequency structure changes. Chapter 6 argues, that RMS variations are the result of changing structure in the time-frequency domain. In fact, both are the manifestations of the dynamic system being subjected to road excitation.

Chapter 5

Calibration of segmentations

Simulation of non-stationary random vibrations has motivated Packaging vibration testing for decades. Often, an event-detection algorithm decomposes Road vehicle vibrations when analyzing the recorded series. However, also often, heuristics and subjective justifications are provided, whereby the papers are foremost concerned with validating the non-stationarity of simulated signals. If a changepoint detection is inherent to the procedure, it is recommended to calibrate the detector. The current chapter concerns the Receiver operating characteristics (ROC) of two novel algorithms and provides contextual support by Segment length distributions (SLD).

5.1 Compared detectors

5.1.1 CUSUM-type changepoint detection

The CpD approach—realized after [73]—is applied to the first four spectral moments of STFT, denoted by μ_{ij} for $i = 1, 2, 3, 4$ and $j = 1, 2, 3, \ldots, J$ seconds of the time-frequency domain. The four series of changepoints (Cp) are unified, dissecting a spectrogram at specified instances. The CpD uses the cumulative sum of differences between the sample element and the total mean, such as

$$S_{ij} = \sum_{j=1}^{J} \left(\mu_{ij} - \overline{\mu}_{ij}\right) \tag{5.1}$$

A sudden change in the direction of S_{ij} at $\hat{S}_{ij} = \max_j |S_{ij}|$ indicates a possible change in the mean tendency. At each candidate Cp, a type of bootstrapping can evaluate the significance of the test statistic. Here, a permutation loop is implemented for $r = 1, 2, \ldots, N$ rearrangements, such that $S_{ij} \to R_{ij'r}$, j not necessarily equaling j' per r. The (resampled) test-statistic $\hat{R}_{ij'r}$ is accounted at each $\mathrm{Cp_c}$. Simply put, $\tilde{p} = 0$ confidence is voted for $\hat{S}_{ij}$ before resampling, each time a counter-evidence is found, $\tilde{p}$

increases with $1/N$. Formally, the approximated p-value is

$$\tilde{p} = \frac{\#\left\{\hat{R}|\hat{R} > \hat{S}\right\}}{N}, \tag{5.2}$$

where $\#$ denotes the number of elements. If $\tilde{p}$ stays smaller than a threshold, the Cp is considered significant, and the series is bisected. Each subsection is introduced to the same procedure until no more Cp is found, a minimum segment length is reached, or exit conditions of an infinite while loop are encountered.

5.1.2 Hypothesis-based spectrogram segmentation

In the previous sections, consecutive DFT profiles of the STFT had been segmented by significant changes according to (one-sample) paired t-tests [7] or (unpaired) two-sample t-tests [6]. The STFT spectrogram was transformed here by $\log_{10}$ operation to bring the normality-assumptions closer. The paired t-test among consecutive spectrums j and $j+1$ is used in the followings, on reasons discussed in Sec. 5.1. For $\mathbf{d} = \mathbf{x} - \mathbf{y}$ paired vectors, the corresponding hypothesis can be formulated, such as:

$$\begin{cases} H_0 : \overline{\mathbf{d}} = 0; \\ H_A : \overline{\mathbf{d}} \neq 0. \end{cases} \tag{5.3}$$

The frequency axis ensures the pairing between neighbor DFT vectors. A Cp is inserted if there is enough evidence against H_0. However, inflating Type I. error is accountable in multiple hypothesis testing; thus, *post hoc* correction might compensate for the inflation.

5.1.3 Hypothesis-based spectrogram segmentation with Bonferroni correction

Family-wise error rate, α_{fw}, increases in multiple hypothesis testing, i.e., an increasing probability of at least one Type I. error is accountable. The Bonferroni correction expresses for m comparisons conducted on the same preliminary significance level, α_0, that the probability of no α error for the overall family of m tests is [109]: $\alpha_{\mathrm{fw}} = 1 - (1 - \alpha_0)^m$, where m equals the number of comparisons, i.e., the number of spectrums minus one. With *post hoc* correction, individual decisions are overruled by the new

$$\alpha_{\mathrm{B}} = \alpha_0 / m \tag{5.4}$$

Bonferroni significance limit.

5.2 Methods of comparison

It is found necessary to summarize the abbreviations for the three procedures, such as CUSUM-type changepoint detection (CpD), Hypothesis-based spectrogram segmentation (3S), and the Hypothesis-based spectrogram segmentation with Bonferroni correction (3SB). Where it is not of particular interest, which type of hypothesis-based procedure is concerned, 3S(B) notation is used.

The investigations resemble the same logic, such as the establishment of samples (5.2.1), derivations of technological windows and the choice on Points of interest (POI) (5.2.2), the Receiver operating characteristics (ROC) (5.2.3), and the Segment length distributions (SLD) (5.2.4).

5.2.1 Establishment of samples

The simulation, introduced in Chapter 6, is used to synthesize RVV. Here some key attributes are mentioned in advance. The method simulates statistically well-aligned DFT profiles per second of segments, and in each segment a different profile is chosen. The data-driven approach relies on real-world RVV; thus, it is understood as a mixture of artificial and natural RVV. Noteworthy, that changepoints (Cp) are known in advance and thus, the condition positives (CP) are also known. The first ensemble of four series (A,B,C,D) with different prevalence is subjected to CpD on the first hand. Samples are depicted in Fig. 5.1. The second ensemble consists of three series (E,F,G), prepared with high prevalence for 3S(B) procedures, see Fig. 5.2. Furthermore, each of the latter three samples is further trisected to supply similar prevalence but on different lengths, J. Also, the first ensemble is used later in Section 5.3.3, confronting CpD and 3S methods.

5.2.2 Operation surfaces and points of interests

The Eq. 5.5 expresses that a given number of permutations are necessary (at least as extreme as the un-resampled test-statistic) to consider a candidate Cp insignificant. This way, the concept of Significance reserve can be introduced.

Definition 1. *The significance reserve,* SR*, denotes the number of permutations necessary to consider a candidate changepoint non-significant in a resampling scheme when a rearrangement of* $x \to r$ *yields at least as extreme test-statistic,* $\hat{r}$ *as the un-rearranged sample,* $\hat{x}$*, for* $n = 1, 2, \ldots, N$ *resampling. The fraction of* α/N *significance portion is accumulated for* $\tilde{p} = 0$*, each time* $\hat{r} > \hat{x}$*.*

In other words, the significance reserve describes a reserve of staying significant for a candidate changepoint. While the rearrangement of elements is a matter of randomness,

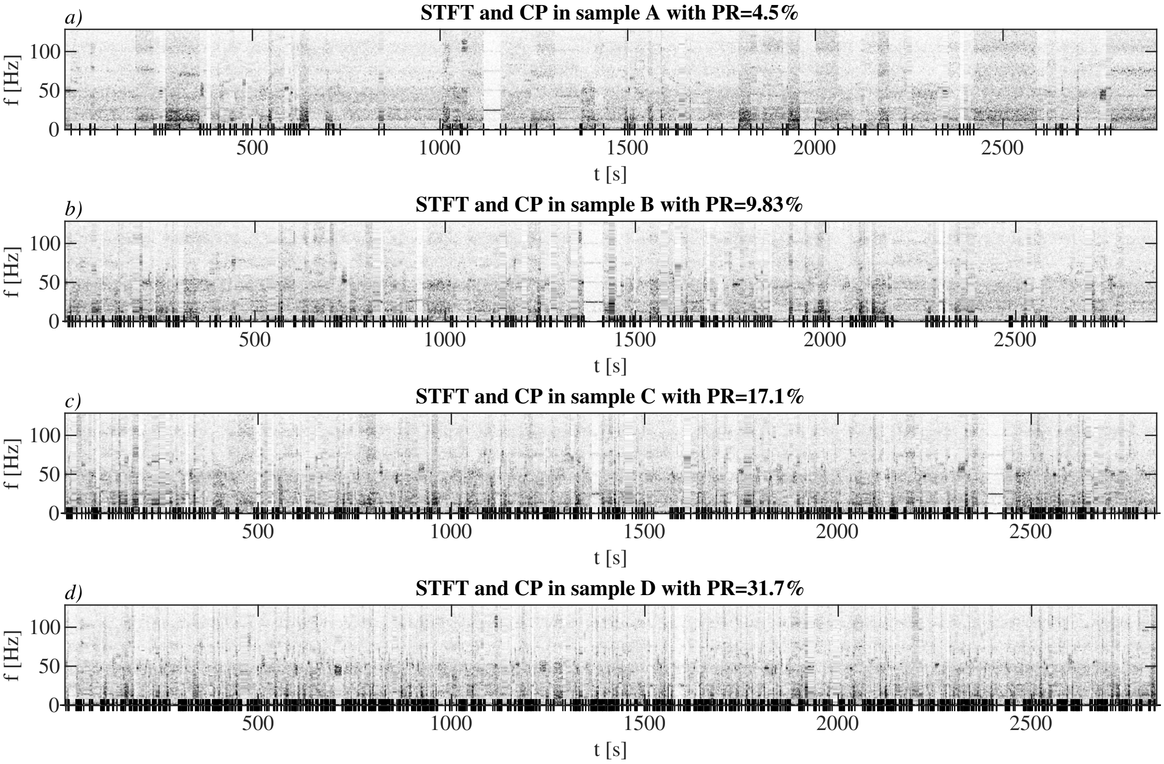

Figure 5.1: Short-time Fourier transform of the samples A,B,C,D. Changepoints, i.e., condition positives indicated by bars, | on the horizontal axes.

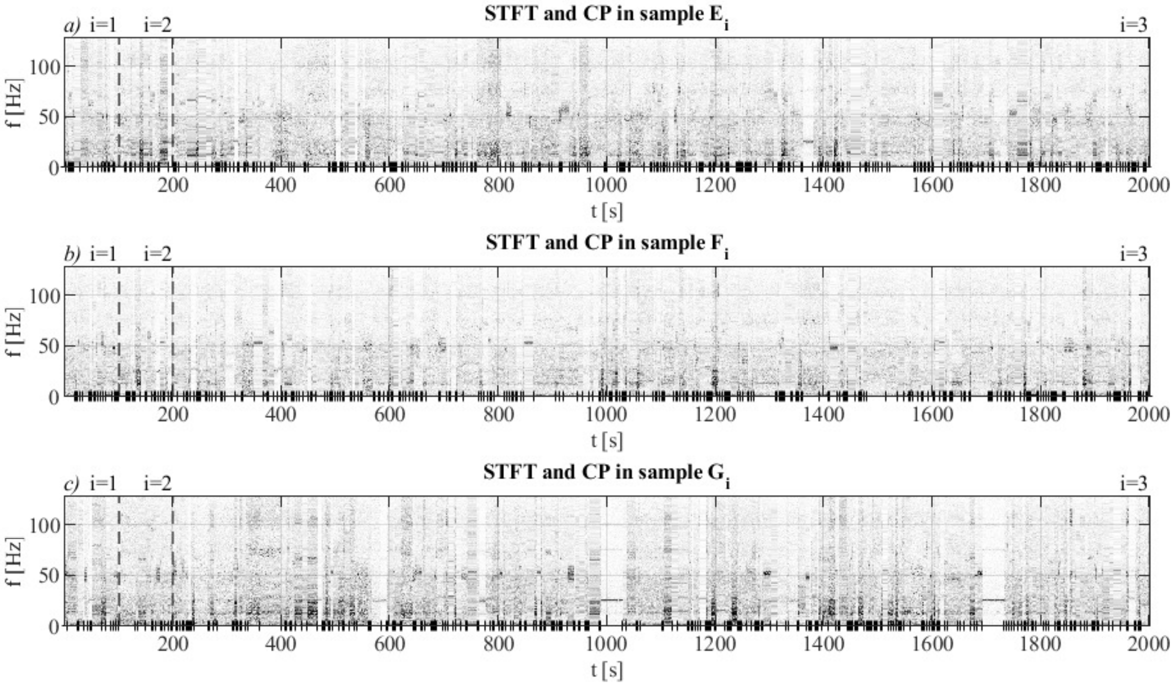

Figure 5.2: Short-time Fourier transform of the samples E,F,G.

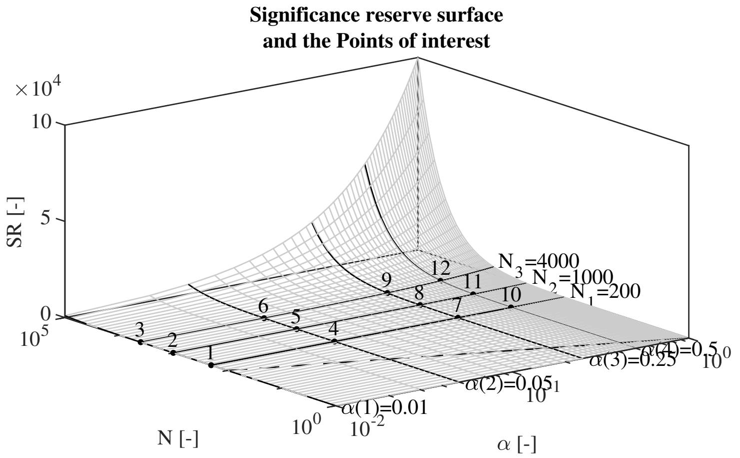

Figure 5.3: The Significance reserve surface (*gray*) with 12 points of interest in the cross-sections of iso-permutation curves $N = 200, 1000, 4000$ and iso-significance limits $\alpha = 0.01, 0.05, 0.25, 0.50$. Each point is above the minimum number of permutations (*dashed*).

the closest parameters of influence are α and N, which can be expressed as

$$\text{SRS} = \frac{\alpha}{1/N}, \tag{5.5}$$

depicting the Significance reserve surface (SRS), illustrated in Fig. 5.3. The POI avoid the lower limit of SRS = 1, also $N = 4000$ permutations constitute an upper limit due to computational practicality.

In the case of Bonferroni correction, Eq. 5.4 is illustrated in Fig. 5.4. Special considerations worth mentioning. The number of hypotheses to test is not always a matter of choice; here, the length of samples skeletonizes different scenarios. Also, few investigations are available on the number of Cp in RVV. At last, $\alpha_0 > 0.10$ significance limits are atypical, but this chapter explores the operation in large perspectives due to the novelty of 3S(B).

5.2.3 Receiver operating characteristics

Consider a population with *a priori* prevalence, PR, of an arbitrary condition. The condition may be the real presence of disease (condition positives, CP) among the healthy individuals (condition negatives, CN). In time-series analysis, e.g., shocks can be present in a random vibration signal, as in Fig. 5.5.*a)*. Let us suppose an RVV is recorded, and a particular statistic is obtained per second. Let us further suppose that we could precisely discern shocks (CP) from stationary Gaussian random vibrations (CN) possessing sufficiently good values of the statistic. Further, we aim to investigate different thresholds for the given statistic, by which, we could distinguish shocks (S) from shock-free vibrations (V) in future observations. In the same pane, a binary

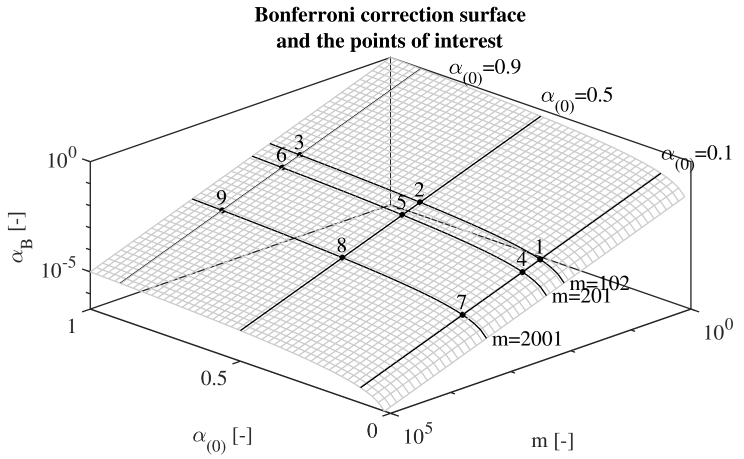

Figure 5.4: The Bonferroni correction surface (*gray*) along the nine points of interest in the cross-sections of the iso-curves corresponding to the number of hypotheses to test $m = 102, 201, 2001$ and preliminary iso-significance limits $\alpha_0 = 0.10, 0.50, 0.90$. Samples E,F,G are tested at each POI.

Table 5.1: Confusion matrix for a binary response

		Prediction		Metrics
		DP	DN	
Reality	CP	TP	FN	TPR=TP/CP; FNR=FN/CP
	CN	FP	TN	TNR=TN/CN; FPR=FP/CN

DP: positive by decision; DN: negative by decision
FNR: false negative rate; TNR: true negative rate

logistic model is fitted to 100 shock- and 100 vibration statistics data. Thus, if

$$\mathrm{PR} = \frac{\mathrm{CP}}{\mathrm{CP} + \mathrm{CN}} \tag{5.6}$$

then 50% prevalence is present in the example. Let the rhombus symbol denote our first guess of a threshold in the same plot. Then, most shocks are correctly considered positive answers above the threshold, contributing to true positives (TP). On the other hand, shocks below the threshold are incorrectly classified as vibration, and hence, false negatives (FN) are obtained.

Table 5.2: Prevalence of samples E,F,G, according to samples A,B,C per the $i = 1, 2, 3$-th sub-samples and corresponding points of interest per row for the hypothesis-based segmentation

i	**E**	**F**	**G**	POI
1	18.63%	18.63%	11.76%	1,2,3
2	14.93%	21.89%	15.42%	4,5,6
3	16.44%	17.04%	17.39%	7,8,9

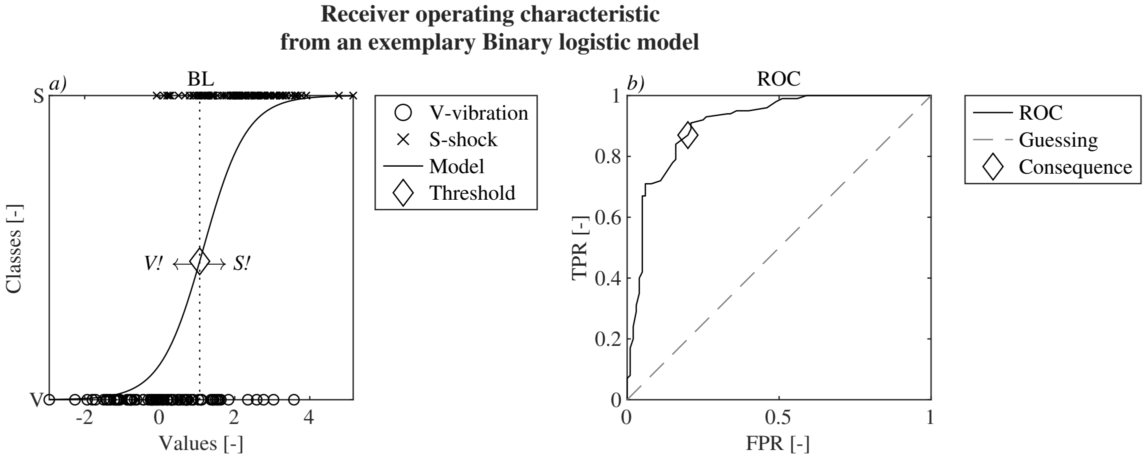

Figure 5.5: An exemplary classification task. Pane *a)* binary logistic model (BL) of vibration (V) and shock (S) events with corresponding values and an arbitrary threshold denoted by rhombus. Events with values lower than the threshold are categorized as vibration (V!); conversely, supra-threshold values are considered shocks (S!). Pane *b)* receiver operating characteristic as of thresholds, also highlighting the consequence of the initial choice. The ROC curve suggests that the BL model is comparatively better than guessing here.

Typically, the control group is investigated similarly. Vibration values below the threshold are correctly classified as vibration constituting to true negatives (TN), and vibrations above the cut-off are falsely classified as a shock, yielding false positives (FP). It is in a common interest to evaluate the true positive rate, $\mathrm{TPR} = \mathrm{TPR}(t)$ being a function of threshold, t; in other terms, the sensitivity, such that

$$\mathrm{TPR} = \mathrm{TP}/\mathrm{CP}, \tag{5.7}$$

which is "*the probability that a person will test positive for a disease, given the person actually has the disease*" [107, p.484]. It may be translated as "*the probability that a classifier will classify a pattern as a target when it really is a target*" [122, p.378]. In the low base rate problem, with rate corresponding to a condition or behavior, it can occur that tests designed to discern rare conditions can find TP, however, beneath an unexpectedly large number of FP. Thus, it is wise to measure the true negative rate, $\mathrm{TNR} = \mathrm{TNR}(t)$, namely specificity, which is "*the probability that a person will test negative for a disease, given the person actually does not have the disease*" [107], in other terms "*the probability that a classifier will correctly classify the true nontarget cases*" [122]. It is commonly expressed as $\mathrm{TNR} = \mathrm{TN}/\mathrm{CN}$, and it occurs that the false positive rate $\mathrm{FPR} = 1 - \mathrm{TNR}$, or directly

$$\mathrm{FPR} = \mathrm{FP}/\mathrm{CN}, \tag{5.8}$$

denoting the ratio of false positives among the (*truly*) condition negatives. The confusion matrix and frequent statistics are introduced in Table 5.1 on page 78. The ROC curve for the introductory examples can be seen in Fig. 5.5.*b)*.

5.2.4 Segment length distribution

The series of Cp indicate the borders of segments in the STFT at given instances denoted by "|" symbols at $f = 0$ Hz in Fig. 5.1. The Cp is considered to be simultaneously present in every frequency bin, visually as vertical lines at the "|" symbols. The horizontal distance between two Cp, namely the segment length is in the center of interest, which is investigated on count-based Segment length distributions (SLD).

5.3 Results

5.3.1 Evaluation of changepoint detection

The CpD is run on the four samples of different prevalence classes, evaluated at the 12 POI on the SRS from Fig. 5.3. The ROC statistics are here snapshots of the ROC curve in Fig. 5.6. The general observations are:

a. the prevalence has much influence at low α; with increasing PR, the effect decreases,

b. low PR tends to yield higher TPR; conversely, high PR can deliver low TPR,

c. the number of permutations produced minor differences at iso-significance settings; see rows of Fig. 5.6.

d. it is hard to approach FPR regions of 50%; see last row of Fig. 5.6.

Segment length distributions in Fig. 5.7 directly show the number of segments, #, in the bins. It supports that

e. the number of resampling, N, produced few differences in the obtained distribution.

Thus, further investigations concentrate on PR and α. It is deduced, that:

f. false positives contribute to over-segmentation, and

g. false negatives contribute to under-segmentation.

Furthermore, Fig. 5.7 suggests that

h. there exist an α threshold for each PR, minimizing the erroneous statistical inferences.

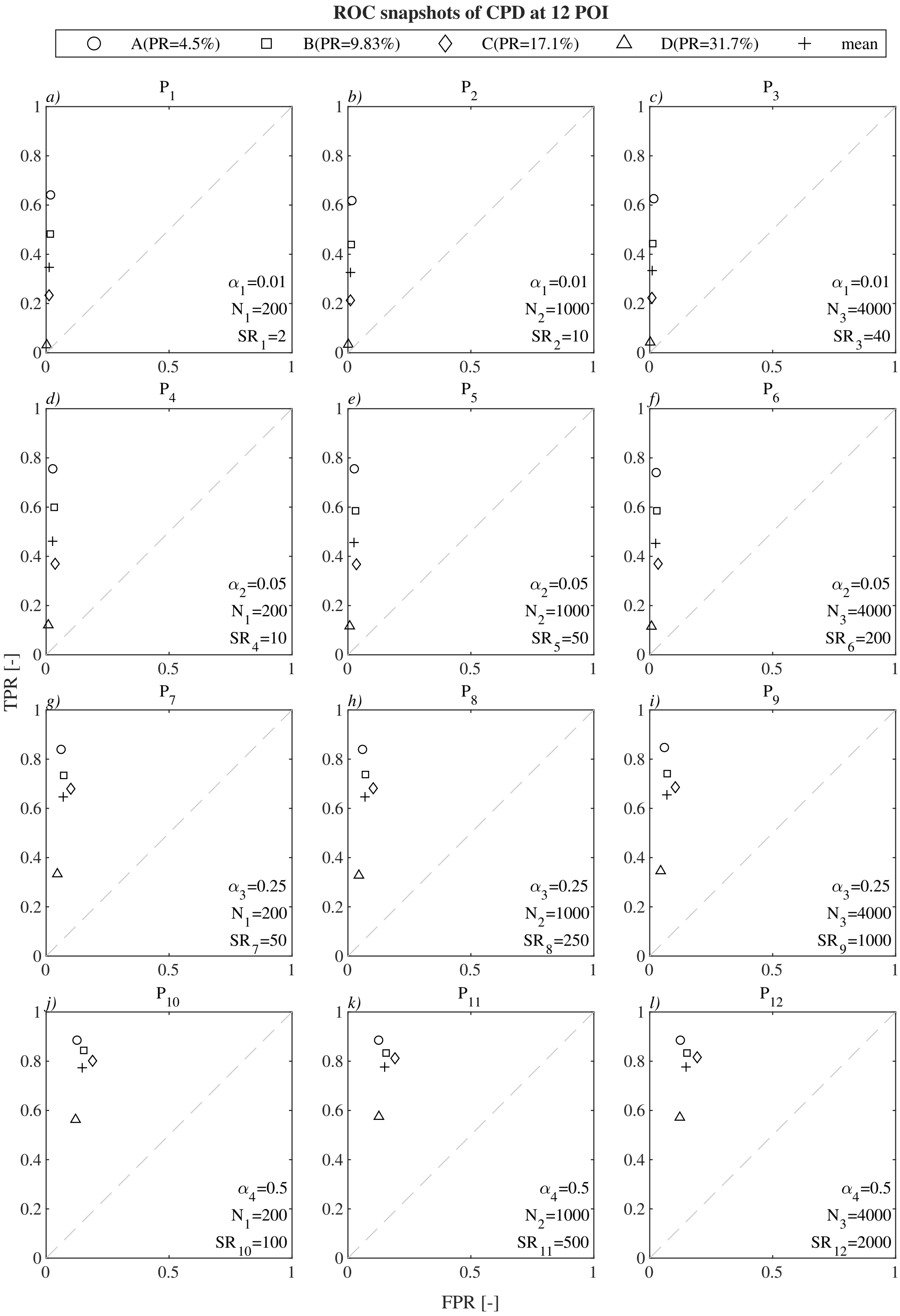

Figure 5.6: ROC snapshots of the CUSUM-type changepoint detection (CpD) on four different samples with different prevalence according to *symbols* at 12 POI according to *panes*. Rows of panes correspond to iso-significance limits, α; columns of panes relate to iso-permutations, N. Note that the significance reserve, SR, varies per POI.

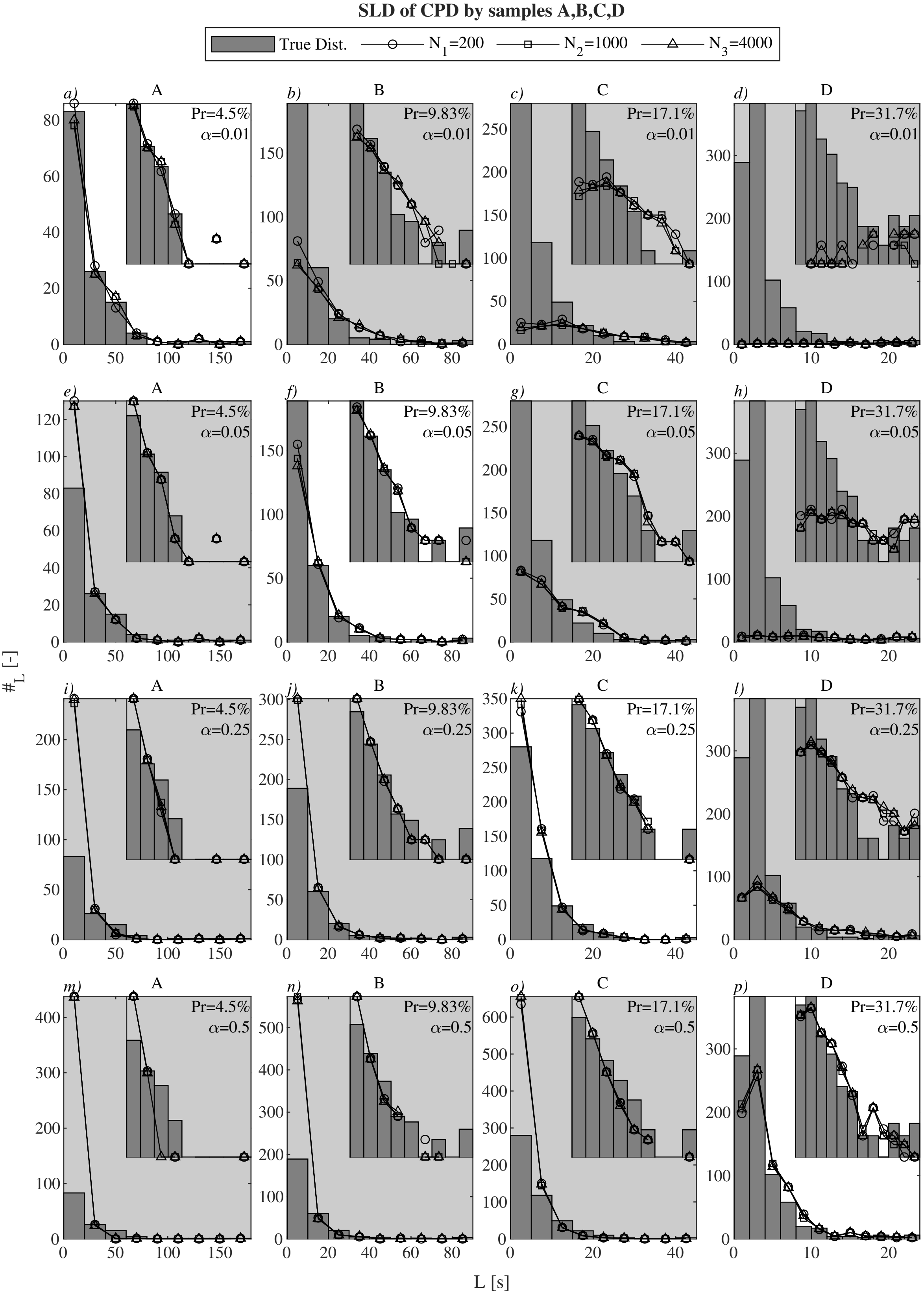

Figure 5.7: Segment length count-distributions from the CUSUM-type changepoint detection (CpD) on four samples. Bars denote the true distributions; lines correspond to the number of permutations. Panes correspond to different samples, each tested on iso-significance limits at different permutations. Note how different permutations yielded overlapping lines.

5.3.2 Evaluation of hypothesis-based segmentation

The 3S(B) is applied to the three samples E,F,G aimed to possess a similar prevalence of $\sim 17\%$. Each sample are divided into sub-series $i = 1, 2, 3$ of length $\sim 100, 200, 2000$ sec corresponds to nine POI. The subdivision changed the sample-wise PR, as expected, which are summarized in Table 5.2 with corresponding POI in Fig. 5.4. Also, Fig. 5.8 shows the 3S method without correction (*black*) and with *post hoc* correction (*gray*). Similarly, the ROC snapshots of 3S(B) allow the following observations according to Fig. 5.8:

a. low α_0 yielded low FPR and medium to high TPR,

b. medium α_0 yielded medium FPR and high TPR,

c. high α_0 yielded high FPR and high TPR,

which is a good justification of the expected ROC. Regarding sample sizes,

d. the longer the sample, the more rigorous the TPR & FPR estimations are.

With *post hoc* set up on Fig. 5.8 (*gray symbols*),

e. minimal FPR is registered, the mean TPR being dispersed around 0.5.

Fig. 5.9 compares the count based SLD after 3S, each pane illustrating a given sub-sample with three different preliminary significance limits. It is concluded that:

f. high thresholds are likely to yield over-segmentation, low α is the best guess in general, given the current ensemble,

which success must be accredited to the paired t-test. Results of 3SB in the probability domain are omitted from here; further explanations are given in the Discussion. The following subsection directly collides CpD and 3S.

5.3.3 Competing comparisons

So far, the behavior of CpD, 3S, and 3SB has been explored, but a direct comparison could not be conducted without the above observations. The following experiences are echoed here:

- the hereby concerned CpD realization does not necessarily require immense iterations per candidate Cp,
- the sample length is indifferent to significance limits in CpD and 3S—not so in 3SB,

- Bonferroni correction may be overlooked, and directly 3S results can also be helpful,
- short recordings with high PR were necessary for 3S for demonstration purposes. (Note that the long sample-low prevalence setting operation could not be shown.)

Thus, CpD and 3S are rerun on samples A,B,C,D with $N = 100$ replications in case of CpD; and without *post hoc* correction of 3S. In both cases, mutual significance levels are applied[1]. The ROC characteristics are displayed in Fig. 5.10 by the four different PR classes. Therein, pane *a)* confirms that an increase in PR can flatten the ROC curve of CpD. Remarkably, CpD can hardly pass the FPR = 0.50 limit with increasing α, which must be accredited to the exit conditions. However, pane *b)* depicts 3S as being quasi prevalence-independent, which could not reach below TPR = 0.50 in current samples. However, this satisfactory performance is not a general conclusion, as Fig. 5.8.*a) black rhombus* instantly falsifies that.

5.4 Discussion

In brief, it was aimed to find all real changepoints, Cp, as true positives, TP; beneath not-being oversensitive, i.e., with consistency on TN. It is shown that FP often corrupts these aims leading to over-segmentation. When numerous false alarms occur, the obtained distribution can overestimate short segments and underestimate long segments. In contrary terms, the modest sensitivity can increase FN, which kind of over-look of real changes can result in under-segmentation; thus, SLD might be under-represented in lower bins and over-estimated in larger bins.

5.4.1 Arguments on detection methods

The number of resampling applied to the given samples did not yield dramatically different results, suggesting that CpD can be robust enough also at a moderate number of permutations. However, the analyst is advised that the recursion can suffer a severe failure when a FN is incurred in one of the first p-value approximations. Then, simply due to randomness, a prominent changepoint is left out, the loop exits and a dramatic under-segmentation is obtained.

Let us suppose that the prevalence is precisely 50%, i.e., every 2-nd sec. is different from neighboring ones. Then, in the hypothetical spectrogram of $[\mathbf{a}, \mathbf{b}, \mathbf{a}, \mathbf{b}, \mathbf{a}, \dots]$, with DFT vectors sufficiently different $\mathbf{a}$ and $\mathbf{b}$, the CpD may encounter that the absolute of CUSUM of a spectral moment does not have a maximum. Above 50% prevalence, however, one must consider, either (a) transients are occasionally present in

---

[1] $\alpha = \{0.01, 0.05, 0.10, 0.20, 0.30, 0.40, 0.50, 0.60, 0.70, 0.80, 0.90, 0.99\}$

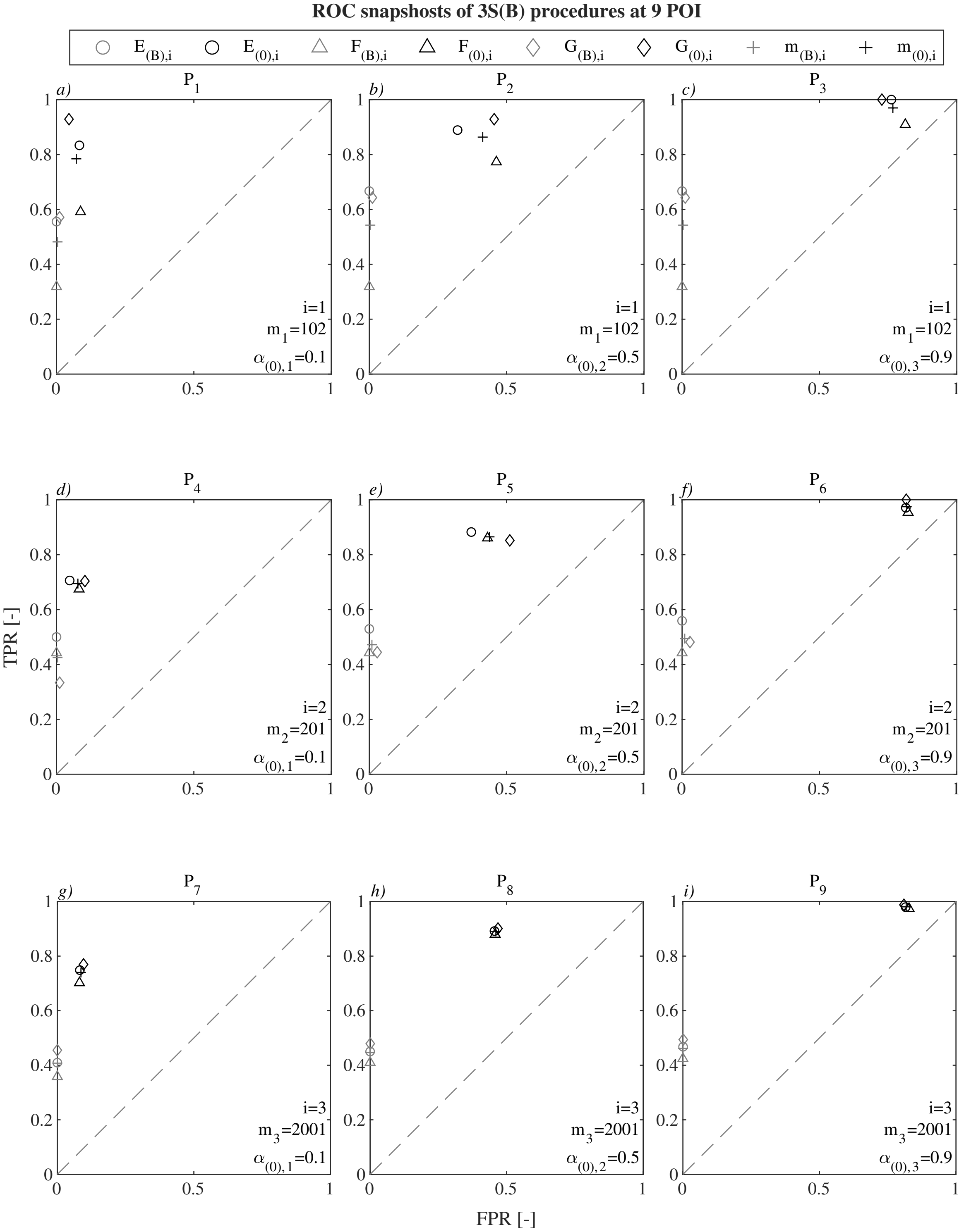

Figure 5.8: ROC snapshots of Hypothesis-based segmentation without Bonferroni correction (3S) denoted by *black symbols* and (0) subscripts; and 3S with Bonferroni correction (3SB) denoted by *gray symbols* and (B) subscripts on three different samples (E,F,G) at 9 POI. Rows of panes correspond to iso-significance limits, α; columns of panes relate to number of spectrums to test.

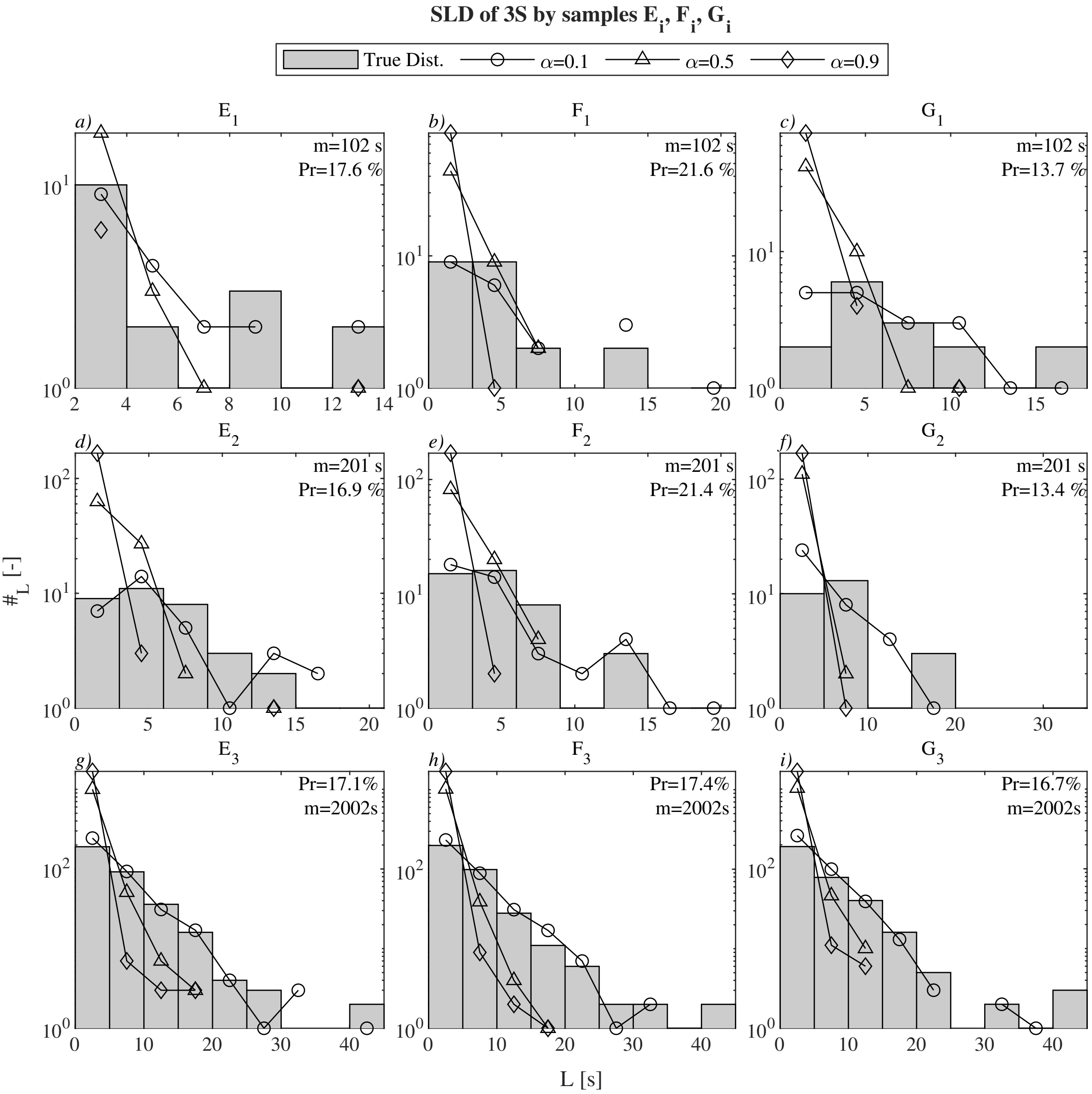

Figure 5.9: Segment length count-distributions from the Hypothesis-based segmentation (3S) on nine sub-samples. Bars denote the true distributions; *lines* correspond to preliminary significance limits. Columns of panes correspond to primary samples (E,F,G), and rows of panes relate to the i-th fraction of main samples $\mathrm{E}_i, \mathrm{F}_i, \mathrm{G}_i$.

an underlying slowly varying process, or (b) mainly successive transients describe the process. While (a) is more straightforward to imagine under everyday circumstances, such as traveling on roads and occasionally meeting some potholes, setting (b) can arise from driving on off-road tracks, for example. It is expected that 3S can overcome such limitations incurred in RVV during the latter case (b).

3S(B) methods rely on the one-sample t-test here, which omits a data-driven resampling, thus, can be performed under every prevalence scenario. It shall be appreciated that the one-sample t-test derives its test-statistic still from two samples: precisely, the differences of two paired samples. Therefore, the differences of two DFT profiles along the whole bandwidth of the spectrum contribute to the estimation. The two-sample (or unpaired) t-test accounts for the two samples differently. Let the following minimum-example use DFT vectors of $\mathbf{a} = [1, 1, 2]$ and $\mathbf{b} = [2, 1, 1]$ ordered as of $[f_1, f_2, f_3]$ frequency components, depicting a frequency modulation from $\mathbf{a}$ to $\mathbf{b}$. It is apparent that the vectors $\mathbf{a}$ & $\mathbf{b}$ are the "*same*" for the two-sample t-test, which does not take the sequence—hence such a frequency modulation—into account. Instead, the two-sample t-test is better to examine overall magnitude modulations by the scenario of, e.g., increasing background noise such as from $\mathbf{a} = [1, 1, 2]$ to $\mathbf{b} = [1, 2, 2]$.

Despite the Bonferroni correction being a mature method, contributing to a whole branch of statistics, its application remained more-or-less chaotic as pointed out, e.g., in the ophthalmic discipline [123]. Some thoughts of ibid. will be borrowed here and put into the current context. Foremost to highlight here the subtle narrative, the use of Bonferroni correction sometimes depends on the intentions—though not the wishes of the analyst. For example, if it is aimed to assess a universal null hypothesis that all tests are non-significant, i.e., there is no change (at all) in the RVV, then Bonferroni correction can improve the reliance of the general H_0. Similarly, if it is imperative to avoid a Type I. error, that is, important costs can be attributed to inserting a changepoint, then applying the *post hoc* correction can also be imperative. But as shown in Fig. 5.8, CP can be left out, as well. Conversely, no correction had been suggested in exploratory studies concerning the search for any significant difference; or if the individual tests' results are important. The numerical investigations presented in Fig. 5.8. also clearly support, that "*reducing the chance of a Type I. error, but at the expense of a Type II. error*" (ibid.). Seemingly, the Bonferroni correction does mitigate Type I. errors but at consequences of increasing false negatives; hence, it cannot provide SLD reasonably well-aligned. Still, the *post hoc* test may be beneficially implemented in general-null testing.

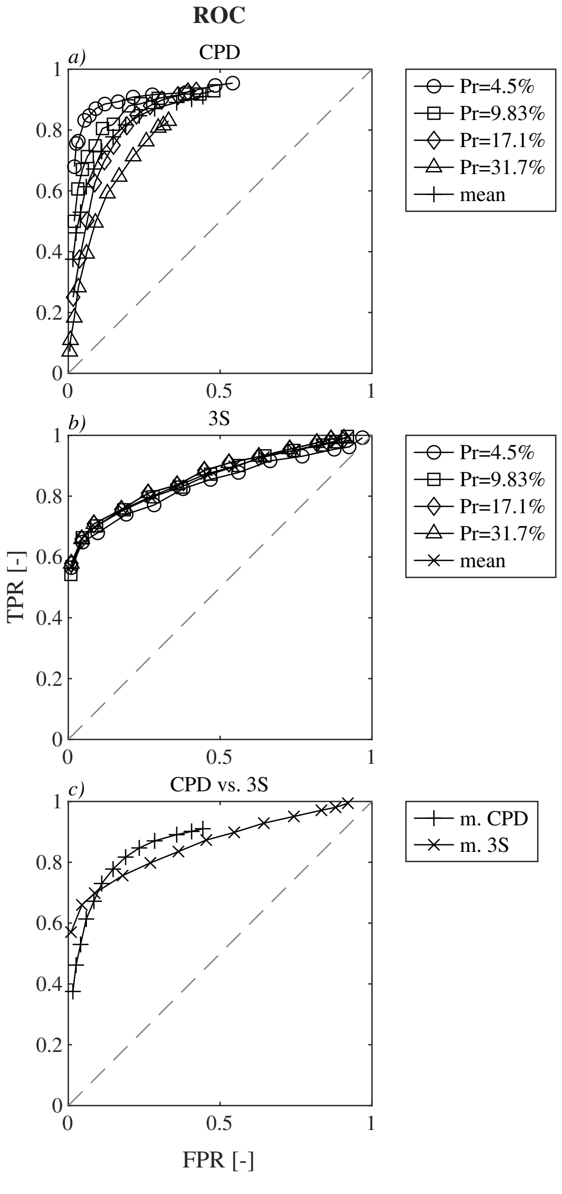

Figure 5.10: Comparison of CUSUM- and Hypothesis-based segmentation by Receiver operating characteristics (ROC) on four samples of (A,B,C,D) with different prevalence (PR). Pane *a)* indicates ROC of CpD and the mean of statistics (+); pane *b)* shows ROC of 3D for the same samples, mean statistics denoted by ×. Finally, pane *c)* repeats the mean of ROC statistics overlaid.

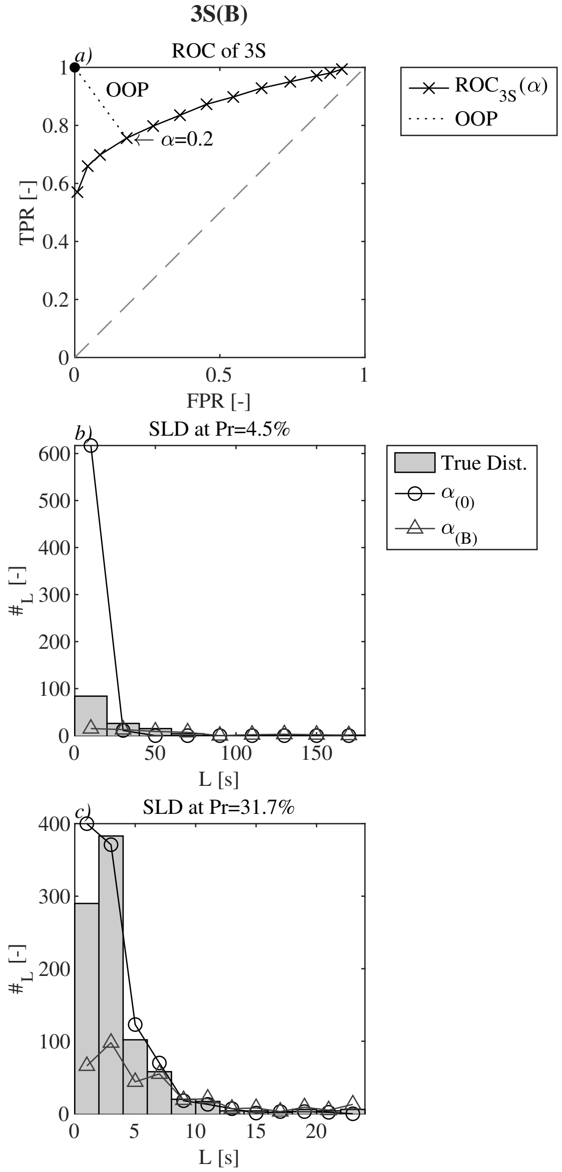

Figure 5.11: Comparison of segment length distributions by hypothesis-based segmentation without- and with Bonferroni correction, 3S (*circles*) and 3SB (*triangles*) respectively. Pane *a)* illustrates the derived optimal operating point (OOP) closest to $[0, 1]$ coordinate from Fig. 5.10.*c)* by *crosses*, yielding $\alpha = 0.10$. Pane *b)* shows the true distribution with bars and corresponding SLD from 3S and 3SB at optimal α for the low- prevalence sample, A; and pane *c)* similarly for the high-prevalence sample, D. Note, that OOP is derived from ROC of 3S, whereby an OOP of 3SB is not applicable according to Fig. 5.10.

5.4.2 On the receiver operating characteristics

ROC curves are mainly used on two occasions: comparing classifiers and deriving a classifiers' optimal operating point (OOP). Numerous proposals have been made so far on OOP [124], also an OOP shall be justified in the given context. The interested reader is referred to [125] for examples of justifications. The simple "*closest to* $[0, 1]$ *criteria*" is presented here, referring to the point closest to the top-left corner on the ROC plot. Formally, $d_{\mathrm{E}} = \left[(\mathrm{FPR}^2 + (1 - \mathrm{TPR})^2\right]^{0.5}$ denotes the Euclidean distances between the ROC curve and the $[0, 1]$ coordinate. It is found in Fig. 5.10.*a)* that the point of (0.09,0.72) relates to the minimum d_E corresponding to $\alpha = 0.10$ significance limit in 3S—according to the given rudimentary curve. The corresponding SLD suggest, that a low prevalence sample on pane *b*) could not be adequately modeled. However, high prevalence sample on pane *c)* depicts the reasonable well-alignment of 3S; also, the over-conservatism of the Bonferroni correction is presented in either case, *b-c).*

5.5 Conclusion

3S(B) and CpD rely on established methods. 3S(B) are comparatively faster than CpD. 3S(B) are easier to implement. If CpD exits suspiciously early, it contributes to under-segmentation. 3S can be run on the contrary. The Bonferroni correction again proved to be too conservative. Current challenge points toward the estimation of prevalence. In a low base rate problem, CpD is suggested, and can be suited for high PR classes. High prevalence samples can be beneficially analyzed also by 3S if resampling schemes are not favorable. It is generally advised to strive for the robustness analysis of detectors in changepoint detection methods.

Thesis 4. I have shown that there exists a significance level and it can be determined for so-called *CUSUM* recursive algorithms—which algorithm searches for the local extrema of the cumulative sum of deviations from the total mean—which significance level minimizes the difference between the theoretical distribution of the segment lengths of the test signal and the segment length distribution between the detected boundary points. ■ *Ref.*: [8, 9]

Chapter 6

Simulation

This is the last before one technical chapter with new concepts, thus, it is found reasonable to reiterate on all necessary steps toward current final application, the numerical simulation of spectrally non-stationary RVV. In fact, the next chapter will investigate future following segmentation.

Vibration testing procedures relying solely on a Fourier profile can introduce only stationary random vibrations. It is in contrast with the non-stationary and non-Gaussian nature of the Road vehicle vibrations (RVV). The following procedure segments the first four spectral moments of the time–frequency domain of RVV, constructs probability density arrays per frequency bins, and perform simulations according to random segment lengths and -root mean squares, yielding more realistic representations of RVV. The distribution of time- and frequency domain moments and normalized spectral entropies are confronted. The Probability-based spectrogram synthesis (PBSS) offers a data-driven stochastic modeling framework for simulating non-stationary RVV.

6.1 Introduction

A Power spectral density (PSD) profile, joint with a uniformly distributed random phase series, can only contribute to stationary Gaussian vibrations by inverse Fourier transformation. Widely accepted that an ideal simulation shall introduce varying RMS levels, transients, and harmonic excitation as the constituents of Road vehicle vibration (RVV). The Packaging vibration testing (PVT) community lined up different algorithms to break down RVV into its constituents. Unfortunately, also purposeful decompositions are inherently suggested. Then, a superposition or concatenation of simulated segments concludes a simulation.

As consensus on decomposition is pending, the current study presents that σ-modulation, transients and harmonics can be simultaneously addressed directly in the Time–frequency domain (TFD). Moreover, the modulations in the Short-time Fourier transform (STFT) plane readily depict any constituent, reducing the need for heuristics and *a priori* assumptions. Furthermore, the multi-level probabilistic environment assures that synthetic TFD are non-stationary; consequently, varying Time domain (TD) characteristics are obtained.

Section 6.3 describes three RVV measurements and the simulation routine. Sec. 6.4 presents that arbitrary number of different STFT can be simulated from one measurement; also, a second run illustrates that the pooled sampling of numerous STFTs produces enhanced simulations. It is followed by verification of synthetic signals' non-Gaussian and non-stationary nature. Finally, Sec. 6.5 shows modeling of segment length and -RMS distributions obtained by the segmentation of spectral moments.

6.2 Related works

Although, Time-history replication (THR) is a straightforward approach for non-stationary RVV testing, it cannot be considered a simulation due to the lack of representative manner on an ensemble of journeys [126]. Kurtosion® [127, 128] or the distortion of waveforms via Zero-memory nonlinear (ZMNL) monotonic functions [129] achieves different-from-normal distributions, but synthesized vibrations remain statistically time-invariant [38]. The Two-way-, Three-way- and subsequently Probability split spectra provide a few spectrums by allocating sub-recordings into groups of vibration levels, groups being characterized by average PSD profiles [130, 131]; still, stationarity for prolonged sub-periods is apparent in time domain.

Changepoint detection (CPD) gained increasing emphasis to segment recordings [5]. A Bayesian approach is implemented on a series of International roughness indices [90], but the study did not address simulations. The moving mean square drop-off distance and crest factor separate quasi constant RMS segments and transients in road elevation profiles [85]. Simulations can be conducted by superimposing transients on a series of σ-modulated Gaussian components. The general approach of moving statistics is prone to the window length and threshold value subjectivity. The Random Gaussian sequence decomposition utilized a CUSUM scheme on the analytic signal obtained by Hilbert transform to find stationary sections within the vibration series [98, 132]. The simulative modulation functions do not necessarily resemble TFD characteristics.

The Short-time Fourier transform (STFT) plane of RVV is segmented in multiple comparison procedures using paired t-tests [7] and two-sample t-tests [6] between consecutive DFT vectors. While *post hoc* procedures are often advised in multiple comparisons, the sensitivity and specificity are affected by the *post hoc* procedures, which already have been investigated in Chapter 5.

Quarter vehicle models subjected to longitudinal pavement profiles simulate also varying traveling speeds and different parameters of vehicle models [48]. Alternatively, Frequency response functions (FRF) can be used in conjunction with road elevation PSD

[133]. However, the experimental estimation of vehicle FRF can be contra-implicated by cost-efficiency; otherwise, it may remain too generic.

The applicability of the Discrete- (DWT) and Continuous wavelet transforms (CWT) is presented on artificially introduced transients [100]. Low-pass filtering separates rigid-body motions and structural vibrations of rail-car vibration PSD, supporting shock-on-random simulations [101]. The fundamental assumption that transients occupy different bandwidths from the one comprising rigid-body motion would need thorough testing on the road vehicle vibrations instead of railed vehicle vibrations. Intrinsic mode functions (IMF) have been proposed for studying frequency-type non-stationarities [102]. The inherent subjectivity of the number of IMFs separating low- and high-frequency components persists.

Wavelet-based Gaussian decomposition presents that CWT regions of the RVV not surpassing the CWT of a Gaussian equivalent can be considered a Gaussian segment [103, 104]. The RVV is decomposed iteratively, but the first Gaussian equivalent may be biased by transients contributing to wider segment borders. The Shock extraction method provides segmentation according to the moving crest factor joint with one-tenth peak value considerations [87]. Segments are simulated as Gaussian equivalents and concatenated into a series, the last part comprising each shock. Components could be rearranged to counteract the fatigue life's unrealistic representation [89, p.365]; still, the segmentation's rigorousness is mainly challenged by the sensitivity of moving statistics.

The Hilbert amplitude spectrum is segmented per frequency bin through time using a CUSUM scheme [105]. Amplitudes in each segment of every frequency bin are fitted with various distributions. A frequency bin throughout its segments is characterized by one distribution model of amplitudes with the lowest Kullback–Leibler divergence. While changepoints can be found in each frequency bin, those do not necessarily align in time. While it allows remarkable simulations, replacing segments was presumably out of scope and, thus, it does not necessarily serve PVT applications. The authors further improved the method later. The Hilbert spectrum simulation was achieved by the former process [105], while the phase function has been modeled as the composition of a time-related part and an autonomous, random component [134].

The Karhunen–Loève expansion and translation process theory can model non-Gaussian and non-stationary random processes [135]. By iterating directly on the non-stationary auto-correlation function, the technique enhances the ITAM—an existing family of procedures, the Iterative translation approximation method. Also, the combination of the Karhunen–Loève expansion with the Linear-moments-based Hermite polynomial model is implemented [136]. The Inverse system method applied in the time domain controls time–frequency domain characteristics, demonstrating the numerical example of a cantilevered beam and a bi-axial vibration test [137].

Machine learning classifiers are also used for transient event detection, using different branches of predictors from various domains simultaneously, presenting an excessive contribution to understanding transient detection in RVV [50].

6.3 Measurements and Methods

Three RVV series have been recorded, denoted as $\mathbf{x}_n$ for $n = 1, 2, 3$. The chauffeur and its companion (app. 150 kg in total) traveled in a passenger car (Suzuki Swift Sedan 1.3 GLX–2002) on public roads of middle Hungary. The DC MEMS-type accelerometer (Recovib® Tiny 15G, effective bandwidth 250 Hz) recorded the vertical vibration at a sampling frequency of 1024 Hz, having different locations: in the coin toss behind the handbrake ($\mathbf{x}_1$), on the cockpit righthand-side ($\mathbf{x}_2$) and on a chassis element of the trunk righthand-side ($\mathbf{x}_3$). Traveled distances covered respectively 50.7, 31.1, 29.2 km. High-pass filtering of $\mathbf{x}_n$ with a cut-off frequency at 1 Hz is applied as pre-processing to eliminate the substantial DC contribution. The down-sampling by a factor of four followed, further easing the computations.

The method is collocated by two *columns* (I,II) with *steps* (1,2,...), as illustrated in Fig. 6.1. The Column I. establishes the categorization system to store RVV segments found by CpD. Column II. produces spectrally non-stationary random vibration signals. The current procedure is presented in two runs: the 1st run consisting simulations $\mathbf{y}_u$ for $u = 1, 2, 3$ from the first measured RVV, $\mathbf{x}_1$; and the 2nd run comprises the $\mathbf{y}_4$ simulation from $\mathbf{x}_n$, $n = 1, 2, 3$ measurements. Indeed, it would be sufficient to present a few simulations from multiple RVV series for presentation purposes, but field recordings are typically not widespread; thus, analysts having one measurement can also investigate the method's capability.

6.3.1 Column I. Establishment of a database

Step I.1. Let $x_n i$ denote the measured signal corresponding to $i_n = 1, 2, \ldots, T_n$ uniformly sampled instances of the $n = 1, 2, \ldots, N$ measured RVV.

Step I.2. The short-time Fourier transform $\mathbf{X}_n$ computed here uses one-second-long windows without overlapping, resulting in one Hz resolution.

Step I.3. The first four spectral moments of $\mathbf{X}_n$, respectively $\mu_m^{(n)}$ for $m = 1, 2, 3, 4$ are subjected to a CUSUM-type CpD, consisting of the following sub-steps.

Step I.3.a. Let X_{njk} denote the DFT profile corresponding to k frequency bins of the j-th second from the n-th measurement. For conciseness in Eq. 1–4, also let us

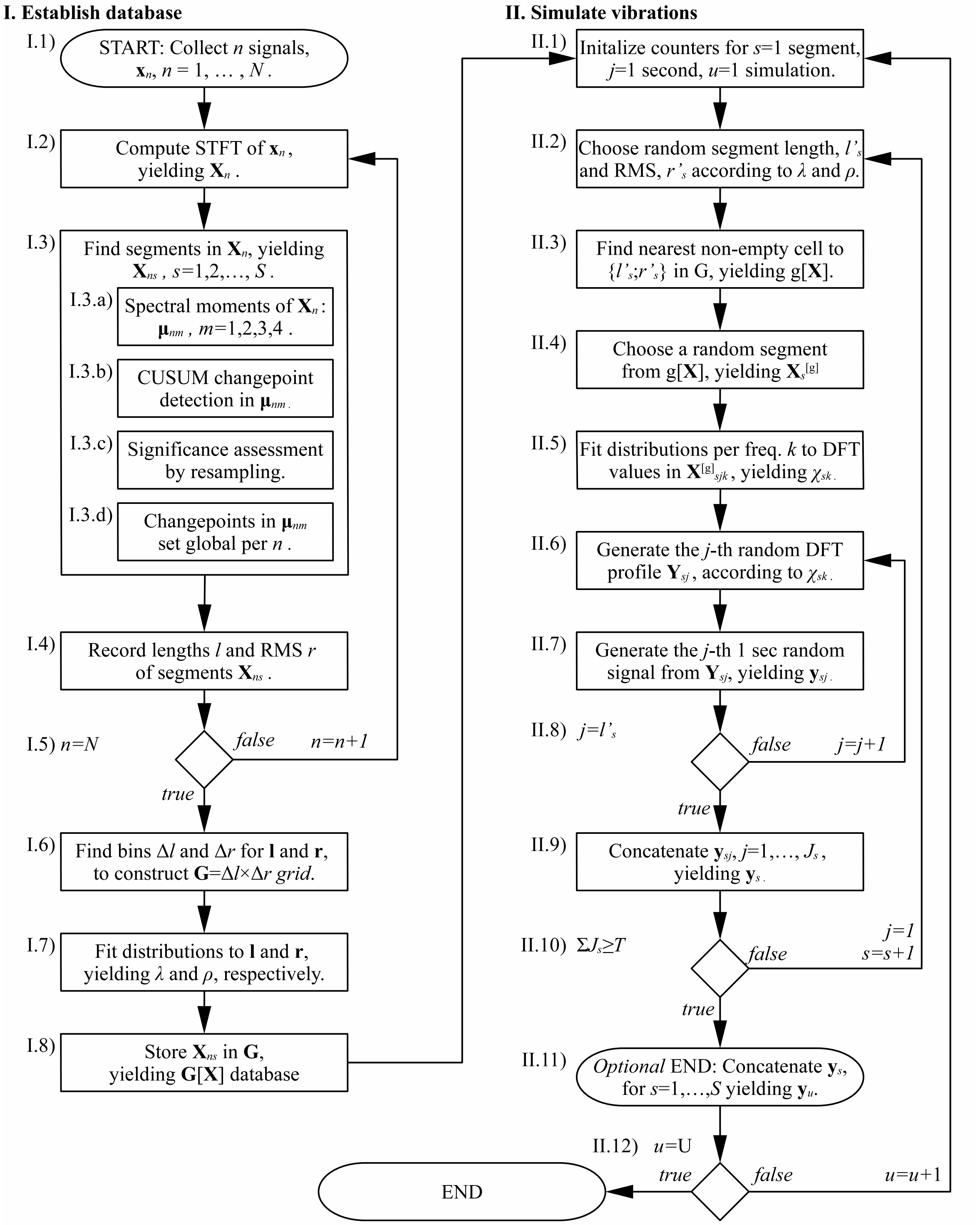

Figure 6.1: Process flowchart of Probability-based Spectrogram Synthesis (PBSS). Only sub-indices are highlighted in the current caption, such as n-th measurement, s-th segment, i-th time instance, j-th second, k-th frequency bin, and u-th simulation.

overlook n, j indices, such as $X_k = X_{njk}$ and $\mu_{mk}^{(n)} = \mu_{mk}$. The spectral centroid,

$$\mu_{1,k} = \frac{\sum_{k=1}^{K} f_k X_k}{\sum_{k=1}^{K} X_k} \tag{6.1}$$

is the frequency-weighted sum of $\mathbf{X}_n$ normalized by the unweighted sum, where f_k is the k-th frequency bin in Hz for the corresponding DFT vector $\mathbf{X}$ [77]. The spectral spread,

$$\mu_{2,k} = \sqrt{\frac{\sum_{k=1}^{K} (f_k - \mu_{1,k})^2 X_k}{\sum_{k=1}^{K} X_k}} \tag{6.2}$$

is defined as the standard deviation around the spectral centroid, which stands for the spectrum's instantaneous bandwidth [77]. The spectral skewness,

$$\mu_{3,k} = \frac{\sum_{k=1}^{K} (f_k - \mu_{1,k})^3 X_k}{\mu_{2,k}^3 \sum_{k=1}^{K} X_k} \tag{6.3}$$

describes symmetry around the centroid. The spectral kurtosis,

$$\mu_{4,k} = \frac{\sum_{k=1}^{K} (f_k - \mu_{1,k})^4 X_k}{\mu_{2,k}^4 \sum_{k=1}^{K} X_k} \tag{6.4}$$

indicates peakiness and the non-Gaussian nature.

Step I.3.b. The four spectral moments are subjected to the CUSUM-type CpD. The CUSUM abbreviation corresponds to the cumulated sum of the differences between the vector elements and the vector's mean, $S_j = \sum_{j=1}^{J} (\mu_j - \overline{\mu_j})$. An extremum $\hat{S}$ serves as a test statistic, on the other hand, it points to a candidate changepoint at the j-th second showing a sudden change in $\mathbf{S}$. The following sub-step decides upon the significance of a candidate changepoint.

Step I.3.c. From available resampling methods [79], a permutation approach is implemented here. Let $\mathbf{R}_r$ denote the r-th random rearrangement (without replacement) of elements in $\mathbf{S}$. Each time, $\hat{R} > \hat{S}$, the significance of the candidate changepoint decreases. Let the p-value be approximated by

$$\widetilde{p} = \frac{\mathrm{Num}\left[\hat{R} | \hat{R} > \hat{S}\right]}{R}, \tag{6.5}$$

with $Num\,[\cdot]$ denoting the number of elements. Each reference set consists of $r = 1, 2, \ldots, 10^4$ permutations beneath and an $\alpha = 0.05$ significance level is applied. If $\widetilde{p} < \alpha$, the candidate changepoint is considered significant.

Step I.3.d. The four series of CPs corresponding to $m = 1, 2, 3, 4$ are considered global dissections in a spectrogram $\mathbf{X}_{ns}$ and conversely, in the time domain, $\mathbf{x}_{ns}$.

Step I.4. Lengths and RMS of segments are stored in $\mathbf{l}$ and $\mathbf{r}$, respectively.

Step I.5. STFT and corresponding spectral moment calculation, followed by changepoint detection are repeated on each measurement until no more time series need to be analyzed.

Step I.6. The joint probability space $L \times R$, for $l \in L, r \in R$ is discretized into $\Delta\mathbf{l} \times \Delta\mathbf{r}$, referred to as the *grid*, $\mathbf{G}$.

Step I.7. The probability density functions λ and ρ are obtained, respectively for $\mathbf{l}$ and $\mathbf{r}$, providing probability-based choices on what RMS content to simulate and how long. The grid and PDFs from the 1st run are illustrated in Fig. 6.2.

Step I.8. The allocation of segments $\mathbf{X}_n s$ to the cells of $\mathbf{G}$ is denoted as $\mathbf{G}\left[\mathbf{X}\right]$, Practically, each STFT segment can be labeled such as $\mathbf{X}_{ns}^{[\mathbf{G}]}$, referred to as the database interpreted on the grid.

In summary, the procedure's I. column introduces a number of measurements to changepoint detection. Changepoints provide borders of segments to measure the segment's length and -RMS. Labeling segments as per the corresponding location in the discretized joint probability space constitutes the *database* of a run.

6.3.2 Column II. Vibration simulations

Random Gaussian vibrations are simulated per seconds in the randomly chosen segment. Finally, segments are concatenated to a total simulation signal in TFD and TD.

Step II.1. The process begins with initializing loop counters for the s-th simulated segment, containing j seconds in the u-th simulation.

Step II.2. One random realization pair $\{l'_s, r'_s\}$ is drawn from $\lambda \times \rho$ corresponding to one point in the grid. If the random coordinate pair arrives at a non-empty tile, the nearest non-empty cell is looked for.

Step II.3. The nearest non-empty cell, $g \in \mathbf{G}$, is found by the Euclidean distance between cell centers. It is noted that a non-empty cell is closest to itself.

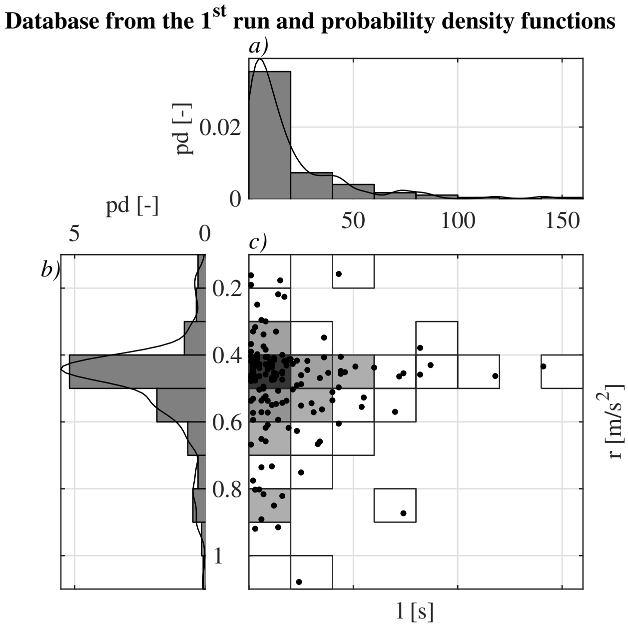

Figure 6.2: The 1st run database. Pane *a)* marginal probability density pd($\mathbf{l}$) with corresponding histogram; pane *b)* marginal probability density pd($\mathbf{r}$); pane *c)* discretized joint probability space of segment lengths $\mathbf{l}$ and RMS, $\mathbf{r}$, where gray-scale squares indicate joint probability densities overlayed by $\{\mathbf{l}, \mathbf{r}\}$ scatter.

Table 6.1: Distributions fitted to DFT values. DFT values $\mathbf{X}_{sjk}$ in the s-th segment per frequency bin k are fitted differently as of the segment length j.

j	**Fit**
1	Direct replication, $\mathbf{Y} = \mathbf{X}$
2–9	Uniform distribution
10–19	Normal distribution
>19	One of the trial distributions*

* Trial distributions: normal, kernel, exponential, gamma, half-normal, Rayleigh, and Weibull distributions.

Step II.4. One $\mathbf{X} \in g$ segment is chosen from the available ones, contributing to a *segment-to-model*, $\mathbf{X}_s^{[g]} = X_{sjk}^{[g]}$.

Step II.5. Each frequency bin k of values in $X_{sjk}^{[g]}$ are modeled through j seconds according to Table 1. Unity-long segments are not modeled but directly replicated. The $j \in [2, \ldots, 9]$ long segments are fitted by uniform distributions, such as

$$\chi_{sk} : \mathrm{U}\left[\min_j X_{sjk}^{[g]}, \max_j X_{sjk}^{[g]}\right]. \tag{6.6}$$

If $j \in [10, \dots, 19]$, the modeling relies on normal distribution in the form of

$$\chi_{sk} : \mathrm{N}\left[\mathrm{mean}_j X_{sjk}^{[g]}, \mathrm{var}_j X_{sjk}^{[g]}\right]. \tag{6.7}$$

For longer segment-to-model, $j \geq 20$, a series of trial distributions are fitted: normal (N), kernel (K), exponential (E), gamma (G), half-normal (Hn), Rayleigh (R), and Weibull (W) models, which showed good capability in modeling. In each trial, a corresponding random sample of the same length is drawn. The trial distribution, with the smallest Kolmogorov–Smirnov distance to the data in $X_{sjk}^{[g]}$ at fixed g, s, k, is considered a representative distribution. Thus, $\chi_{sk} \sim X_{sjk}^{[g]}$ probability density array is built up bin by bin in the s-th segment.

Step II.6. In the s-th simulated segment, the DFT profile $\mathbf{Y}_{sj}$ corresponding to the j-th second is the random realization of χ_{sk}. A random variable is drawn from χ_{sk} per frequency bin until a positive value is obtained to counteract negative coefficients in the spectrum.

Step II.7. In the j-th second of the s-th segment, $\mathbf{Y}_{sj}$ is coupled with a uniformly distributed random phase, and inverse Fourier transformed to obtain a zero-mean Gaussian vibration $\mathbf{y}_{sj}$.

Step II.8. The DFT simulation and vibration synthesis is repeated for all j. The *segment-in-simulation* grows until the desired segment length $j = l'_s$ is achieved. Each j-th spectrum rests on the same array of probability densities, χ_{sk}.

Step II.9. The concatenation of j-th seconds in TD and TFD concludes the end of one simulated segment, such as $\mathbf{Y}_{sj} = \{\mathbf{Y}_{s,1} \prec \mathbf{Y}_{s,2} \prec \cdots \prec \mathbf{Y}_{s,J}\}$ and $\mathbf{y}_{sj} = \{\mathbf{y}_{s,1} \prec \mathbf{y}_{s,2} \prec \cdots \prec \mathbf{y}_{s,J}\}$ the symbol $\prec$ describing "*followed by.*"

Step II.10. Further segments are simulated by repeating *Steps II.2–9.*, from a random realization of $\{l'_s, r'_s\}$ pair to the concatenation of seconds. New segments are constructed until the sum of segment lengths arrives at supersedes the size of the measured signal, T. The simulation length in the 2nd run is set to match to longest measurement.

Step II.11. The concatenation of segments, such as $\mathbf{Y} = \{\mathbf{Y}_1 \prec \mathbf{Y}_2 \prec \cdots \prec \mathbf{Y}_S\}$ and$\mathbf{y} = \{\mathbf{y}_1 \prec \mathbf{y}_2 \prec \cdots \prec \mathbf{y}_S\}$ concludes the end of the u-th simulation.

Step II.12. If more simulation is carried out, the method repeats *Steps II.1–11.* until the necessary number of simulations, U, is obtained in the form of $\mathbf{Y}_U$ and $\mathbf{y}_U$, concluding the end of the current procedure.

Highlighting key steps of Column II., segments are simulated in the time-frequency domain from second to second. A random length and RMS are chosen from the previously established database, as in Fig. 6.2, per segment. Each segment-to-simulate may consist of several spectral profiles, which facilitate the modeling of each frequency bin according to Table 6.1. The probability density array produces random variables in each frequency bin with substantive consistency through time indices of a segment.

6.4 Results

This section introduces results from the two runs in separate subsections for unambiguity.

6.4.1 Results from the 1st run

Fig. 6.3 shows how each simulation differs in the 1st run. The measured vibration signal in pane *a)* $\mathbf{x}_1$ consists of transient events, and each simulation also mimics such short events, nevertheless at varying instances in panes *c,e,g)*. Distinctive TD behavior implies distinguishable TFD characteristics. Seemingly, the simulated spectrograms $\mathbf{Y}_1, \mathbf{Y}_2, \mathbf{Y}_3$ are neither darker nor whiter as X_1. Further to be highlighted here, series *a)* $\mathbf{x}_1$ incurred two examples of stopping the car at 350 and 2600 s providing STFT sections dominated by constant harmonic excitation around 25 Hz in *b)* $\mathbf{X}_1$. Constant harmonic excitation is also manifested in *d)* $\mathbf{Y}_1$ for short periods. Sections of *a)* $\mathbf{X}_1$ also introduce other accountable phenomena in the bandwidth 100–120 Hz at 1200 and 1770 s, best described as shocks. Similar high-frequency excitations are simulated in *h)* $\mathbf{Y}_3$ around 1200, 1910, 2280 s. Interesting to note, that the 0–50 Hz bandwidth is consistently darker compared to the upper halves in each STFT.

Further comparisons are explained by the Probability densities (pd) of TD- and (FD) moments in Fig. 6.4. Let $\eta_m^{(u \vee n)}$ denote the $m = 1, 2, 3, 4$-th TD moments over j seconds of either $n = 1$ measurement or $u = 1, 2, 3$ simulations. The pd of first TD moments, pd $\left(\eta_1^{(n=1)}\right)$, are not directly comparable to simulations in pane *a)*. Since distributions of pd $\left(\eta_1^{(u=1,2,3)}\right)$ from simulations show only a rudimentary spike at zero. While $\eta_1^{(n=1)}$ from the measurement is computed block wise in one-sec-long frames of $\mathbf{x}_1$, its fluctuation is natural. However, the inverse DFT with a uniformly distributed random phase from *Step II.7.* can only provide zero-mean Gaussian processes. In pane *b)* pd(η_2) supplies similarities in scale, location, and magnitude parameters of the distributions in. Similarly, suitable matches are inferred from *c)* pd(η_3). A degree of similarity for *d)* pd(η_4) is better viewed on log-horizontal scales, which holds further

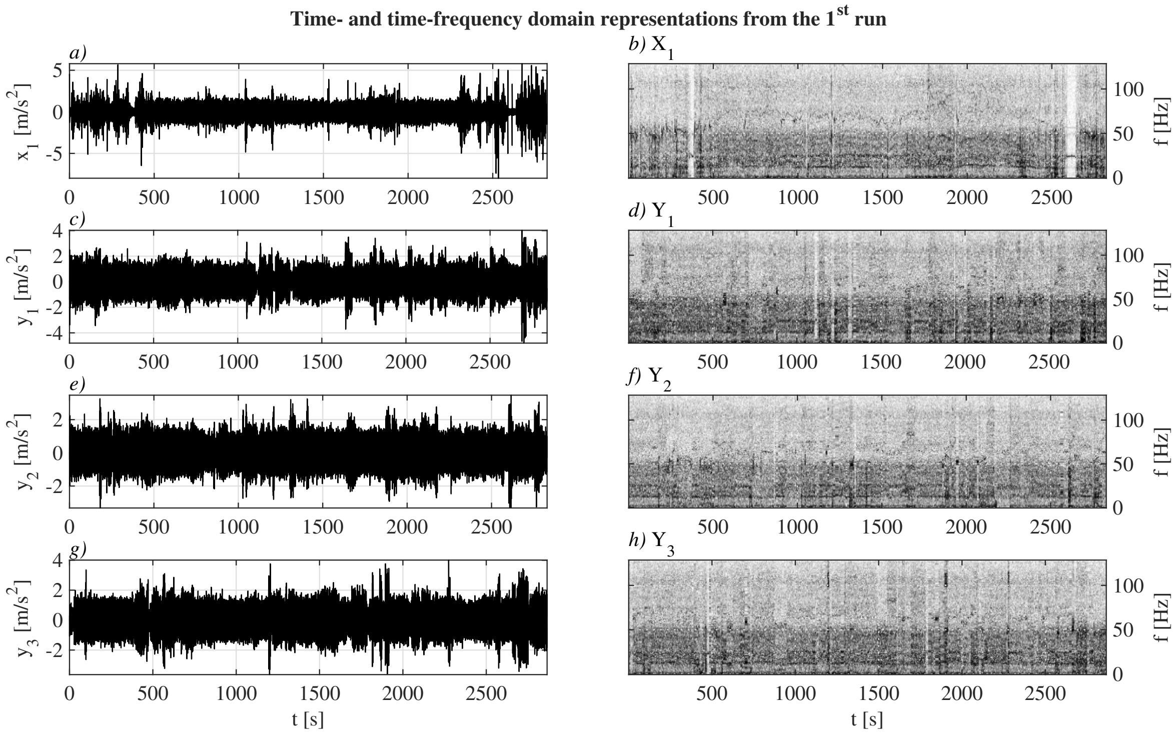

Figure 6.3: Measurements and simulation of the 1st run. The $n = 1$ measurement and the resulting $u = 1, 2, 3$ simulations in the 1st run per row, the time domain signals in the *left* column with corresponding short-time Fourier transform in the *right* column.

observations. Real-world RVV introduced kurtosis values orders of magnitudes higher than the simulations.

By similar considerations regarding the four spectral moments in panes *e–h)*, it can be concluded that a general consistency is found in $\mathrm{pd}(\mu_m)$ two-fold PDFs, directly comparable in the probability domain.

6.4.2 Results from the 2nd run

The 2nd run in Fig. 6.5 shows that the collected measurements $\mathbf{x}_1, \mathbf{x}_2, \mathbf{x}_3$ in panes *a,c,e)* obviously differ, while the simulated signal *d)* $\mathbf{y}_4$ also mutually differs. By visual examination, it can be concluded also here that $\mathbf{Y}_4$ overall is neither whiter nor darker compared to $\mathbf{X}_n$. It can be observed in the measurements, e.g. pane *f)* $\mathbf{X}_3$, how sweeping harmonic components can be obtained in reality. Such sweeping harmonics can be better examined in the enlarged STFT, $\mathbf{X}_3$ in Fig. 8.2, suggesting speed-dependent, drivetrain related causes. Simulations also presented harmonic components in Fig. 6.5.*h)* but rather, the hopping of articulated harmonic features can be observed instead of sweeping. In summary, a mutual difference between simulations and measurements can be deduced.

Regarding the 2nd run, it can be concluded by similar reasoning in Fig. 6.6 that probability densities for all but the first TD moments; furthermore, for all FD moments

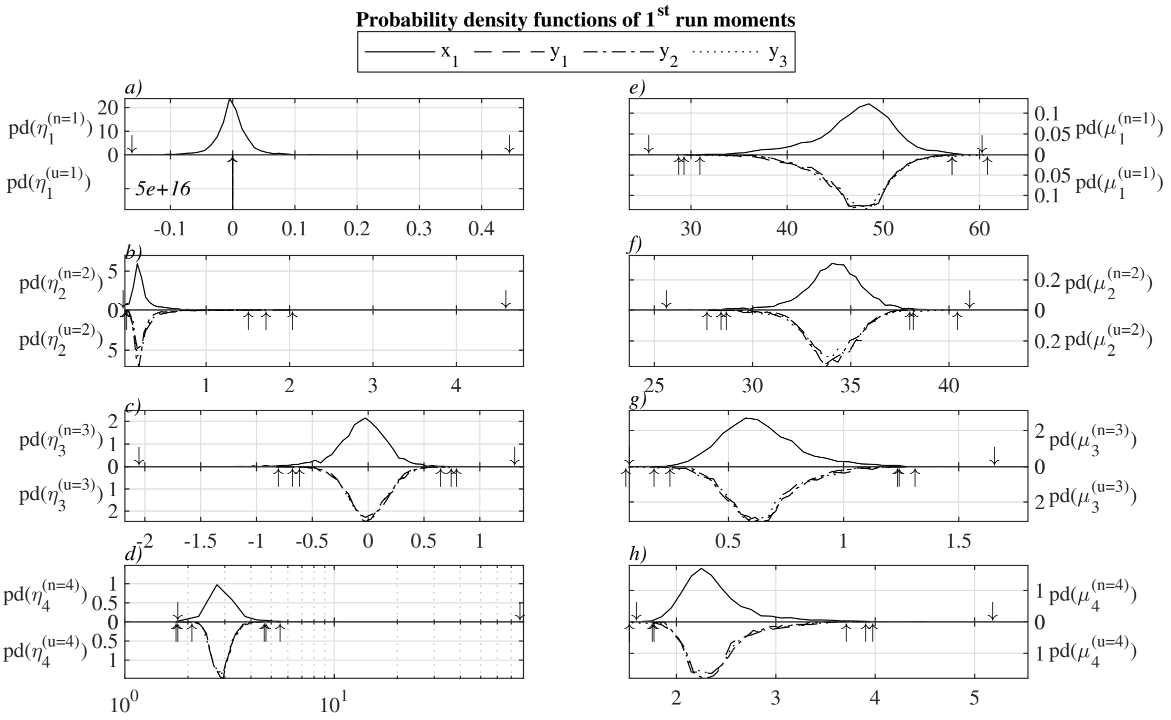

Figure 6.4: Two-fold probability density functions of moments in the 1st run. Comparison of time and frequency domain moments from $n = 1$ (*continuous*) measurements *above* and $u = 1, 2, 3$ (*dashed*, *dash-dotted*, *dotted*) simulations *below*, in the 1st run. Arrows show extrema per series in each half for the 1–4th time domain moments per seconds in panes *a–d)* respectively, and for the 1–4th frequency domain moments per seconds in panes *e–h)* respectively. The legend refers to the source signals.

represent a good match between measurements $n = 1, 2, 3$ and the simulation $u = 4$ in terms of the location, scale, and magnitude parameters of its distributions. Instead, the current paragraph highlights the algorithm's inherent mechanics in the case of multiple measurements. The distinctive characteristics of the third measurement $\mathbf{X}_3$ is helpful for presentation, in which case the gauge was installed directly on a chassis element of the trunk, yielding exacerbated harmonic components at app. 75 Hz in 800–1200 s. Also, certain road sections of the trip produced more noise, e.g., after 1500 s in Fig. 6.5.*f)*. Thus, well observable median differences of probability densities $\mathrm{pd}\left(\eta_2^{(n)}\right)$ and $\mathrm{pd}\left(\mu_2^{(n)}\right)$ are obtained among the experiments. Its simulated counterparts for $\mathrm{pd}\left(\eta_2^{(u)}\right)$ and $\mathrm{pd}\left(\mu_2^{(u)}\right)$ highlight how the procedure indeed utilized pooled samples of the three measurements, e.g., in *e)* $\mathrm{pd}\left(\mu_1^{(u)}\right)$ has a longer tail to the left (toward smaller bins), or *f)* $\mathrm{pd}\left(\mu_2^{(u)}\right)$ has a thicker tail to the right, and *g)* $\mathrm{pd}\left(\mu_3^{(u)}\right)$ reaches to the right, as well as *h)* $\mathrm{pd}\left(\mu_4^{(u)}\right)$ has thicker downhill on the left side.

Diverse phenomena can be found in real RVV, as in the case of $\mathbf{X}_3$ in Fig. 8.2. Similarly, simulations show various manifestations, highlighted on $\mathbf{Y}_4$ in Fig. 8.3. While the corresponding captions provide further details, here, general conclusions are summarized. The real RVV $\mathbf{X}_3$ shows constant harmonic excitation with harmonics and the similarly the simulation $\mathbf{Y}_4$, see annotations *a)*. Higher frequency excitations can be found around 75 Hz, see arrows *b)*. While $\mathbf{X}_3$ shows smooth frequency modulation, it cannot be expected in the simulations due to random sampling. $\mathbf{X}_3$ provides broadband excitation for prolonged periods, similarly $\mathbf{Y}_4$, see points *c)*.

6.4.3 Verification

The approach is verified according to the scheme presented in Fig. 6.9. The $\mathbf{l}_n$ and $\mathbf{r}_n$ in *Step I.4.* are readily available. Introducing the simulated signals $\mathbf{Y}_u$ to the same CpD the segment length and -RMS distributions $\mathbf{l}''_u$ and $\mathbf{r}''_u$ from the simulations are directly comparable. Fig. 6.10 reports the comparisons below the average DFT profiles. From the 1st run, the time-averages of $\mathbf{X}_1$ and $\mathbf{Y}_u$ for $u = 1, 2, 3$ profiles show close-to-identical similarities; similarly the segment length and -RMS probability density functions in panes *b,c)*. By the 2nd run in panes *d,e,f)* slightly different spectral characteristics can be observed between measurements, whereas $\mathbf{Y}_4$ is positioned somewhere in-between $\mathbf{X}_1, 2, 3$, as expected. The probability density of segment lengths remains close to identical. The segment RMS PDF provides a good confirmation of pooled sampling in case of multiple measurements.

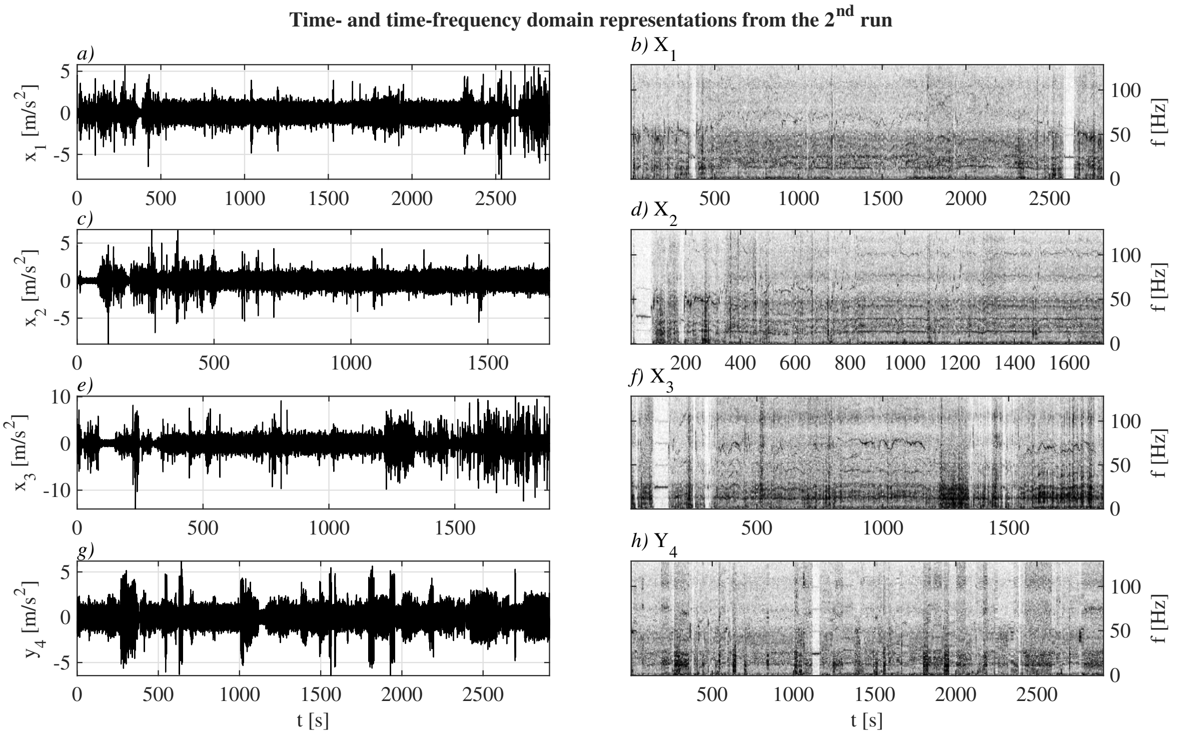

Figure 6.5: Measurements and simulation of the 2^{nd} run. The $n = 1, 2, 3$ measurements and the resulting $u = 4$ simulation in the 2^{nd} run per row, the time domain signals in the *left* column with corresponding short-time Fourier transform in the *right* column.

6.4.4 Non-Gaussian and non-stationary nature

RVV processes are well-known to undergo a non-Gaussian nature, having transients being much further away from $\pm 3\sigma$ limits and a leptokurtic state. Therefore, the measurements and simulations are tested against the null hypothesis that "*the series has a Gaussian distribution.*" The p-value from the Anderson–Darling tests (p), accompanied by the kurtosis values (η_4), are reported in Table 6.2. The current study also presented evidence against the non-Gaussian nature of RVV from passenger cars in all cases.

The non-stationary nature is further investigated in the measurements and simulations. Non-stationarity can be analyzed in time-, frequency-, and time-frequency domain features, e.g., by spectral entropy, H. For the power spectrum $S_{jk} = |X_{jk}|^2$ with the marginal power spectrum $S_k = \sum_{j=1}^{J} S_{jk}$, the normalized power spectrum P_k becomes

$$P_k = \frac{\sum_{j=1}^{J} S_{jk}}{\sum_{k=1}^{K} \sum_{j=1}^{J} S_{jk}}, \tag{6.8}$$

from which the spectral entropy is

$$H = -\sum_{k=1}^{K} P_k \log_2 P_k, \tag{6.9}$$

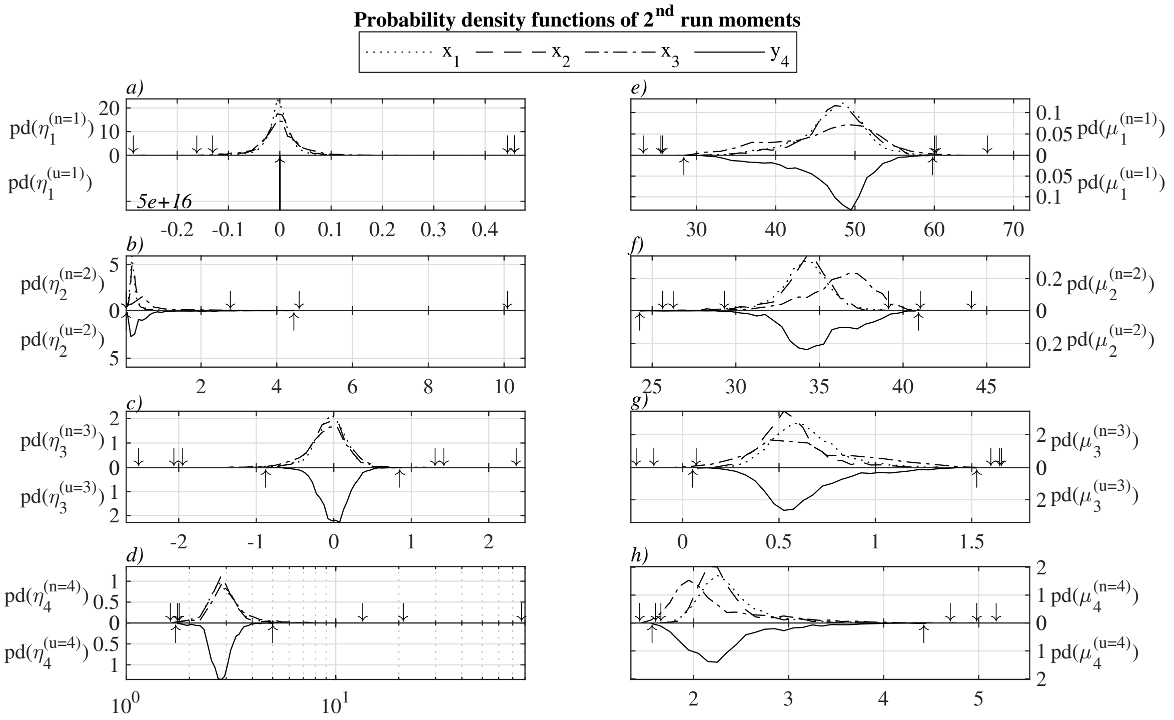

Figure 6.6: Two-fold probability density functions of moments in the 2nd run. Comparison of time and frequency domain moments of $n = 1, 2, 3$ (*dotted*, *dashed*, *dash-dotted*) measurements *above* and $u = 1$ (*continuous*) simulation *below*, in the 2nd run. Arrows show extrema per series in each half for the 1–4th time domain moments per seconds in panes *a–d)* respectively, and for the 1–4th frequency domain moments per seconds in panes *e–h)* respectively. The legend refers to the source signals.

Table 6.2: Statistics on non-Gaussianity and non-stationarity. Anderson–Darling tests (p-value), kurtosis (η_4), normalized spectral entropy (h), instantaneous normalized spectral entropy (h_j) and frequency-bound normalized spectral entropy (h_k) statistics of measurements and simulations.

1st run	$\mathbf{x}_1$	$\mathbf{y}_1$	$\mathbf{y}_2$	$\mathbf{y}_3$
p	0.00	0.00	0.00	0.00
η_4	7.57	4.18	3.82	4.07
h	0.89	0.89	0.89	0.89
h_j	0.76 ± 0.09	0.76 ± 0.07	0.76 ± 0.07	0.76 ± 0.08
h_k	0.88 ± 0.04	0.90 ± 0.04	0.90 ± 0.04	0.89 ± 0.06
2nd run	$\mathbf{x}_1$	$\mathbf{x}_2$	$\mathbf{x}_3$	$\mathbf{y}_4$
p	0.00	0.00	0.00	0.00
η_4	7.57	7.32	10.73	6.53
h	0.89	0.88	0.83	0.86
h_j	0.76 ± 0.09	0.75 ± 0.10	0.72 ± 0.11	0.74 ± 0.10
h_k	0.88 ± 0.04	0.88 ± 0.04	0.87 ± 0.03	0.87 ± 0.04

p is less than the smallest tabulated value, returning 0.0005.

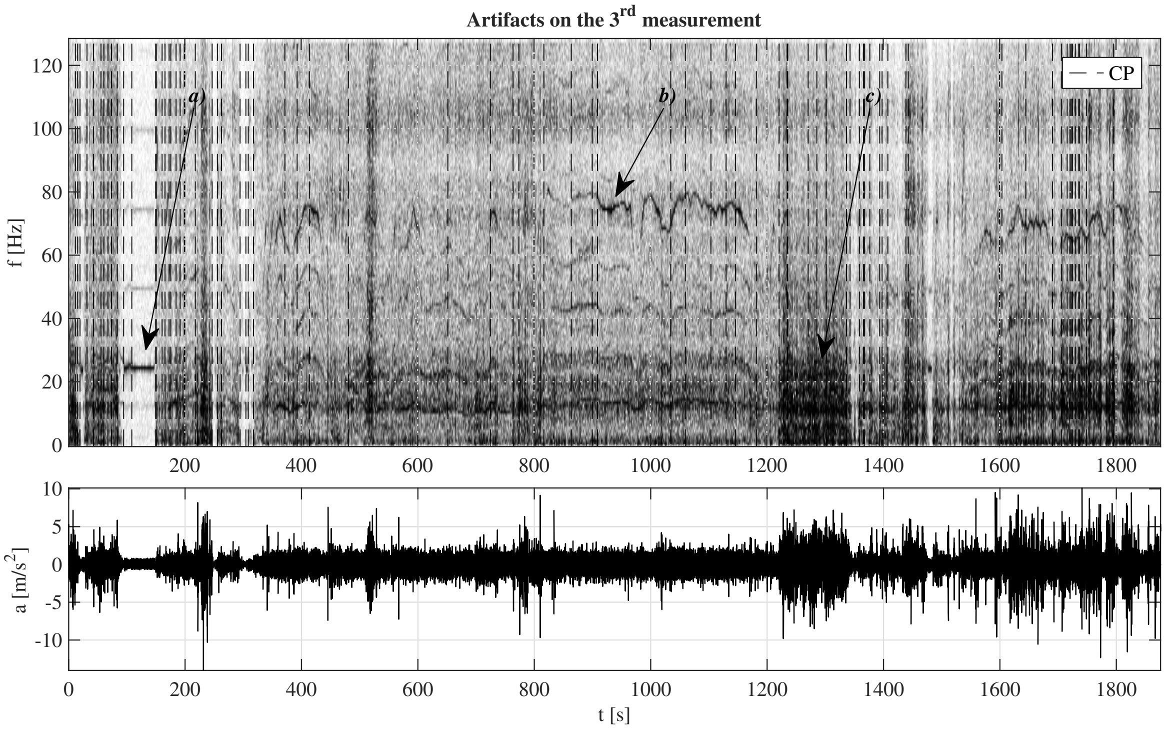

Figure 6.7: Artifacts on the short-time Fourier transform of the 3rd measurement. The gray-scale surface is overlayed by segment borders (*dashed line*) in the upper pane. Various effects can be seen in the spectrogram, such as *a)* constant harmonic excitation and its harmonics, possible one sub-harmonic; *b)* drifting harmonic excitation; *c)* broad-band excitation for a prolonged period dominated by frequency range app. $[1, 50]$ Hz between $[1220, 1320]$ s.

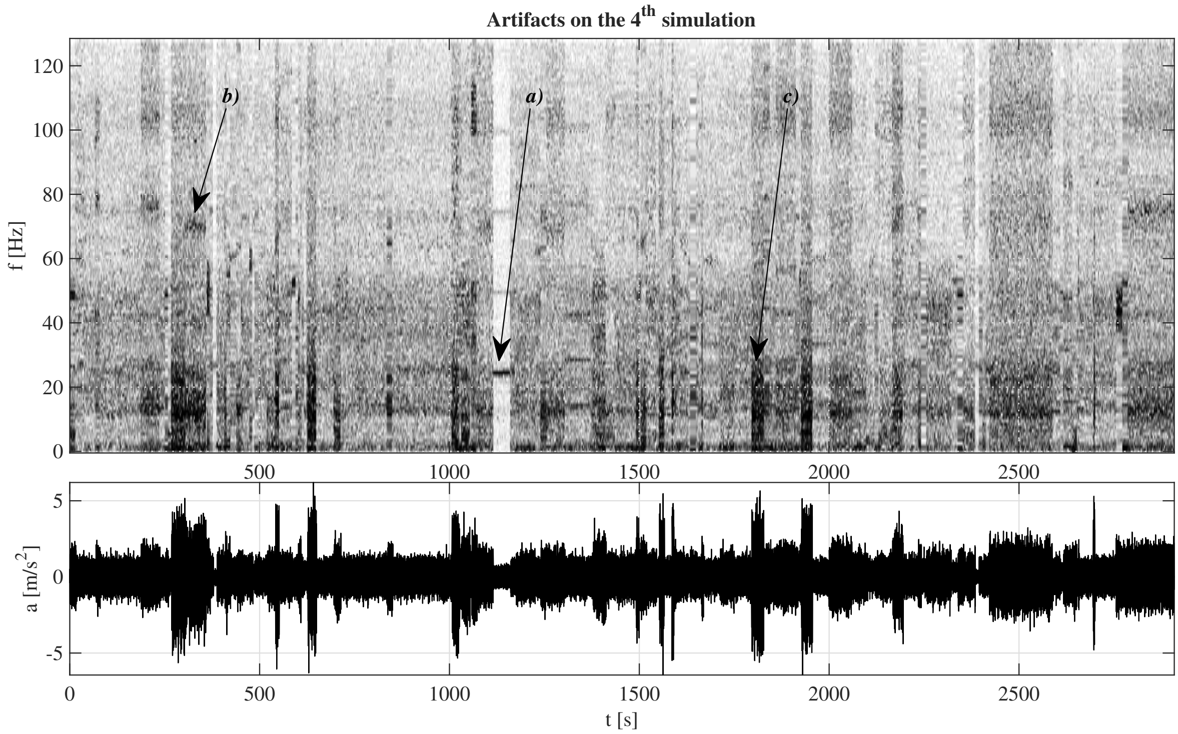

Figure 6.8: Artifacts on the short-time Fourier transform of the 4th simulation. In the upper pane: *a)* simulated stop, i.e., constant harmonic excitation with harmonics, *b)* harmonic component with possible sub-harmonincs blended in background noise, *c)* broad-band noise.

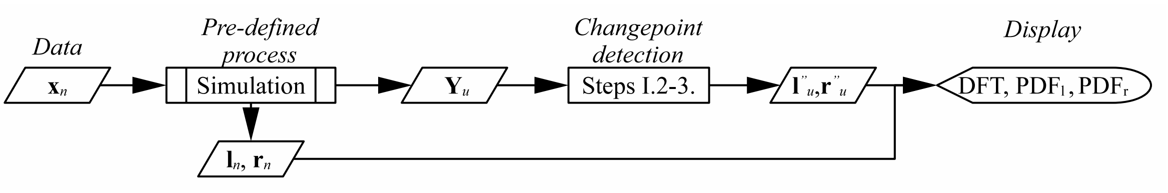

Figure 6.9: Verification process. Each run produced $\mathbf{Y}_u$ simulations from $\mathbf{x}_n$ measurements. Simulated STFT profiles are subjected to *Changepoint detection.* The resulting DFT profiles, PDF of segment lengths, and PDF of segment RMS are compared to the ones from measurements, being on view in Fig. 6.10 per run.

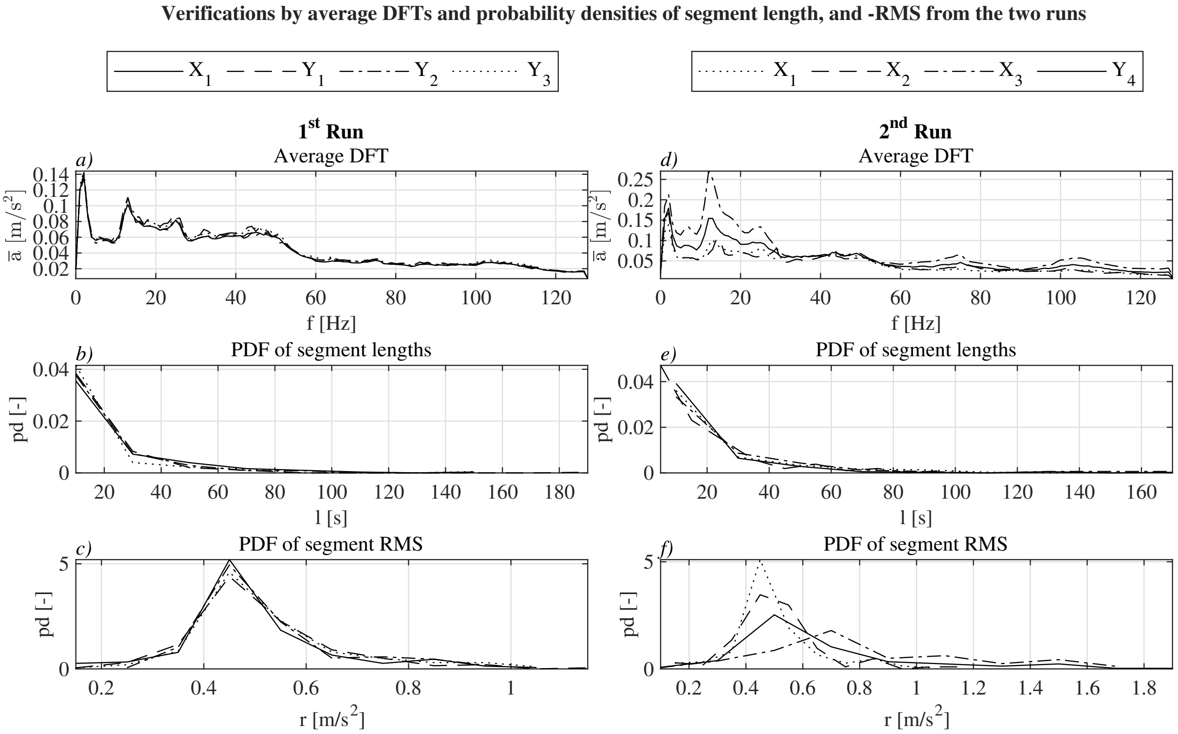

Figure 6.10: Comparison of N measurements and U simulations. On the *left* side, pane *a)* average DFT profiles, *b)* PDFs of segment length, and *c)* PDFs of segment RMS in case of the 1st run. On the right side, pane *d)* DFT, *e)* λ, and *f)* ρ distributions from the 2nd run. Note, that legends show the origin STFT matrices for conciseness. The legend refers to the source signals.

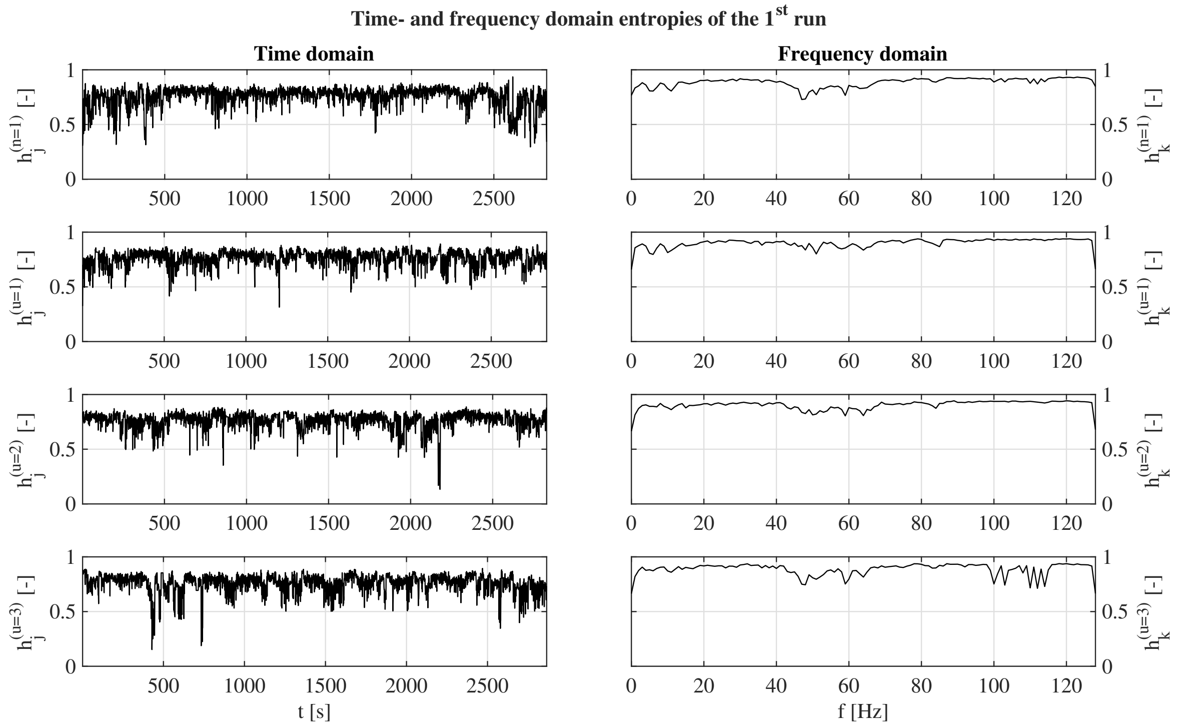

Figure 6.11: Spectral entropies of the 1st run. Instantaneous normalized spectral entropies (h_j) for $n = 1$ measurement and $u = 1, 2, 3$ simulations in the *left* column, frequency-bound normalized entropies (h_k) in a similar fashion in the *right* column.

and the normalized spectral entropy is

$$h = \frac{H}{\log_2 K}, \tag{6.10}$$

the denominator describing the spectral entropy of a white noise process, following uniform distribution in the frequency domain. Since X_{jk} is available, the entropies might be also investigated as a function of time and frequency. In the former case, h_j denotes the instantaneous normalized spectral entropy in the j-th second as follows

$$P_{jk} = \frac{S_{jk}}{\sum_{k=1}^{K} S_{jk}}, \tag{6.11}$$

$$H_j = -\sum_{k=1}^{K} P_{jk} \log_2 P_{jk}, \tag{6.12}$$

$$h_j = \frac{H_j}{\log_2 K}. \tag{6.13}$$

Similarly, as a function of frequency, the summations in Eq. 11–12 happen by time-index j in a fixed bin k, resulting in a frequency-bound H_k, which normalized by $\log_2 J$ yields h_k. Fig. 6.11, 6.12 show that the normalized entropies provide similar variations between measurements and simulations, also quantified in Table 2.

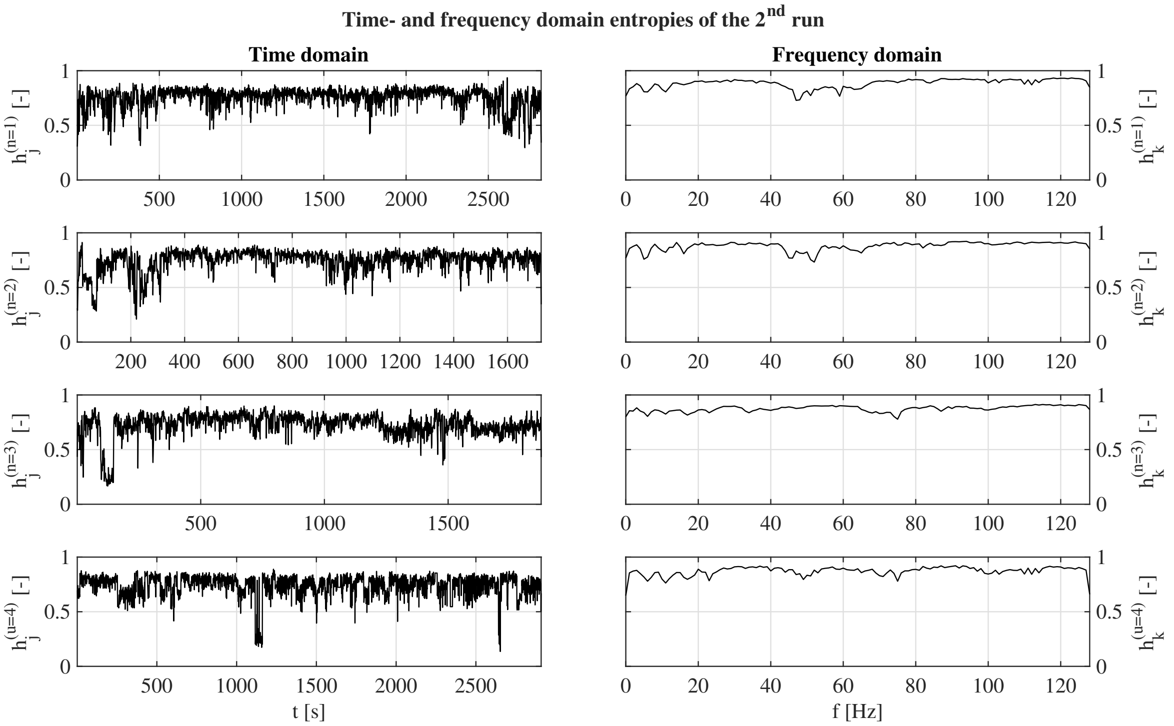

Figure 6.12: Spectral entropies of the 2nd run. Instantaneous normalized spectral entropies (h_j) for $n = 1, 2, 3$ measurements and $u = 4$ simulation in the *left* column, frequency-bound normalized entropies (h_k) in a similar fashion in the *right* column.

6.5 Discussion

The current study suggests that the long-criticized approach of time-history replication still has remarkable benefits but by a different approach. A practical alternative is presented above, emphasizing probability-based choices, hence the name Probability-based spectrogram synthesis (PBSS).

Anomaly in the long-term had not been found in Fig. 6.10. The verification confirms the approach of probability-based choices on segment length and RMS, supplying a reasonable approximation of real-world RVV. Furthermore, the consistency between average DFT profiles in panes *a,d)* supports the second form of probability-based modeling by terms of Table 1. These findings show that PBSS may beneficially synthesize broad-band excitations with shocks and solid harmonic components.

6.5.1 Deductive arguments

As expected, the first-order TD moments are characteristically misaligned in Fig. 6.4.*a)* and Fig. 6.6.*a)*. Instead of echoing *Step II.7.*, it suffices to say that no other distribution could have been obtained by simulation. Since the concerned 2–4 TD moments showed proper matches in each half of the two-fold PDFs and the investigated FD moments are adequately mirrored, it is deduced that PBSS can provide sufficient representation in the probability domain, though, excessive peaks are not typical.

Since TD variance is not constant, as Fig. 6.4.*b)* and Fig. 6.6.*b)* lower panes illustrate, it is concluded that a variance, conventionally σ-modulated, random vibration signals can be obtained, contributing to non-stationarity. The Fig. 6.13 further confirms this by $\mathbf{y}_3$ with its TD moments and $\mathbf{Y}_3$ with FD moments along time, presenting the variability in the second TD moment series.

6.5.2 Arguments on limitations

Transient events occur in simulated signals, but moderated peak levels can be still achieved. The underlying reason can be best understood by the initially set time resolution of STFT, presented by one-sec. frames here. Thus, applications mainly concerned about excessive shocks may further tune parameters. It is speculated that TD manipulations, e.g., ZMNL [129] may increase peak levels in simulated shocks. Another suggestion is the direct replay of shocks, although beforehand, either manual or an automated but rigorous shock extraction should be conducted.

A good agreement of strong harmonic components has been achieved between measurements and simulations. Although the peak frequency components are smeared in the simulated STFT, see Fig. 8.2.*b)* and Fig. 8.3.*b)*. The frequency-modulation in $\mathbf{X}_3$ is easily understood by human recognition, that smoothness in simulations is only possible in a distinct manner due to spectrograms being segmented at each CP through the whole bandwidth. In surplus, the random variables of segment length are independent, thus, they are primarily dispersed in time.

The current section concludes that the above limitations can be well-understood by traditional trade-offs in signal processing and statistical modeling. However, a typical dilemma is left for here: certain disciplines, such as PVT, are often interested in analyzing hour-long time series. Then the signal processing needs to balance the computational efficiency and a good resolution. While STFT under-performs, e.g., Stockwell transform, or Continuous wavelet transform in terms of a fine resolution, the latter two exemplary methods applied on current signals ran out of memory under everyday circumstances (16 GB RAM).

6.5.3 Arguments on modeling

Further comparisons are extended to the modeling of segment length, $\mathbf{l}_s = \mathbf{l}_n \cup \mathbf{l}''_u$, and RMS distributions, $\mathbf{r}_s = \mathbf{r}_n \cup \mathbf{r}''_u$, illustrated on Fig. 6.14. The probability distribution of segment lengths, “s”, had been modeled by

$$p(s) = C/\sinh(ks) \tag{6.14}$$

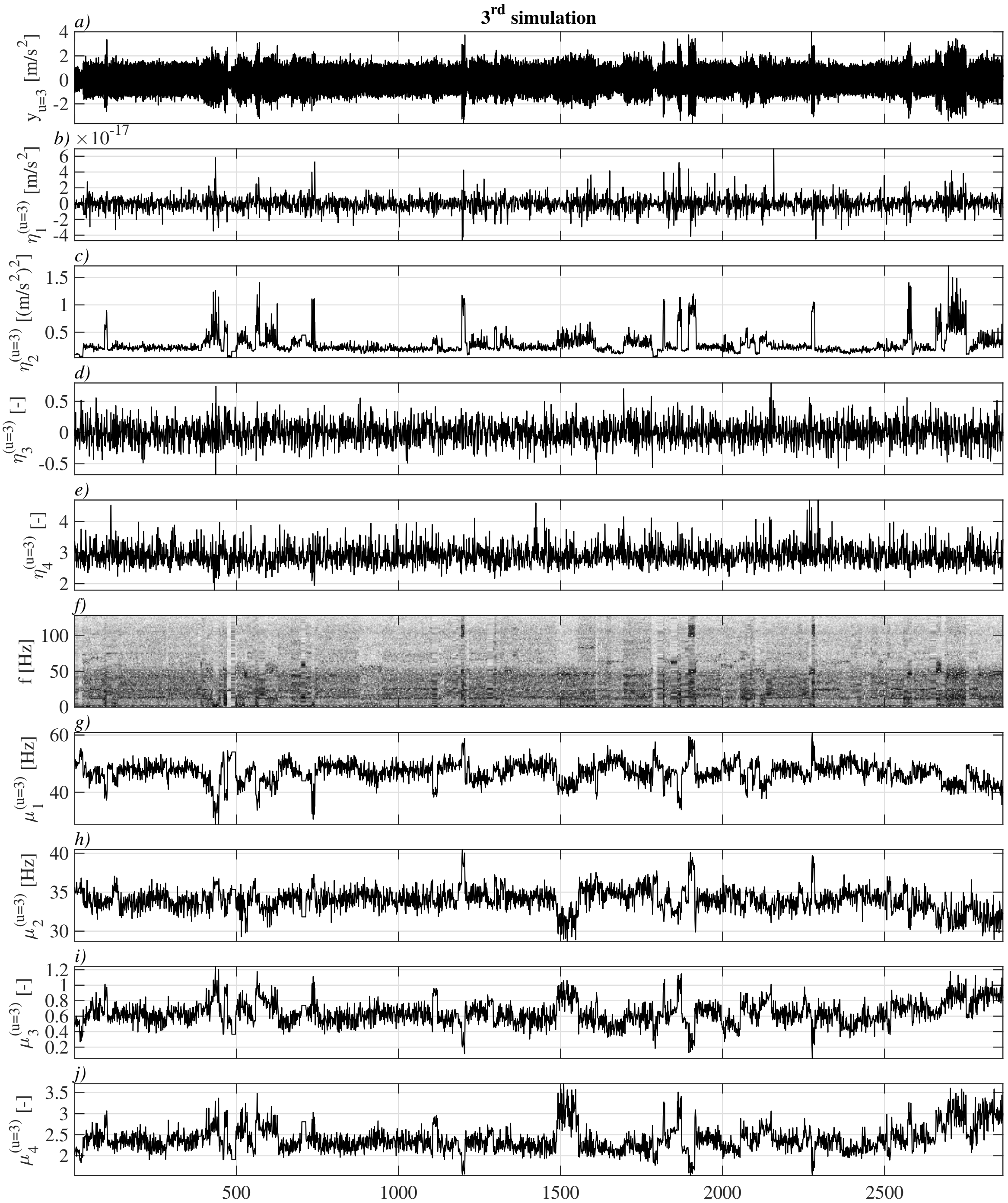

Figure 6.13: Time- and frequency domain moments from the 3rd simulation. Pane *a)* simulated signal in time domain, and its 1–4th time domain moments per seconds, in *b–e)* respectively. Pane *f)* short-time Fourier transform of the simulation, and its 1–4th frequency domain moments per seconds, in *g–j)* respectively.

hyperbolic function, and empirically found constants of $C \approx 4$ and $k \approx 1/4$ had been used [132, Eq.15]. In this paragraph substituting the notations $s \to \mathbf{l}_s$, the $C \approx 8.9$ and $k \approx 0.03$ values are found by least squares fitting. This might suggest that the distribution of spectrally homogeneous segment lengths might differ from amplitude-type non-stationarities; or itself the subject of experiments, namely passenger cars, contribute to different distribution than obtained from trucks in [132]. Despite the difference, the proposed model can be successfully deployed for typical segment length distributions since it excels in contrast to the exponential distribution in higher regions, where the exponential distribution does not account for longer segments.

The modeling of probability density of segment RMS, $\mathbf{r}_s$, introduced further challenges in the literature. The modified four-parameter Weibull distribution (4W), such as

$$P(x) = \begin{cases} 0 & ,\forall x \in \left]-\infty, x_0\right[\\ \frac{\beta}{\alpha\Gamma[\gamma/\beta]} \left(\frac{x-x_0}{\alpha}\right)^{\gamma-1} \cdot \mathrm{e}^{-\left(\frac{x-x_0}{\alpha}\right)^{\beta}} & ,\forall x \in \left[x_0, +\infty\right[\end{cases} \tag{6.15}$$

proposed in [138, Eq.9] showed to be a better modeling, compared to a three-parameter Weibull distribution (3W). Fig. 6.14.*b)* shows that the 3W method can under-represent the PDF of $\mathbf{r}$, while the 4W model provides a better approximation but under-represented tail-distributions.

Speculatively, if the amplitude- and frequency-type non-stationarities lead to different distributions of segment lengths, it implies on the long-terms that the joint probability space of segment lengths provides more adequate representation; consequently, the RMS distributions would be again indirect results.

6.5.4 General arguments

The literature of PVT distinguished amplitude- and frequency type non-stationarities in RVV and studied vibration level variations, transient events, and harmonic excitation, which distinctions allowed a better understanding of the constituents. The current chapter presented a unified approach to the simultaneously occurring amplitude- and frequency modulation in RVV.

Use cases may emanate from 1) the analyst has a limited number of measurements and wishes to conduct many different simulations, or 2) already an ensemble of RVV series is on hand and simulations shall be obtained as a general approximation of RVV but in a respective manner. Also, if 3) experiments had been conducted by varying the gauge's location and a pooled sampling is applicable.

Generality rises from simulations being different in each loop of (j, s, u), and the respective manner is laid down in the data-driven approach of DFT synthesis. Also, the analyst is advised to investigate the applicability of a given test signal in the necessary domains before commanding any equipment to reproduce it.

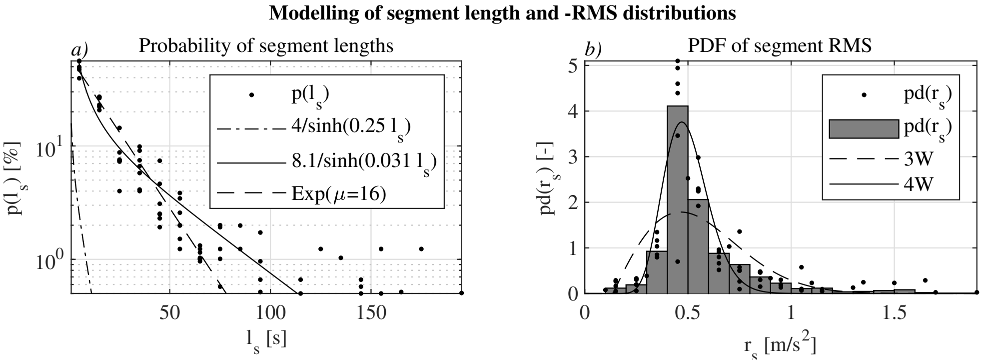

Figure 6.14: Modeling of segment length and -RMS distributions. Pane *a)* shows segment length probabilities of $\mathbf{l}_n$ from measurements and $\mathbf{l}''_u$ from simulations, together as $\mathbf{l}_s = \mathbf{l}_n \cup \mathbf{l}''_u$. The *scatter* shows the probabilities on common binning, *dash-dotted* line corresponds to [132, Eq.15], *continuous* line represents current fit, and *dashed* line corresponds to the exponential model. Pane *b)* shows segment RMS probability densities of $\mathbf{r}_n$ from measurements and $\mathbf{r}''_u$ from simulations, together as $\mathbf{r}_s = \mathbf{r}_n \cup \mathbf{r}''_u$. The *scatter* shows the probability densities individually for each sub-series of $\mathbf{r}_s$, *histogram* corresponds to the probability density from the concatenated series of $\mathbf{r}_s$, *dashed* line represents the three-parameter Weibull model based on concatenated series, and *continuous* line corresponds to the four-parameter Weibull model [138, Eq.9] based on the *scatter*.

6.5.5 Conclusion

The current chapter introduced the non-stationary simulation method, Probability-based Spectrogram Synthesis (PBSS). Timely appearance and various manifestations of most accountable artifacts in simulated spectrograms are likely to be met. An arbitrary number of distinctive simulations can be obtained from unlimited measurements. The simulation uses pooled sampling in the case of multiple measured series. Probability densities of the 2–4$^{\text{th}}$ time domain moments and the 1–4$^{\text{th}}$ frequency domain moments present noteworthy alignment between measurements and simulations. The 1$^{\text{st}}$ time domain moment of simulations is not an applicable metric here. Frequency modulation is principally possible but not necessarily through consecutive spectrums. Amplitude modulation is manifested as σ-modulation. Natural transients shorter than the time-resolution of the STFT loose energy concentration in simulation. Harmonics can be smeared around peaks in a spectrogram. Future research may investigate the possibilities of increasing the kurtosis of simulated transients. Modeling possibilities by joint distribution of frequency domain moments should follow.

Thesis 5. A simulation routine can be constructed that can reflect spectral variations in the time-frequency domain in a realistic manner; which simulates an arbitrary number of different time-frequency domains from a single measurement realization; furthermore, which simulates aggregate statistical properties of the registered road vehicle vibrations. Verifying this claim, I have presented the *Probability-based Spectrogram Synthesis* procedure for simulating the 2$^{\text{nd}}$, 3$^{\text{rd}}$, and 4$^{\text{th}}$ spectral moments. Practical implications of the thesis are:

5.1 Changepoints in the time-frequency domain can found simultaneously for transient events, changes in the root mean square of the signal, and the appearance of harmonic excitations in the road vehicle vibration signals.

5.2 Methods relying on magnitude modulation bypass the need for *a priori* and heuristic adjustment of many parameters.

5.3 Road vehicle vibrations can be directly simulated in the time-frequency domain.

5.4 Modeling and simulation based on measured data outperforms in variability the time-history replication method. ■ *Ref.*: [10]

Chapter 7

Clustering spectrums

Research on the non-stationary nature of Road vehicle vibrations (RVV) led to advances in simulating such processes. Contemporary methods introduced for the analysis of RVV primarily aimed at partitioning the signal in the time- or time-frequency domain, providing differing segments of a signal. However, a degree of dissimilarity, or conversely similarity, is still challenging to find. Hereunder it is argued that in some cases, merely a statement of dissimilarity between neighboring segments within a signal might be well-enough, though from a broader perspective, the assessment of the similarity of Discrete Fourier transforms (DFT) may be the next practical step forward. For this reason, the current chapter presents the hierarchical clustering of elements of the Short-time Fourier transform (STFT) plane from an RVV measurement; secondly, it introduces a clustering validation metric to arrive at an optimum distance metric and a threshold to use in binary hierarchical clusters.

7.1 Introduction

Let us suppose that an STFT is appropriately segmented, each segment consisting of one or more DFT profiles. Let us further assume that the segments are characterized by one *representative* profile, e.g., the average DFT profile of that segment. We wish to investigate the similarities of representative DFT spectra of segments. Therefore, the current article provides a methodology for measuring DFT vector similarity from the STFT of RVV. Instead of figuring out completely artificial examples of representative DFT profiles, a recording in Fig. 7.1.*a)* is provided, serving as a *population*; apparently, its elements are ordered in time. The so-called representative samples are drawn randomly from the population.

The field of clustering is maturing with a wealth of procedures and algorithms. Several approaches and their different taxonomies are available. A comprehensive review of methods would escape the possibilities of the current section. However, a common taxonomy is discussed in [139], defining *hierarchical* and *partitional* clustering families at the first grouping level. Hierarchical clustering techniques provide a hierarchical sequence of divisions according to a similarity-based criterion for merging or dividing clusters. Partitional clustering approaches identify the partition that optimizes a clustering criterion. While hierarchical techniques create a nested series of partitions, partitional clustering simply creates one.

Other introductions may distinguish first the families of hard- and soft clustering. In *hard* clustering, an object can belong only to one cluster; in *soft* (or *fuzzy*) clustering, objects can belong to more than one cluster. In the latter case, a fuzzy clustering may be transformed into a hard clustering by allocating each pattern to the cluster with the highest membership. Standard techniques for hard clustering are hierarchical clustering and k-means; and Gaussian mixture models or fuzzy C-means for soft clustering.

The primary benefit of hierarchical clustering methods is that the number of clusters does not have to be specified *a priori*. Dendrograms provide appealing representations assisting the clustering; however, they also introduce the typical dilemma of defining a threshold of distances by which cluster boundaries can be determined. The first and most subjective solution to this question is a visual examination, followed by a subjective decision. While this might not provide a proving ground, the visual assessment is more or less unavoidable in clustering, which can be assisted by other qualitative figures, e.g., silhouette plots [140]. Thus, one might classify subjective decisions as *manual evaluation*. Researchers also introduced dozens of metrics to validate clustering results by boiling down the problem to single metrics. The *external evaluation* covers the comparison of the given results to ground truth, if available. Some of the often-favored internal evaluation metrics follow here [141]. The Variance ratio criterion [142] balances the within-cluster variation against the between-cluster variation in Euclidean spaces. The Dunn family of indices [143] formalizes the idea of a ratio between the between-cluster separation and within-cluster compactness for general dissimilarity data. The Average silhouette width criterion [144] is a trade-off concerning the between-cluster separation and the within-cluster homogeneity. The CDbw-index [145] assesses the separation and compactness of clusters. The Clustering validation index based on nearest neighbors [146] proposed an alternative idea to measure separation, which does not excavate dissimilarity values; instead, it is based on how many of the k-nearest neighbors of each observation are in the same cluster. The reader is referred to [147] for a more extensive list of validation metrics.

Here, a hypothesis is projected. Once a generally accepted segmentation technique is adopted, it is speculated that the similarity of DFT or Power spectral density (PSD) profiles from segments, needs to be analyzed. While the future is unknown, it remains a potent guess that clustering methods offer prominent techniques in this question.

The process introduced here is based on the idea of defining a threshold, which maximizes the number of clustered spectrums beneath an overall low spread. Although

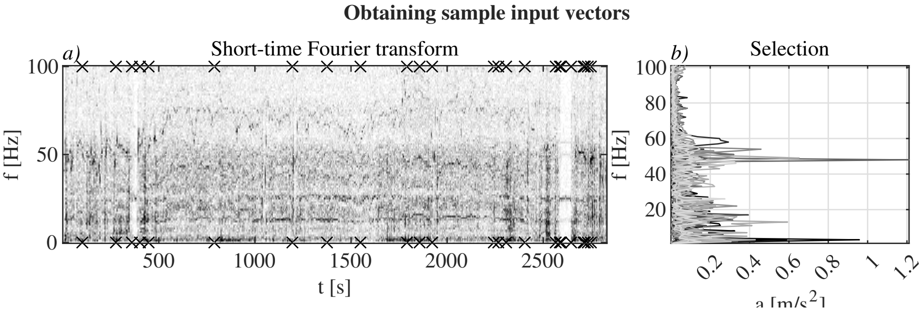

Figure 7.1: Sample DFT vectors are randomly selected from the same population in *a)* denoted by "×" at $f_1 = 1; f_{101} = 101$ Hz. Pane *b)* shows the selected vectors in the frequency domain.

one of the above validity indices could have been adopted; instead, the present technique gives a straightforward and more tactile measure.

7.2 Methods

The technique is shown first on a random sample from the STFT of an RVV measurement to illustrate the clustering process, yielding an optimum distance metric beneath an optimum parameter setting. Then, the application is repeated many times for a probabilistic appraisal of arriving at such optima. Section 7.2.1 introduces the establishment of DFT vectors to be clustered. A broad introduction to dendrograms follows it, and various distance metrics are discussed Sec. 7.2.2. Next, the distributions of distances by various metrics are illustrated Sec. 7.2.3; afterwards, the optimality criterion follows in Sec. 7.2.4.

7.2.1 Source data

A DC MEMS accelerometer measured the vertical acceleration of a passenger car with a sampling frequency of 1024 Hz, placed in the coin toss behind the handbrake of a Suzuki Swift Sedan 1.3 GLX (2002). The journey took place in everyday traffic conditions. The obtained series is high-pass filtered with a 1 Hz cut-frequency; however, the spectrogram is accounted only up to 100 Hz, as let through an ideal low-pass filter, in order to reduce computational needs. The resulting STFT matrix without overlapping of one-sec-long timeframes is plotted in Fig. 7.1.*a)*. Twenty-five timepoints, t_k, are randomly selected from the STFT matrix, yielding the first sample.

7.2.2 On the use of dendrograms

A brief introduction to dendrograms follows, whereby the frequent notations are illustrated in Fig. 7.2. The *objects* may have one or more dimensions, e.g., single points on

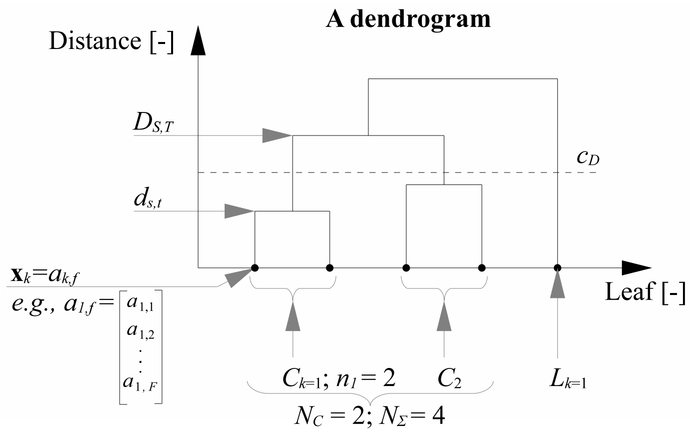

Figure 7.2: A dendrogram showing five leaves combined into two multi-element clusters, C_k, and one lone branch, L_k, at the utilized cutting height, c_D. The number of leaves in the k-th multi-element cluster is n_k, the number of multi-element clusters is N_C, while the number of clustered objects is N_Σ.

an axis, coordinate pairs in a plane, coordinates in a three-dimensional space, etc. Here, each $\mathbf{x}$ itself is a DFT vector from the STFT plane. Let us imagine a tree upside down as in Fig. 7.2. The *tree* (a dendrogram) is built up from branches, each one ending in one *leaf* or object. Currently, the k-th DFT vector $\mathbf{x}_k = a_{k,f}$ is the k-th leaf comprising $f = 1, 2, \ldots, F$ frequency bins. Here, defining a cutting height at c_D (viz. a threshold for *distance*), some branches fall, yielding clusters with multiple leaves as *collectives*, C_k, and a *lone* branch holding only one leaf, L_k. (*Singleton* is the common term for a stand-alone leaf, but the notion s is spared for *source* later.) The number of leaves in the k-th multi-element cluster is denoted by n_k, and the number of multi-element clusters is N_C, while the number of clustered objects is represented by N_Σ .

As the *first step*, one aims to find the similarity between the pair of objects given a distance measure [148, pp.3925–3926], called here *metrics*. Common similarity metrics are Euclidean-, standardized Euclidean-, Chebyshev-, cosine-, correlation-, and Spearman distances, respectively $M_m = \{\mathrm{EUC}, \mathrm{SEU}, \mathrm{CHE}, \mathrm{COS}, \mathrm{COR}, \mathrm{SPE}\}$ as of Eq. 7.1–7.6.

For $\mathbf{x}_s$ source- and $\mathbf{x}_t$ target objects in general, each representing a row vector, the Euclidean distance is

$$d_{s,t}^2 = (\mathbf{x}_s - \mathbf{x}_t)(\mathbf{x}_s - \mathbf{x}_t)' \tag{7.1}$$

the square root of the scalar product of the difference vector $(\mathbf{x}_s - \mathbf{x}_t)$. The standardized form of the Euclidean distance is

$$d_{s,t}^2 = (\mathbf{x}_s - \mathbf{x}_t)\mathbf{V}^{-1}(\mathbf{x}_s - \mathbf{x}_t)' \tag{7.2}$$

where $\mathbf{V}$ is the $n \times n$ diagonal matrix whose j-th diagonal element is S_j^2 . The term $\mathbf{S}$

is a vector of scaling factors for each dimension. The Chebyshev distance,

$$d_{s,t} = \max_j \left\{ |x_{s_j} - x_{t_j}| \right\} \tag{7.3}$$

expresses the maximum of absolute of difference vector between source and target objects. The cosine distance,

$$d_{s,t} = 1 - \frac{\mathbf{x}_s \mathbf{x}_t'}{\sqrt{(\mathbf{x}_s \mathbf{x}_s')(\mathbf{x}_t \mathbf{x}_t')}} \tag{7.4}$$

is one minus the cosine of included angle between points (treated as vectors). Correlation distance is defined as

$$d_{s,t} = 1 - \frac{(\mathbf{x}_s - \overline{\mathbf{x}}_s)(\mathbf{x}_t - \overline{\mathbf{x}}_t)'}{\sqrt{(\mathbf{x}_s - \overline{\mathbf{x}}_s)(\mathbf{x}_s - \overline{\mathbf{x}}_s)'}\sqrt{(\mathbf{x}_t - \overline{\mathbf{x}}_t)(\mathbf{x}_t - \overline{\mathbf{x}}_t)'}} \tag{7.5}$$

which is one minus the sample correlation between objects, where $\overline{\mathbf{x}}_s = (1/n)\sum_j x_{s_j}$ and $\overline{\mathbf{x}}_t = (1/n)\sum_j x_{t_j}$. At last, the Spearman distance,

$$d_{s,t} = 1 - \frac{(r_s - \overline{r}_s)(r_t - \overline{r}_t)'}{\sqrt{(r_s - \overline{r}_s)(r_s - \overline{r}_s)'}\sqrt{(r_t - \overline{r}_t)(r_t - \overline{r}_t)'}} \tag{7.6}$$

which is one minus the sample Spearman rank correlation between observations (treated as sequences of values), where r_{s_i} is the rank of x_{s_i} taken over $x_{1_i}, x_{2_i}, \ldots, x_{m_i}$; r_s and r_t are the coordinate-wise rank vectors of x_s and x_t, i.e., $r_s = (r_{s_1}, r_{s_2}, ..., r_{s_n})$; furthermore, $\overline{r}_s = (1/n)\sum_j r_{s_j} = (n+1)/2$ and $\overline{r}_t = (1/n)\sum_j r_{t_j} = (n+1)/2$.

The *second phase* is the clustering of objects into a binary, hierarchical cluster tree. Objects that are in proximity are linked. As objects are linked into binary (two-object) clusters, the newly generated clusters are grouped into larger clusters until a hierarchical tree is constructed. Different *methods* can be used for calculating linkages [148, pp.3087–3088]. *Single* linkage, also known as nearest neighbor, uses the shortest distance between objects in the two clusters. The maximum distance between objects in the two clusters is used in *complete* linkage, in other terms, the farthest neighbor. *Average* linkage uses the average distance between all pairs of objects in any two clusters. The Euclidean distance between the centroids of the two clusters is used in *centroid* linkage, while the Euclidean distance between the weighted centroids of the two clusters is used in *median* linkage. Further options are, e.g., Ward's linkage and *Weighted average* linkage.

The average linkage Eq. 7.7 method is used in the current chapter, which can be expressed for S source- and T target clusters as:

$$D_{s,t} = \frac{1}{n_S n_T} \sum_{i=1}^{n_S} \sum_{j=1}^{n_T} d(x_{S_i}, x_{T_j}) \tag{7.7}$$

where x_{S_i} is the i-th object in the source cluster, S, having a total number of included objects n_S; similarly, x_{T_j} is the j-th object in the target cluster T with n_T included objects. Note how any metrics from the *first step* Eq. 7.1–7.6 can be used in the operator $d(\cdot,\cdot)$. At each stage of hierarchical clustering, the clusters S and T, for which $D_{S,T}$ is the minimum, are combined.

In summary, given the objects, $\mathbf{x}_k$, the pair-wise differences, $\mathbf{d}$, are calculated by metrics Eq. 7.1–7.6, and the average linkage method Eq. 7.7 yielding $\mathbf{D}$ constitutes the clustering. In the followings, an optimal threshold for $\mathbf{D}$ is sought.

The following notations are worth to highlight here. Let $P := \{c_p\}$ the set of c_p, since C is reserved for *collectives.* Thus, $M \times P$ parameter space describes the M metric types and P set of various thresholds, c_p.

7.2.3 The distribution of distances

Given a c_D threshold as in Fig. 7.2, the clustering is complete, i.e., a cluster identification number is ordered to each sample DFT profile. The empirical cumulative distribution functions of distances $p(\mathbf{D})$ are obtained in each metric type, as in Fig. 7.3. The panes show that kernel cumulative distribution functions are close to the empirical distributions. The cut-off values for probabilities $c_p = \{k \cdot 0.10\}\}$ for $k = 1, 2, \ldots, 9$ are available in the ECDF values vertically, from which the c_D cut-offs for distances can be obtained on the horizontal axis. Whenever $p(\mathbf{D}) \neq c_p$, inverse linear interpolation helps to obtain c_D.

7.2.4 A benefit-to-cost ratio

There are many proposed methodology for defining a threshold on dendrograms; nevertheless, the lack of a golden rule does not ease the circumstances. However, it is hypothesized that the following are often aimed at (a) *as many clustered elements as possible*, beneath (b) *as low spread within clusters as possible.*

To characterize the *variability* within collectives, C_k, among its elements, x_i, over the frequency domain, f, the following measure is used:

$$v_k = \sum_{i=1}^{n_k} \sqrt{\sum_{f=1}^{F} (x_{i,f}, \overline{x}_{i,f})^2}, \tag{7.8}$$

$\overline{x}_{i,f}$ being the average DFT profile in the i-th cluster. Thus, the square root of the squared deviations between cluster elements $\mathbf{x}$ and cluster mean $\overline{\mathbf{x}}$ is summed into one number v_k in the k-th collective cluster. However, it might be favorable to represent this error from many clusters in a single measure characterizing an $\{m, p\}$ setting. Therefore,

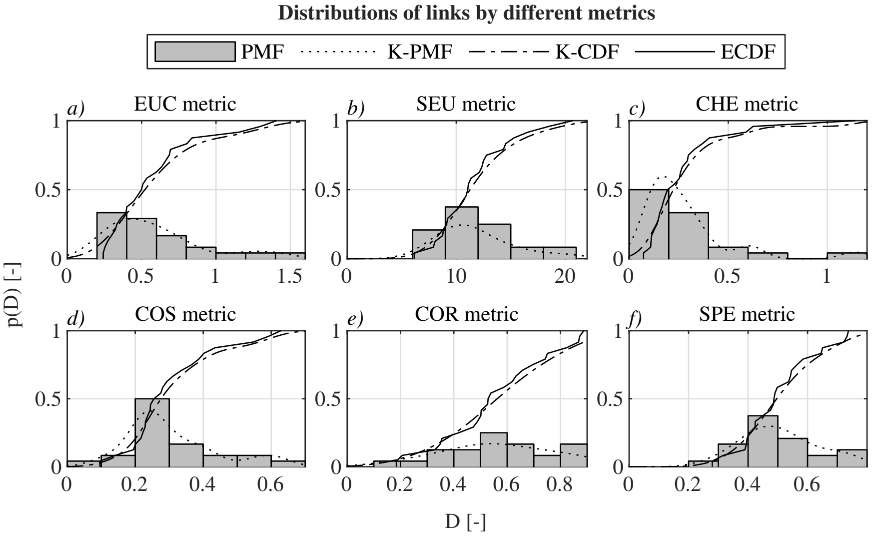

Figure 7.3: Empirical probability mass function (EPMF) along with Kernel-PMF and Kernel cumulative distribution function (KCDF) shows that the ECDF (later referred to as $p(\mathbf{D})$) and the theoretical KCDF are in close proximity for distances obtained by metrics: *a)* Euclidean-; *b)* standardized Euclidean-; *c)* Chebyshev-; *d)* cosine-; *e)* correlation- and *f)* Spearman distances. Note that the Kernel distributions do not utilize positive support.

the center of mass for one setting is defined as

$$G_{m,p} = \frac{\sum_{k=1}^{N_C(m,p)} v_{(m,p)_k} n_{(m,p)_k}}{\sum_{k=1}^{N_C(m,p)} v_{(m,p)_k}}, \tag{7.9}$$

in short $\mathbf{G_k} = \sum \mathbf{v_k n_k} / \sum \mathbf{v_k}$. A possible representation of a *benefit-to-cost ratio* approach is implemented, such as the more objects are clustered, the more *benefits* are provided as of condition (a), and the higher error term is provided by an $\{m, p\}$ setting, the higher *costs* are to be paid in line with condition (b); together defined such as:

$$R_{m,p} = \frac{N_{\Sigma_{m,p}}}{G_{m,p}} \tag{7.10}$$

equivalently $\mathbf{R} = \mathbf{N}/\mathbf{G}$, shown in Fig 7.4.*d)*, which offers the optimum at its maximum in the $M \times P$ parameter space of clustering.

The following section presents the clustering of the above given random sample and Section 7.4 investigates the approach by repeating the procedure 100 times per different sample size.

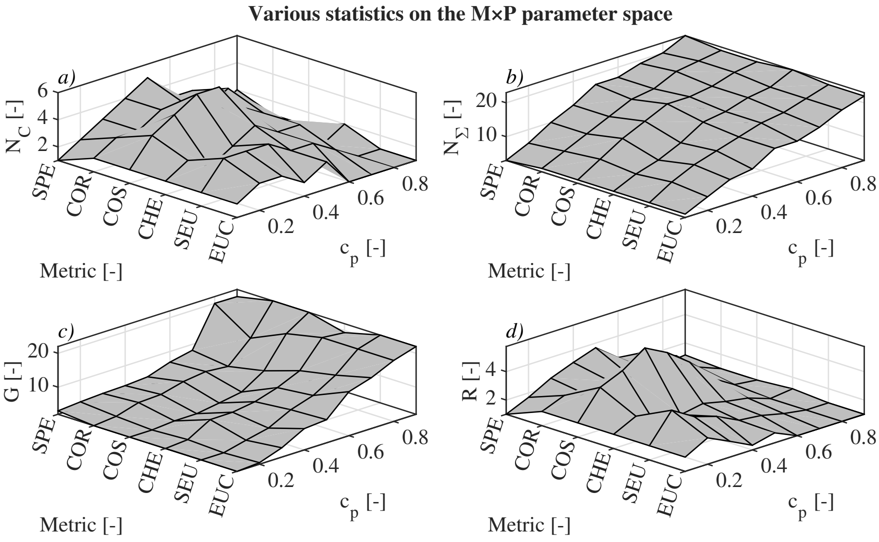

Figure 7.4: Evaluations in the $M \times P$ parameter space, where M indicates metrics and P denotes the set of $\{c_p\}$ thresholds. Results from $\{m, p\}$ settings: *a)* the number of collectives, N; *b)* the number of clustered objects, $N_{\Sigma_{m,p}}$; *c)* the center of mass, $\mathbf{G}$; and *d)* benefit-to-cost ratio, $\mathbf{R}$.

7.3 Results

Fig. 7.4 presents the outcomes from clustering setups collocated by the distance metrics, m, and cut-off probabilities, c_p, for 25 randomly selected vectors from Fig. 7.1. Beginning by Fig. 7.4.*a)*, it shows that the number of clusters at low and high c_p settings is likely to be minor, while middle regions of c_p are likely to produce a maximum in N_C. This is expected since a low c_D might cut all leaves, yielding only a few multi-element clusters. Conversely, a high c_D might also surpass the largest distance in a dendrogram, generating one group comprising every branch. Pane *b)* supports the above observations since an increase in c_p, consequently in c_D, yielded an increasing number of clustered objects in $N_{\Sigma_{m,p}}$ regardless of the type of metric. Pane *c)* depicts a non-linear proportionality between the center of mass $\mathbf{G}$ in clustering settings $\{m, p\}$ as of c_p ; however, it also shows a promising *dale* in the middle regions, especially at the correlation and cosine metrics leading to the suggestion in pane *d)*. That is, benefiting from the number of clustered objects $N_{\Sigma_{m,p}}$ but at the cost of within-cluster-variability, v_k, the benefit-to-cost ratio, $\mathbf{R}$, expresses the optimum at its maxima, which in the above-given sample lead to $m^* = \text{COS}$ at $c_p^* = 0.40$, which meant $c_D^* = 0.24$ here.

Fig. 7.5 shows the dendrogram of the first sample using m^* and c_p^* yielding a seemingly sensitive clustering as a function of c_D since distances are dense around the threshold c_D^*. Fig. 7.6 shows each cluster with its objects and the mean of objects in the frequency domain, producing a qualitatively nice well-alignment in C_k, for $k = 3, 4, 6, 12, 14$. The last cluster, C_{15}, is seemingly more spread in-between. Finally, Fig. 7.7 shows that the means from multi-element clusters tend to be separated from

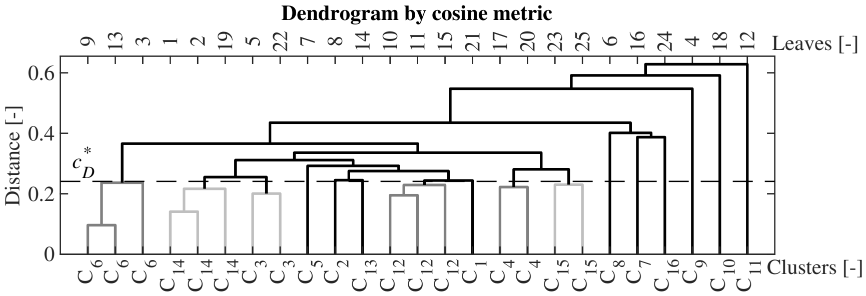

Figure 7.5: Dendrogram by cosine metric, where alteration of lighter and darker *gray* colors shows different clusters, *black* denoting lone objects below c_D optimal cut value

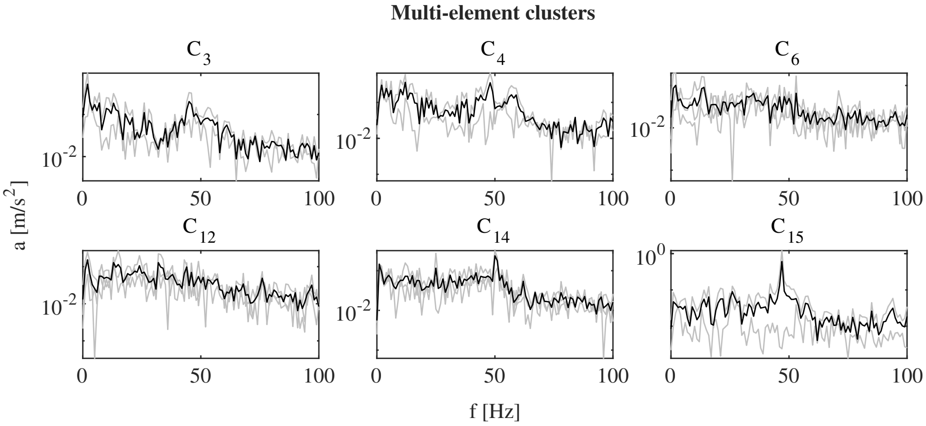

Figure 7.6: Results of clustering in the frequency domain by cosine distance metric at optimum c_D^*, objects denoted by *gray* and their mean by *black*.

singletons.

7.4 Replications

The procedure was repeated 100 times utilizing random samples of sizes $S_S = \{25, 50, 75, 100\}$. The $M \times P$ parameter space had been evaluated in each random sample. Fig. 7.8 *left column* depicts that an optimum metric based on BCM maxima is foremost likely the be the cosine-, second-most the correlation distance metrics. It also shows in

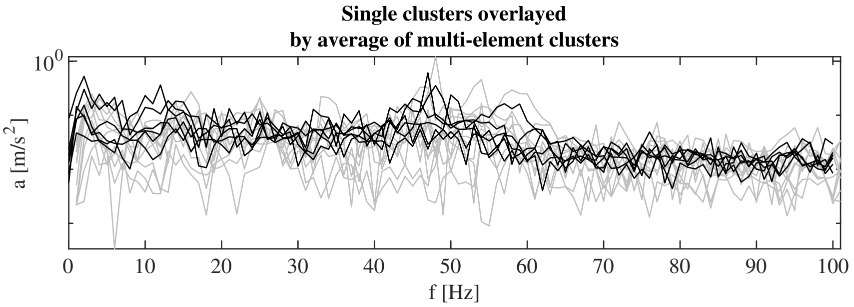

Figure 7.7: Sample clustering yielded a few lone leaves (*gray*), which are overlaid by the mean of multi-element clusters (*black*)

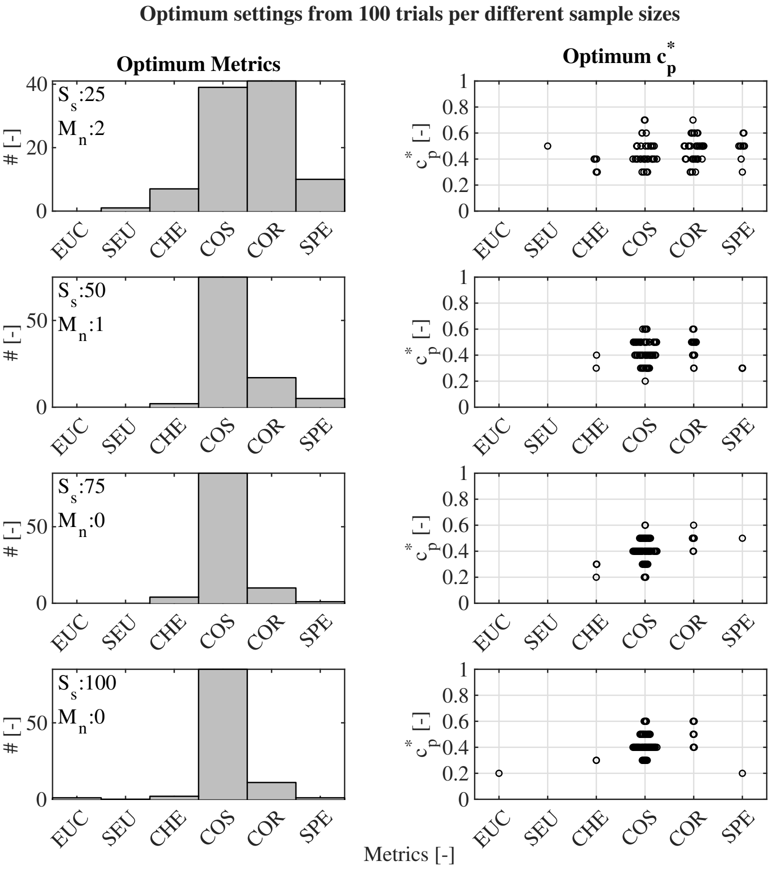

Figure 7.8: The optimum choice on the metric (*left column*) and corresponding swarmchart of optimum cut-off for probability (*right column*). Each row represents 100 trials, according to S_S sample sizes. Md denotes the cases where different simultaneous optima had been found in a trial.

the *right column* that c_p^* is most often around 0.40–0.50, whereas c_D^* is not of particular interest. The left column also reports cases where multiple optima, M_n, were found in a trial. The benefit-to-cost ratio surfaces, **R**, tended to have typically one global maximum, which eases the choice by current methodology.

7.5 Discussion

Hennig argues that "*indices used for finding an optimal number of clusters by optimization should not systematically prefer lower or higher numbers of clusters*" [141]. However, considering the number of clustered objects, it is believed that the presented approach should avoid such a conflict. Though the long-maintained interest in clustering has led to "*a possibly three-digit number of algorithms*" [149], the current procedure can be beneficial in the spectral clustering of DFT vectors obtained in RVV. Finally, it is noted that the above investigation could be extended to different linkage *methods*, as well.

The idea of clustering can be imagined in a completely different use case. The clustering may be applied to the whole series of DFT vectors, e.g., the STFT itself in Fig. 7.1.*a)* given a choice of metric and either an omnibus threshold or a procedure to arrive at optimum c_D^*. Now, if the series of leaves in a dendrogram (see upper horizontal axis in Fig. 7.5) is constrained to the original appearance in time, the dendrogram may not present an easily readable structure. However, apart from aesthetics, the similarity of neighboring DFT vectors could be evaluated. In this idea, it might be rightly supposed that some of the consecutive DFT vectors get into the same cluster, while borders of consecutive clusters are also to be found. The consecutive leaves being in the same cluster would yield a coherent segment in-between but different from neighboring segments, which procedure would mean a novel segmentation.

It is argued in this chapter that the next advantageous step following the segmentation of the time-frequency domain can be the quantification of similarity among segments. The clustering of representative DFT vectors could be accompanied by the collection of exogenous data in order to relate such a segmentation (via clustering). For instance, road profile surveys, internal and external dash-cam recordings could be used to identify the scenarios contributing to the clusters.

7.6 Conclusion

The current chapter presented a validation criterion for clustering road vehicle vibrations spectrums in an automatable procedure. The choice of a threshold for distances, c_D, in a dendrogram has been investigated by thresholds on the empirical cumulative distribution probabilities of distances, c_p, allowing the unified treatment of distance metrics. In hierarchical clustering, a benefit-to-cost ratio surface, $R_{m,p}$, can be defined as a function of metric types, m and cut-offs, c_p. The scheme was repeated in 100 replications as of the four random samples, consisting of $\{25, 50, 75, 100\}$ elements. It showed that the cosine distance metric is the most likely *optimum metric*. However, the corresponding *optimum thresholds* for ECDF produced a wide range, primarily found in the middle regions. In fact, c_p has a secondary interest in the current demonstration since a finer resolution of P can yield a more consequent estimate.

Thesis 6. In binary hierarchical clustering of amplitude spectrum of road-induced vibrations, most likely the cosine distance maximizes the number of clustered elements and minimizes the scattering in-between clusters. ■ *Ref.*: [2]

Chapter 8

Summary

The Introduction excerpted the bibliographic sample analyses [1, 3] leading to the motivation of the current dissertation, summarized in a Proposition.

Proposition. Based on the heterogeneous research topics of road vehicle vibration studies, the lifetime of installed vehicle components and their design to take on loads from amplitude- and frequency modulated excitation, as well as, the avoidance of aversion in passenger comfort, and the vibration protection of transported loads are central research subjects. Instead of studying the individual subsystems of the road–vehicle–cargo system, it can be imperative to establish a standardized methodology, since the final source of excitation is itself the road-induced vibration. ■ *Ref.*: [1, 3]

Non-stationary simulations gained increasing attention, not only in Packaging vibration testing (PVT) but in disciplines concerned with the analysis and synthesis of Road vehicle vibrations (RVV). The limitations of Power spectral density (PSD) based simulations have inherent contrast to real-world RVV. That is, relying on a single PSD, or Discrete Fourier transform (DFT) profile, substantively assumes the stationarity of process; hence, the inverse Fourier transformation can produce only stationary signals, when joint with a uniformly distributed random phase series. This deviation is illustrated in Fig. 8.1, where the lack of transients in the synthesized signal is to be noted. In effect, if a dynamic system has to be designed for taking on transient loads, the adequacy of stationary simulations is seriously limited either as verification in the modeling phase, or as validation in the post-design or pre-release phases.

The dissertation presented various occasions that the spectral content of RVV is far from an autonomous process, far from being avoid of changes. It is therefore rightly to assume non-stationarity in the time-frequency domain structure of RVV, as well. The Chapter, Spectral non-stationarity, has presented that the STFT of measured RVV show up varying spectral characteristic, i.e., the DFT profiles and its spectral moments are non-stationarity over time, allowing the 1st thesis [4]. The example of Fig. 8.2 is a good depiction of drive-train related frequency modulations, furthermore, significant difference in spectral structure at stops, or increased noise levels at various subsections.

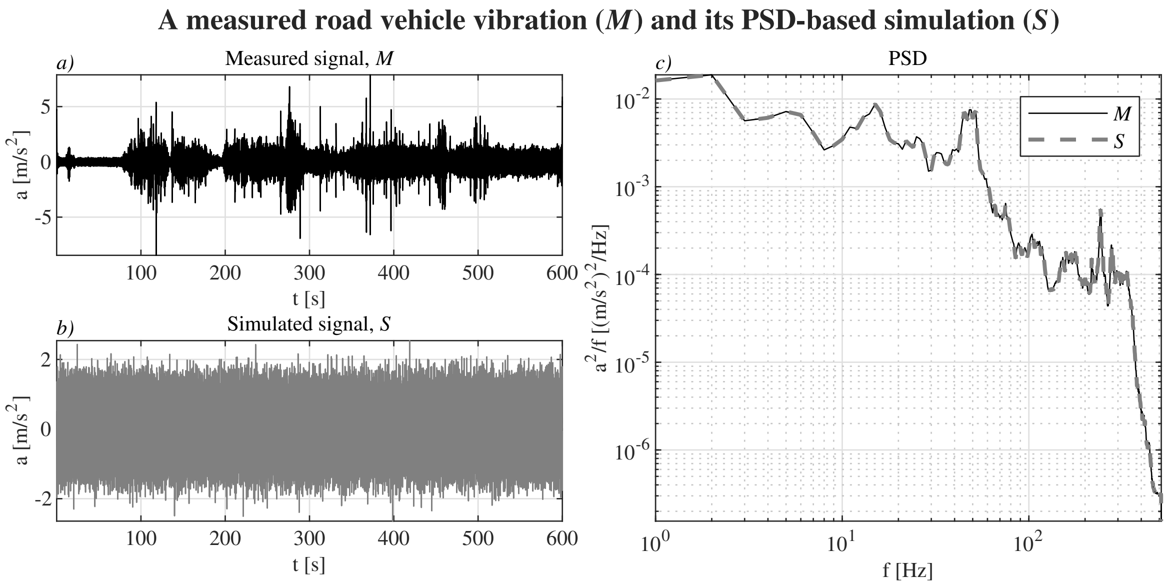

Figure 8.1: Comparison of real-world RVV with its PSD-based simulation. Pane *a)* shows the first 10 min of measurement A from Chapter, Spectral non-stationarity, and its Power spectral density in pane *c)* via *black solid* line. The PSD of the measured signal, M, had been used to simulate a random signal with uniformly distributed random phase in each iteration of the inverse Fourier transform, for 600 s in total. The resulted synthesized signal, S, can be seen in pane *b)* in the time domain, and its re-computed PSD in pane *c)* via *gray dashed* line. The overlap of the two PSD profiles are to be noted, only the PSD of the simulated signal resulted a 28-order smaller difference in the last bin.

Thesis 1. I have presented that the shape of amplitude spectrum function is not constant over time, due to the variation of the spectral shape manifested in the time-frequency domain, which is due to transient events, and harmonic excitation in accordance with the driving speed, compared to the spectral shapes of the steady-state vibration intervals. The changes, therefore, occur locally on the time or space horizon of the journeys, thus, for practical reasons it is reasonable to separate them into homogeneous intervals. ■ *Ref.*: [4]

The time domain of RVV has been thoroughly investigated by scholars, as the author had reviewed those methods in [5]. In order to find homogeneous sections within RVV recordings, various changepoint- or event-detection algorithms have been published. The Chapter, Analysis of prior algorithms, has analyzed the steps of available processes since only a few insights under the hood of such algorithms are provided. As it has turned out, the reproducibility can be easily challenged in most of the cases.

Thesis 2. I have observed that previous segmentation algorithms have been uncalibrated and designed along heuristic considerations in several cases. Calibration of detection algorithms is essential when investigating road-induced vibrations. For verification purposes, the segment length distribution should be investigated on a test sample, as a necessary complementary investigation beneath the receiver operating characteristic. ■ *Ref.*: [5]

The bibliographic sample analyses has shown, that PVT originates in the *measurement and analysis* of RVV, which soon expanded its scope to *simulations* [3], foreshadowing the aims of current work embracing the 5th Thesis. The merit of a second kind has also challenged a preconception. That is, the investigations had been pre-dominantly limited to the time domain, whereby spectral non-stationarities are, at the best, only mentioned. Therefore, it had to presented how the STFT structure are inherently responsible for time domain non-stationarities. The novel algorithms have been developed in Chapter, Development of segmentation, such as the Multiple hypothesis testing by paired t-tests as published in [6]:

$$\begin{cases} H_0^{(j)} : \overline{d_j} = 0; \\ H_A^{(j)} : \overline{d_j} \neq 0, \end{cases}$$

where $d_j = a_i - a_{i+1}$, with a_i denoting the DFT coefficients in the i-th timepoint of the STFT. By two-sample t-tests, published in [7]:

$$\begin{cases} H_0^{(j)} : \overline{a}_{i,k} = \overline{a}_{i,k+1}; \\ H_A^{(j)} : \overline{a}_{i,k} \neq \overline{a}_{i,k+1}. \end{cases}$$

where $a_{i,k}$ denotes the DFT coefficients in the i-th timepoint of the STFT through k frequency components.

Thesis 3. The surface formed by short-time Fourier amplitude spectrum can be segmented in the time-frequency domain due to the temporal variation of the inherited spectral shape. This can be done by applying paired-sample- and two-sample t-tests to the Fourier coefficients of adjacent-to-adjacent amplitude spectra. ■ *Ref.*: [6, 7]

The spectral non-stationarity has been also supported by a conventional method applied in a novel context, as discussed in the Section, CUSUM-type changepoint detection [9]. While the algorithm needed custom implementation in lack of command-line availability, the novel characterization of the STFT plane in the forms of spectral moments was also necessary. The Chapter, Calibration of segmentations, has presented that the Segment length distributions are a necessary company to Receiver operating characteristics in the verification, leading to the next thesis [8].

Thesis 4. I have shown that there exists a significance level and it can be determined for so-called *CUSUM* recursive algorithms—which algorithm searches for the local extrema of the cumulative sum of deviations from the total mean—which significance level minimizes the difference between the theoretical distribution of the segment lengths of the test signal and the segment length distribution between the detected boundary points. ■ *Ref.*: [8, 9]

While in Multiple hypothesis testing, the adjustment of significance limit is often advised; it has been shown, the Bonferroni- and Holm–Bonferroni correction are too strict in the long term for RVV segmentation purposes.

The developed changepoint detections could have been used on the sole reason of segmentation as the basis of further quantitative analyses. It has been shown, that the segment length- and RMS distributions did not allow to assume a bi-uniform joint distribution. That is, not any RMS content can be imagined on arbitrary lengths. Therefore, the simulation of non-stationary RVV followed the segmentation.

Each of the prior three segmentation methods can be used in a modular manner during the simulation, Probability-based Spectrogram Synthesis (PBSS). For an eased acceptability, the conventional CUSUM algorithm had been inherited [10]. Its further advantages also emanates from the joint probability distribution of segment lengths and -RMS. That is, every new *segment-in-simulation* has a length and RMS target value according to random variables. The key idea in the synthesis of segments excavated that the amplitude spectrum values in each frequency bin can be fitted with individual distributions from the *segment-to-simulate*. That is, the synthesis is directly accomplished in the time-frequency domain. Such a simulated signal is presented in Fig. 8.3.

Thesis 5. A simulation routine can be constructed that can reflect spectral variations in the time-frequency domain in a realistic manner; which simulates an arbitrary number of different time-frequency domains from a single measurement realization; furthermore, which simulates aggregate statistical properties of the registered road vehicle vibrations.

Verifying this claim, I have presented the *Probability-based Spectrogram Synthesis* procedure for simulating the 2^{nd}, 3^{rd}, and 4^{th} spectral moments. Practical implications of the thesis are:

5.1 Changepoints in the time-frequency domain can found simultaneously for transient events, changes in the root mean square of the signal, and the appearance of harmonic excitations in the road vehicle vibration signals.

5.2 Methods relying on magnitude modulation bypass the need for *a priori* and heuristic adjustment of many parameters.

5.3 Road vehicle vibrations can be directly simulated in the time-frequency domain.

5.4 Modeling and simulation based on measured data outperforms in variability the time-history replication method. ■ *Ref.*: [10]

It allows not only to achieve random segment length and -RMS pairs, but the modeling of STFT values are simulated in *each second of each segment of each simulation.* Therefore, given only one realization of RVV measurement, arbitrary number of different artificial RVV can be obtained. Furthermore, given numerous RVV measurements, their pooled sampling is applicable.

Not only a simulation could follow the segmentation. In the author's opinion, the composition of databases storing DFT characteristics will be sooner or later necessary. In this problem, however, it can be rightly supposed that the similarity of spectral profiles has to be investigated. In this manner, the hierarchical clustering of DFT profiles in the STFT had been investigated in the Chapter, Clustering spectrums. While this is based on a simplistic idea, no spectral clustering has appeared in the concerned discipline of PVT [2].

Thesis 6. In binary hierarchical clustering of amplitude spectrum of road-induced vibrations, most likely the cosine distance maximizes the number of clustered elements and minimizes the scattering in-between clusters. ■ *Ref.*: [2]

As final thoughts, the current dissertation presented, how non-stationarity in RVV can be approached from the time-frequency domain. The changes in spectral characteristics can be found by the new algorithms. Furthermore, the presented simulation, PBSS, allows the non-stationary STFT simulations. With the above theses and corresponding methods, the practitioners have new tools to investigate dynamic systems subjected to road-induced vibrations.

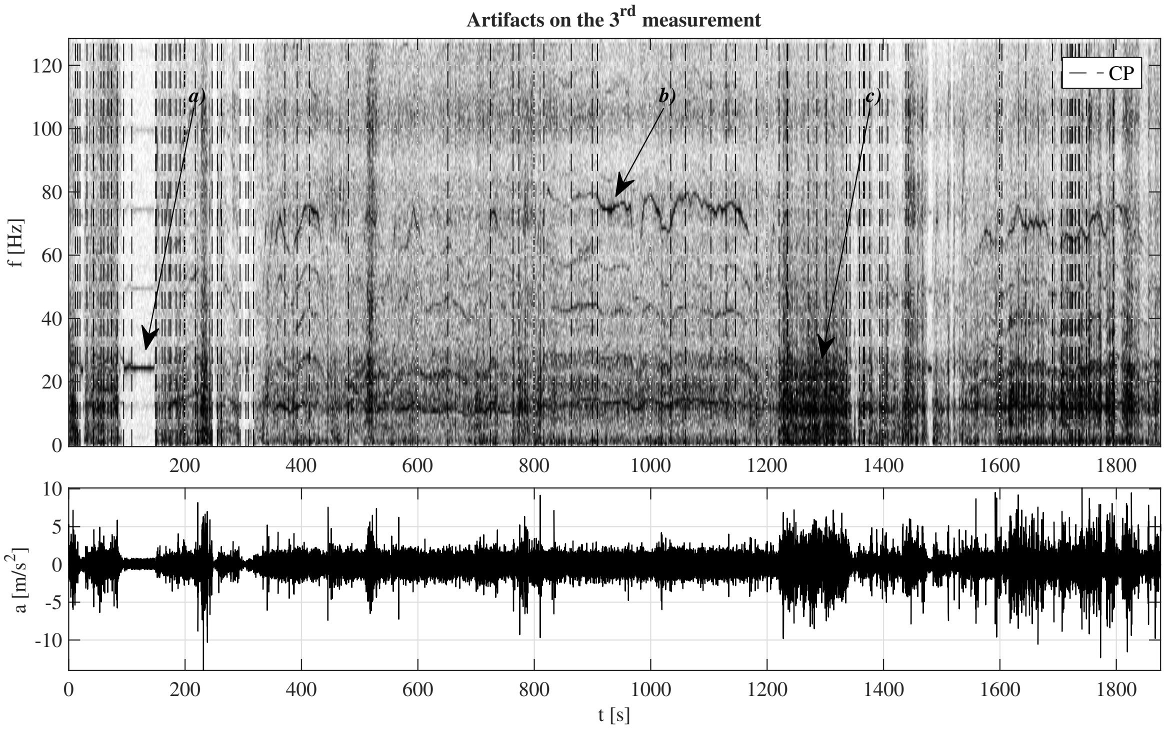

Figure 8.2: Artifacts on the short-time Fourier transform of the 3^{rd} measurement. The gray-scale surface is overlayed by segment borders (*dashed line*) in the upper pane. Various effects can be seen in the spectrogram, such as *a)* constant harmonic excitation and its harmonics, possible one sub-harmonic; *b)* drifting harmonic excitation; *c)* broadband excitation for a prolonged period dominated by frequency range app. $[1, 50]$ Hz between $[1220, 1320]$ s.

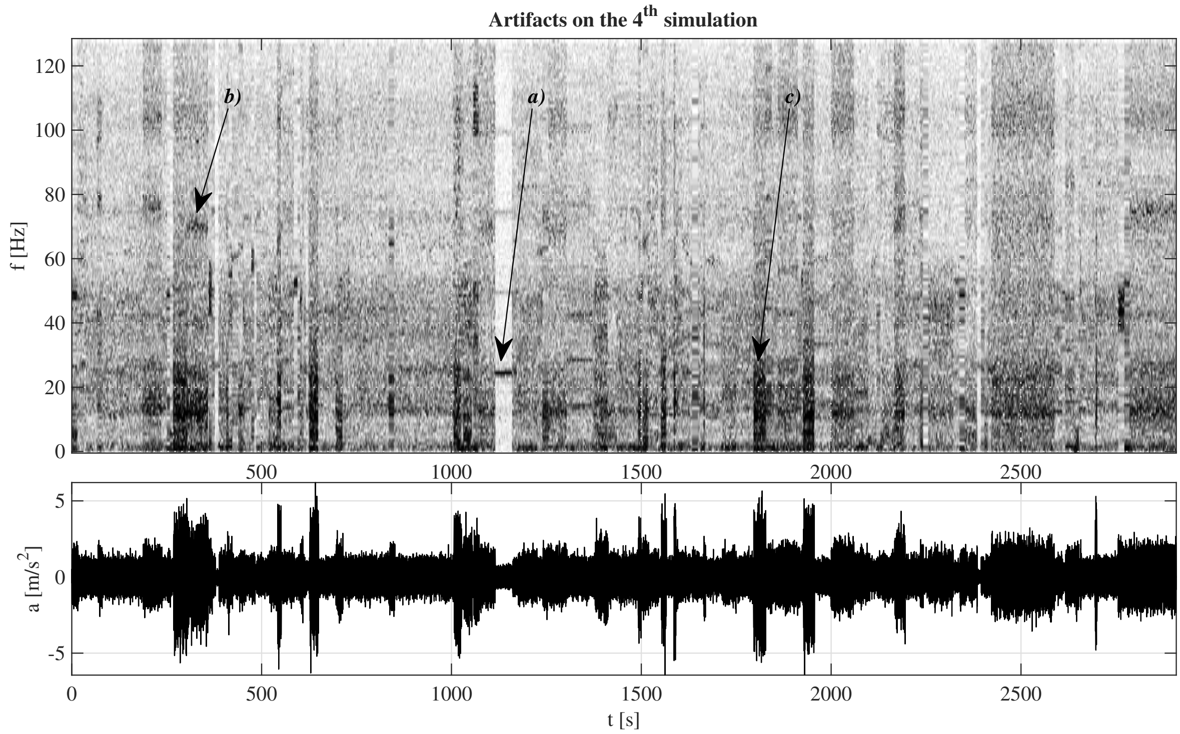

Figure 8.3: Artifacts on the short-time Fourier transform of the 4th simulation. In the upper pane: *a)* simulated stop, i.e., constant harmonic excitation with harmonics, *b)* harmonic component with possible sub-harmoninics blended in background noise, *c)* broad-band noise.

Appendix A

Theses

A.1 Theses in English

Proposition. Based on the heterogeneous research topics of road vehicle vibration studies, the lifetime of installed vehicle components and their design to take on loads from amplitude- and frequency modulated excitation, as well as, the avoidance of aversion in passenger comfort, and the vibration protection of transported loads are central research subjects. Instead of studying the individual subsystems of the road–vehicle–cargo system, it can be imperative to establish a standardized methodology, since the final source of excitation is itself the road-induced vibration. ■ *Ref.*: [1, 3]

Thesis 1. I have presented that the shape of amplitude spectrum function is not constant over time, due to the variation of the spectral shape manifested in the time-frequency domain, which is due to transient events, and harmonic excitation in accordance with the driving speed, compared to the spectral shapes of the steady-state vibration intervals. The changes, therefore, occur locally on the time or space horizon of the journeys, thus, for practical reasons it is reasonable to separate them into homogeneous intervals. ■ *Ref.*: [4]

Thesis 2. I have observed that previous segmentation algorithms have been uncalibrated and designed along heuristic considerations in several cases. Calibration of detection algorithms is essential when investigating road-induced vibrations. For verification purposes, the segment length distribution should be investigated on a test sample, as a necessary complementary investigation beneath the receiver operating characteristic. ■ *Ref.*: [5]

Thesis 3. The surface formed by short-time Fourier amplitude spectrum can be segmented in the time-frequency domain due to the temporal variation of the inherited spectral shape. This can be done by applying paired-sample- and two-sample t-tests to the Fourier coefficients of adjacent-to-adjacent amplitude spectra. ■ *Ref.*: [6, 7]

Thesis 4. I have shown that there exists a significance level and it can be determined for so-called *CUSUM* recursive algorithms—which algorithm searches for the local extrema of the cumulative sum of deviations from the total mean—which significance level minimizes the difference between the theoretical distribution of the segment lengths of the test signal and the segment length distribution between the detected boundary points. ■ *Ref.*: [8, 9]

Thesis 5. A simulation routine can be constructed that can reflect spectral variations in the time-frequency domain in a realistic manner; which simulates an arbitrary number of different time-frequency domains from a single measurement realization; furthermore, which simulates aggregate statistical properties of the registered road vehicle vibrations. Verifying this claim, I have presented the *Probability-based Spectrogram Synthesis* procedure for simulating the 2nd, 3rd, and 4th spectral moments. Practical implications of the thesis are:

5.1 Changepoints in the time-frequency domain can found simultaneously for transient events, changes in the root mean square of the signal, and the appearance of harmonic excitations in the road vehicle vibration signals.

5.2 Methods relying on magnitude modulation bypass the need for *a priori* and heuristic adjustment of many parameters.

5.3 Road vehicle vibrations can be directly simulated in the time-frequency domain.

5.4 Modeling and simulation based on measured data outperforms in variability the time-history replication method. ■ *Ref.*: [10]

Thesis 6. In binary hierarchical clustering of amplitude spectrum of road-induced vibrations, most likely the cosine distance maximizes the number of clustered elements and minimizes the scattering in-between clusters. ■ *Ref.*: [2]

A.2 Theses in Hungarian

Feltevés Az útgerjesztéssel foglalkozó tanulmányok heterogén kutatási tárgyai alapján, főként a beépített járműalkatrészek élettartama és azok amplitúdó- és frekvenciamodulált gerjesztésekre történő méretezése, továbbá az utaskomfortérzet averzív befolyásoltságának elkerülése, valamint a szállított rakományok rezgésvédelme a kutatások központi tárgyai. A pálya–jármű–rakomány egyes alrendszereinek tanulmányozása helyett célravezető az egységesített módszertan létrehozása, tekintve, hogy ugyanaz a gerjesztés végső forrása maga az útgerjesztés. ■ *Ref.*: [1, 3]

1. Tézis Bemutattam, hogy az amplitúdóspektrum alakja időben nem állandó, az idő-frekvencia tartományban lezajló spektrális változás okán, amely a tranziens események és a menetsebességben bekövetkező és azzal összfüggésben jelentkező harmonikus gerjesztések hatására jön létre, összevetve az állandósult rezgésű szakaszok spektrális alakjaival. A változások ennélfogva lokálisan jelentkeznek az utazások idő- vagy térhorizontján, így praktikus szempontokból ezek szeparációja homogén intervallumokra indokolt. ■ *Ref.*: [4]

2. Tézis Megfigyeltem, hogy a korábbi szegmentálási algoritmusok heurisztikus megfontolások mentén, több esetben kalibrálatlanul publikáltak. Az algoritmusok kalibrációja elengedhetetlen a detektálási feladatokban az útgerjesztés vizsgálata során. Verifikációs célból, próbamintán tesztelhető a szegmenshossz eloszlás, amely a detektor jelleggörbéjének szükségszerű kiegészítő vizsgálata. ■ *Ref.*: [5]

3. Tézis A rövid-idejű amplitúdóspektrumokból kialakított felület az idő-frekvencia tartományban szegmentálható a spektrális alak időbeni változásának okán. Erre alkalmasak a páros mintás- és kétmintás t-tesztek a szomszédos amplitúdóspektrumok Fourier-együtthatóira alkalmazva, amelyeket két-, majd egy-másodperces időbeni felbontás esetén mutattam be. ■ *Ref.*: [6, 7]

4. Tézis Bemutattam, hogy létezik és meghatározható olyan szignifikancia-szint, az átlagtól vett eltérések kumulatív összegsorának lokális szélsőértékeit keresvő ún. *CUSUM* rekurzív algoritmusok esetén, amely szignifikancia-szint minimalizálja tesztjelbeni szegmenshossz elméleti eloszlása és a detektált határoló pontok közötti szegmenshossz-eloszlás közötti különbséget. ■ *Ref.*: [8, 9]

5. Tézis Konstruálható olyan szimulációs rutin, mely az idő-frekvencia tartományban spektrális változások valósághközeli tükrözésére képes; amely rutin egy mérési realizáció esetén tetszőleges számú különböző idő-frekvencia tartományt szimulál; továbbá, amely rutin tetszőleges számú mérési realizáció esetén a regisztrátumok aggregált statisztikai vonatkozásait szimulálni képes. Az állítás igazolására a 2., 3., és 4. spektrális nyomatékokat szimuláló eljárást mutattam be. A tézis gyakorlati következményei:

5.1 Tranziens események, a jel effektív középértékében bekövetkező változások, továbbá a harmonikus gerjesztések együttesen szegmentálhatók az idő-frekvencia tartományban.

5.2 A magnitúdó modulációra támaszkodó eljárások kikerülik az *a priori* szükségességét és számos paraméter heurisztikus beállítását.

5.3 Az útgerjesztés közvetlenül szimulálható az idő-frekvencia tartományban.

5.4 Mérési adatokra támaszkodó modellezés és szimuláció jellegőből fakadóan előrelépést jelent a jelek direkt visszajátszásához, azaz reprodukálásához képest. ■ *Ref.*: [10]

6. Tézis Az útgerjesztés jelek amplitúdóspektrum-függvényeinek bináris hierarchikus klaszterezése során a legnagyobb valószínűséggel a koszinusz távolságmutató maximálja a klaszterelt elemek számát és minimálja a klaszterek szóródását. ■ *Ref.*: [2]

Bibliography

[1] László Róbert Hári. “Keyword Co-occurrence Analysis of a Packaging Vibration Testing Relevant Sample”. In: *16th International Bata Conference for Ph.D. Students and Young Researchers*. Vol. 16. Zlín, Czech Republic: Tomas Bata University, 2020, pp. 187–201. ISBN: ISBN: 978-80-7454-935-9. DOI: https://doi.org/10.7441/dokbat.2020.16.

[2] László Róbert Hári and Péter Földesi. “An Approach for Hierarchical Clustering of Road Vehicle Vibration Spectrums (in print)”. In: Miskolc, Hungary, Sept. 2022.

[3] László Róbert Hári. “Timeline-based Network Analysis of a Publication Sample Related to Packaging Vibration Testing”. In: *Business Logistics in Modern Management*. Osijek, Croatia: Josip Juraj Strossmayer University of Osijek Faculty of Economics in Osijek, Oct. 2020. ISBN: 1849-6148 (Online).

[4] László Róbert Hári. “Spectral Non-Stationarity in Road Vehicle Vibrations (in review)”. In: *Periodica Polytechnica Transportation Engineering* -.- (), pp. –.

[5] László Róbert Hári. “Event Detection Algorithms in Packaging Vibration Testing: An Analytic Review”. In: *Business Logistics in Modern Management*. Osijek, Croatia: Josip Juraj Strossmayer University of Osijek Faculty of Economics in Osijek, Oct. 2021, pp. 453–472. ISBN: 1849-6148 (Online).

[6] László Róbert Hári. “Multiple Hypothesis Testing by Unpaired Samples for Indexing Changepoints in a Road-induced Vibration Signal”. In: *University Politehnica of Bucharest - Scientific Bulletin*. Series D 83.3 (2021), pp. 17–28. ISSN: 1454-2358.

[7] László Róbert Hári. “Segmentation of a Road Vehicle Vibration Signal Using Multiple Comparison Procedures between Paired Samples”. In: *Tehnicki Vjesnik - Technical Gazette* 28.5 (Oct. 2021). ISSN: 13303651, 18486339. DOI: 10.17559/TV-20200122112551. URL: https://hrcak.srce.hr/261336 (visited on 01/03/2022).

[8] László Róbert Hári and Péter Földesi. “Calibration of Two Novel Segmentation Approaches by Synthetic Road Vehicle Vibrations (in review)”. In: *Tehnicki Vjesnik - Technical Gazette* -.- (), pp. –.

[9] László Róbert Hári and Péter Földesi. “Evaluation of a CUSUM-type Change-point Detector Applied in the Time-Frequency Domain of Synthetic Road Vehicle Vibrations (in Print)”. In: Miskolc, Hungary, Sept. 2022.

[10] László Róbert Hári. “Spectral Moment Segmentation and Spectrogram Synthesis for Simulation of Road Vehicle Vibrations”. en. In: *Mechanical Systems and Signal Processing* 180 (Nov. 2022), p. 109408. ISSN: 08883270. DOI: 10.1016/j.ymssp.2022.109408. URL: https://linkinghub.elsevier.com/retrieve/pii/S0888327022005350.

[11] Julius S. Bendat and Allan G. Piersol. *Random Data: Analysis and Measurement Procedures.* en. 4th ed. Wiley series in probability and statistics. Hoboken, N.J: Wiley, 2010. ISBN: 978-0-470-24877-5.

[12] Jens Ahrens et al. “Tutorial on Scaling of the Discrete Fourier Transform and the Implied Physical Units of the Spectra of Time-Discrete Signals”. en. In: (2020), p. 5.

[13] G Heinzel, A Rudiger, and R Schilling. “Spectrum and spectral density estimation by the Discrete Fourier transform (DFT), including a comprehensive list of window functions and some new flat-top windows.” en. In: (2002), p. 84.

[14] Elsevier B.V. *Scopus.* 2020. URL: https://www.scopus.com/.

[15] Nees Jan van Eck and Ludo Waltman. “VOSviewer”. In: (2020). Place: Leiden Publisher: Centre for Science and Technology Studies of Leiden University.

[16] Vladimir Batagelj and Andrej Mrvar. “Pajek”. In: (2020).

[17] *Wolfram Mathematica.* The Wolfram Centre Lower Road, Long Hanborough Oxfordshire OX29 8FD United Kingdom, 2020. URL: https://www.wolfram.com.

[18] Dragan Sekulić et al. “Definition and determination of the bus oscillatory comfort zones”. In: *International Journal of Industrial Ergonomics* 53 (May 2016), pp. 328–339. ISSN: 01698141. DOI: 10.1016/j.ergon.2016.04.003.

[19] S. Peng and J. Song. “Simulation of vehicle ride comfort performance in Adams”. In: *Proceedings of Asian Simulation Conference; System Simulation and Scientific Computing (Shanghai).* Orlando, FL; United States, 2002, Vol 2. 738–742.

[20] Hanyue Zhang and Xueqiong Feng. “Study on Damage Analysis and Random Vibration Detection of Transportation Goods”. In: *Applied Sciences in Graphic Communication and Packaging.* Ed. by Pengfei Zhao et al. Vol. 477. Series Title: Lecture Notes in Electrical Engineering. Singapore: Springer Singapore, 2018, pp. 475–487. ISBN: 978-981-10-7628-2 978-981-10-7629-9. DOI: 10.1007/978-981-10-7629-9_59. URL: http://link.springer.com/10.1007/978-981-10-7629-9_59 (visited on 07/21/2022).

[21] S.Q. Wu et al. “Vibration analysis of a beam on a moving vehicle under the road excitation with different contact models”. In: *Journal of Vibroengineering* 15.4 (2013), pp. 1689–1700.

[22] Yi Chern Hsieh, Minh Hai Doan, and Chen Tai Chang. “Three Dimensional Dynamic Analyses on Stroller Wheel with Shock Absorber”. In: *Applied Mechanics and Materials* 387 (Aug. 2013), pp. 159–163. ISSN: 1662-7482. DOI: 10.4028/www.scientific.net/AMM.387.159.

[23] G. Müller. “Nonlinear simulation of the suspension and steering systems of road vehicles - Multibody dynamics”. In: *Proceedings of the Mini Conference on Vehicle System Dynamics, Identification and Anomalies*. Budapest, 2006, pp. 321–327.

[24] Peter Holdmann and Frank Berger. “Kinematics and Compliance of Sports Utility Vehicles”. In: *SAE 2001 World Congress*. SAE International in United States, Mar. 2001. DOI: 10.4271/2001-01-0491.

[25] V. Rouillard, M.J. Lamb, and Y. Losk. “Developing test schedules for simulating multiaxial vibratory motions of delivery vehicles”. In: *21st IAPRI World Conference on Packaging 2018 - Packaging: Driving a Sustainable Future*. Zhuhai, 2019, pp. 104–111.

[26] Vincent Rouillard and Matthew Lamb. “Some characteristics of the heave, pitch and roll vibrations within urban delivery routes”. In: *Packaging Technology and Science* 33.3 (Mar. 2020), pp. 113–121. ISSN: 0894-3214. DOI: 10.1002/pts.2491.

[27] Zhang Lijun, Si Yang, and Yu Zhuoping. “Elementary Investigation into Road Simulation Experiment of Powertrain and Components of Fuel Cell Passenger Car”. In: *2008 SAE International Powertrains, Fuels and Lubricants Congress*. SAE International in United States, June 2008. DOI: 10.4271/2008-01-1585.

[28] Ali G. Goktan and Argun Yetkin. “Road Load Data Estimation on Multiaxial Test Rigs for Exhaust System Vibrations”. In: *SAE 2002 World Congress & Exhibition*. SAE International in United States, Mar. 2002. DOI: 10.4271/2002-01-0805.

[29] Péter Böröcz and S. Paul Singh. “Measurement and analysis of delivery van vibration levels to simulate package testing for parcel delivery in Hungary”. In: *Packaging Technology and Science* 31.5 (May 2018), pp. 342–352. ISSN: 08943214. DOI: 10.1002/pts.2327.

[30] Muhammad Prasetya Kurniawan et al. “Measurement and Analysis of Vibration Levels in Two and Three Wheel Delivery Vehicles in Southeast Asia”. In: *Packaging Technology and Science* 28.9 (Sept. 2015), pp. 836–850. ISSN: 08943214. DOI: 10.1002/pts.2143.

[31] Behnam Soleimani and Ebrahim Ahmadi. “Measurement and analysis of truck vibration levels as a function of packages locations in truck bed and suspension”. In: *Computers and Electronics in Agriculture* 109 (Nov. 2014), pp. 141–147. ISSN: 01681699. DOI: 10.1016/j.compag.2014.09.009.

[32] Manuel-Alfredo Garcia-Romeu-Martinez, S. Paul Singh, and Vicente-Agustin Cloquell-Ballester. “Measurement and analysis of vibration levels for truck transport in Spain as a function of payload, suspension and speed”. In: *Packaging Technology and Science* 21.8 (Dec. 2008), pp. 439–451. ISSN: 08943214. DOI: 10.1002/pts.798.

[33] Giovani Otavio Rissi et al. “Measurement and analysis of truck transport environment in Brazil”. In: *Packaging Technology and Science* 21.4 (June 2008), pp. 231–246. ISSN: 08943214. DOI: 10.1002/pts.797.

[34] Y. Zeng et al. “Effect of transport vibration in different levels of road on Hamimelons (Cucumis melo var. saccharinus) quality”. In: *Nongye Gongcheng Xuebao/Transactions of the Chinese Society of Agricultural Engineering* 33.9 (2017), pp. 282–289. DOI: 10.11975/j.issn.1002-6819.2017.09.037.

[35] Marc Köntges et al. “Impact of transportation on silicon wafer-based photovoltaic modules”. In: *Progress in Photovoltaics: Research and Applications* 24.8 (Aug. 2016), pp. 1085–1095. ISSN: 10627995. DOI: 10.1002/pip.2768.

[36] Behnam Soleimani and Ebrahim Ahmadi. “Evaluation and analysis of vibration during fruit transport as a function of road conditions, suspension system and travel speeds”. In: *Engineering in Agriculture, Environment and Food* 8.1 (Jan. 2015), pp. 26–32. ISSN: 18818366. DOI: 10.1016/j.eaef.2014.08.002.

[37] Carlos Bernad et al. “Dynamic study of stacked packaging units by operational modal analysis”. In: *Packaging Technology and Science* 23.3 (2010), pp. 121–133. ISSN: 08943214. DOI: 10.1002/pts.883.

[38] Julien Lepine, Vincent Rouillard, and Michael Sek. “Review Paper on Road Vehicle Vibration Simulation for Packaging Testing Purposes”. In: *Packaging Technology and Science* 28.8 (2015). Publisher: John Wiley and Sons Ltd, pp. 672–682. ISSN: 10991522. DOI: 10.1002/pts.2129.

[39] K. Ramji et al. “Dynamic behaviour of railway coach and bogie frame using finite element analysis”. In: *Journal of the Institution of Engineers (India): Mechanical Engineering Division* 87.JAN. (2007), pp. 7–17.

[40] M.T. Turczyn et al. “Testing Frozen Foods for Rail Transport Environment”. In: *Transactions of the American Society of Agricultural Engineers* 27.6 (1984), pp. 1984–1989.

[41] S. Saravanan, M.I. Sakri, and P.V. Mohanram. “Fatigue Prediction of Electronic Packages Subjected to Random Vibrations”. In: *Journal of Microelectronics and Electronic Packaging* 5.1 (Jan. 2008), pp. 31–35. ISSN: 1551-4897. DOI: 10.4071/1551-4897-5.1.31.

[42] Karumbu Meyyappan et al. “Knowledge Based Qualification Process to Evaluate Vibration Induced Failures in Electronic Components”. In: *ASME 2017 International Technical Conference and Exhibition on Packaging and Integration of Electronic and Photonic Microsystems*. American Society of Mechanical Engineers, Aug. 2017. ISBN: 978-0-7918-5809-7. DOI: 10.1115/IPACK2017-74190.

[43] Ki-Soo Kim, Yong Baek, and In Kyoon Yoo. “Pavement roughness monitoring method using fiber optic vibration sensors”. In: *Proceedings Volume 7647, Sensors and Smart Structures Technologies for Civil, Mechanical, and Aerospace Systems 2010*. Ed. by Masayoshi Tomizuka. Mar. 2010, 76472G. DOI: 10.1117/12.848880.

[44] K.-S. Kim et al. “Fiber optic pavement roughness monitoring”. In: *17th World Congress on Intelligent Transport Systems, ITS 2010; Busan Exhibition and Convention Center (BEXCO)Busan;* Busan, 2010.

[45] Mu’ath Al-Tarawneh and Ying Huang. “Glass fiber-reinforced polymer packaged fiber Bragg grating sensors for low-speed weigh-in-motion measurements”. In: *Optical Engineering* 55.8 (Aug. 2016), p. 086107. ISSN: 0091-3286. DOI: 10.1117/1.OE.55.8.086107.

[46] Claudiu Chiculita and Laurentiu Frangu. “A low-cost car vibration acquisition system”. In: *2015 IEEE 21st International Symposium for Design and Technology in Electronic Packaging (SIITME)*. IEEE, Oct. 2015, pp. 281–285. ISBN: 978-1-5090-0332-7. DOI: 10.1109/SIITME.2015.7342341.

[47] Y. Liua, B. Sun, and Q. Feng. “Package reliability of MEMS sensors used in automotive under random vibration”. In: *Chemical Engineering Transactions* 33 (2013), pp. 481–486. DOI: 10.3303/CET1333081.

[48] Vincent Rouillard. “Generating road vibration test schedules from pavement profiles for packaging optimization”. In: *Packaging Technology and Science* 21.8 (Dec. 2008), pp. 501–514. ISSN: 08943214. DOI: 10.1002/pts.840.

[49] Julien Lepine, Vincent Rouillard, and Michael Sek. “Evaluation of machine learning algorithms for detection of road induced shocks buried in vehicle vibration signals”. In: *Proceedings of the Institution of Mechanical Engineers, Part D: Journal of Automobile Engineering* 233.4 (Mar. 2019). Publisher: SAGE Publications Ltd, pp. 935–947. ISSN: 09544070. DOI: 10.1177/0954407018756201.

[50] Julien Lepine, Vincent Rouillard, and Michael Sek. “On the Use of Machine Learning to Detect Shocks in Road Vehicle Vibration Signals”. In: *Packaging Technology and Science* 30.8 (Aug. 2017). Publisher: John Wiley and Sons Ltd, pp. 387–398. ISSN: 10991522. DOI: 10.1002/pts.2202.

[51] Julien Lepine, Vincent Rouillard, and Michael Sek. “Wavelet Transform to Index Road Vehicle Vibration Mixed Mode Signals”. In: *ASME 2015 Noise Control and Acoustics Division Conference*. San Francisco, California, USA: American Society of Mechanical Engineers, Aug. 2015. ISBN: 978-0-7918-5681-9. DOI: 10.1115/NCAD2015-5909.

[52] J. Lepine, V. Rouillard, and M. Sek. “Using the Hilbert-Huang transform to identify harmonics and transients within random signals”. In: *8th Australasian Congress on Applied Mechanics: ACAM 8*. Barton: ACT: Engineers Australia, 2014, pp. 157–166.

[53] Mohammad Fard. “Acoustic Signature for Seat Rattles”. In: *SAE 2011 World Congress & Exhibition*. SAE International in United States, 2011. DOI: 10.4271/2011-01-0504.

[54] Clarivate Analytics. *Web of Science*. 2020. URL: https://apps.webofknowledge.com/.

[55] Nees Jan van Eck and Ludo Waltman. “CitNetExplorer (Leiden University © 2014)”. In: (2014). Place: Leiden, Netherlands Publisher: Leiden Univerity.

[56] De Wouter Nooy, Andrej Mrvar, and Vladimir Batagelj. *Exploratory network analysis with Pajek*. 1st ed. New York: Cambridge University Press, 2005.

[57] Indika Fernando, Jiangang Fei, and Roger Stanley. “Measurement and analysis of vibration and mechanical damage to bananas during long-distance interstate transport by multi-trailer road trains”. en. In: *Postharvest Biology and Technology* 158 (Dec. 2019), p. 110977. ISSN: 09255214. DOI: 10.1016/j.postharvbio.2019.110977. URL: https://linkinghub.elsevier.com/retrieve/pii/S0925521419301103 (visited on 01/17/2021).

[58] Indika Fernando et al. “Measurement and evaluation of the effect of vibration on fruits in transit-Review”. en. In: *Packaging Technology and Science* 31.11 (Nov. 2018), pp. 723–738. ISSN: 08943214. DOI: 10.1002/pts.2409. URL: http://doi.wiley.com/10.1002/pts.2409 (visited on 01/17/2021).

[59] Fei Lu et al. “Analysis of shock and vibration in truck transport in Japan”. In: *Packaging Technology and Science* 21.8 (Dec. 2008). Publisher: Wiley, pp. 479–489. ISSN: 0894-3214. DOI: 10.1002/pts.841.

[60] S P Singh et al. “Measurement and analysis of truck and rail shipping environment in India”. In: *Packaging Technology and Science* 20.6 (2007). Publisher: John Wiley & Sons Ltd., pp. 381–392. ISSN: 0894-3214. DOI: 10.1002/pts.764.

[61] S P Singh and J Marcondes. “Vibration levels in commercial truck shipments as a function of suspension and payload”. In: *Journal of Testing and Evaluation* 20.6 (Nov. 1992). Publisher: Amer Soc Testing Materials, pp. 466–469. ISSN: 0090-3973.

[62] Paul A. Gagniuc. *Markov Chains: From Theory to Implementation and Experimentation*. Hoboken, NJ: John Wiley & Sons, 2017. ISBN: 978-1-119-38757-2 978-1-119-38758-9.

[63] Michael Havbro Faber. *Statistics and Probability Theory*. Vol. 18. Topics in Safety, Risk, Reliability and Quality. Dordrecht: Springer Netherlands, 2012. ISBN: 978-94-007-4055-6 978-94-007-4056-3. DOI: 10.1007/978-94-007-4056-3. URL: http://link.springer.com/10.1007/978-94-007-4056-3 (visited on 04/05/2021).

[64] D. A. Dickey and W. A. Fuller. “Likelihood Ratio Statistics for Autoregressive Time Series with a Unit Root”. In: *Econometrica* 49 (1981), pp. 1057–1072.

[65] Denis Kwiatkowski et al. “Testing the Null Hypothesis of Stationarity Against the Alternative of a Unit Root”. en. In: *Journal of Econometrics* 54.1-3 (Oct. 1992), pp. 159–178. ISSN: 03044076. DOI: 10.1016/0304-4076(92)90104-Y. URL: https://linkinghub.elsevier.com/retrieve/pii/030440769290104Y (visited on 04/05/2021).

[66] S. J. Leybourne and B. McCabe. “Modified Stationarity Tests with Data-Dependent Model-Selection Rules”. In: *Journal of Business and Economic Statistics* 17 (1999), pp. 264–270.

[67] Peter C. B. Phillips and Pierre Perron. “Testing for a Unit Root in Time Series Regression”. en. In: *Biometrika* 75.2 (1988), pp. 335–346. ISSN: 0006-3444, 1464-3510. DOI: 10.1093/biomet/75.2.335. URL: https://academic.oup.com/biomet/article-lookup/doi/10.1093/biomet/75.2.335 (visited on 04/05/2021).

[68] Andrew W. Lo and A. Craig MacKinlay. “Stock Market Prices Do Not Follow Random Walks: Evidence from a Simple Specification Test”. en. In: *Review of Financial Studies* 1.1 (Jan. 1988), pp. 41–66. ISSN: 0893-9454, 1465-7368. DOI: 10.1093/rfs/1.1.41. URL: https://academic.oup.com/rfs/article-lookup/doi/10.1093/rfs/1.1.41 (visited on 04/05/2021).

[69] Rudra Prakash Pradhan. “Variance Ratio Test of Random Walk for Foreign Trade: The Study in India During the Globalization Era of 1990s”. In: *International Journal of Financial Research* 3.1 (Jan. 2012), p101. ISSN: 1923-4031, 1923-4023. DOI: 10.5430/ijfr.v3n1p101. URL: http://www.sciedu.ca/journal/index.php/ijfr/article/view/714 (visited on 04/05/2021).

[70] F. N. David and S. Siegel. “Nonparametric Statistics for the Behavioral Sciences”. In: *Biometrika* 44.3/4 (Dec. 1957), p. 538. ISSN: 00063444. DOI: 10.2307/2332896. URL: https://www.jstor.org/stable/2332896?origin=crossref (visited on 04/05/2021).

[71] Martin Bilodeau et al. “Normality and Stationarity of EMG Signals of Elbow Flexor Muscles During Ramp and Step Isometric Contractions”. en. In: *Journal of Electromyography and Kinesiology* 7.2 (June 1997), pp. 87–96. ISSN: 10506411. DOI: 10.1016/S1050-6411(96)00024-7. URL: https://linkinghub.elsevier.com/retrieve/pii/S1050641196000247 (visited on 04/05/2021).

[72] Walter A. Shewhart and W. Edwards Deming. *Statistical Method from the Viewpoint of Quality Control*. New York: Dover, 1986. ISBN: 978-0-486-65232-0.

[73] Wayne Taylor A. *Change-Point Analysis: A Powerful New Tool for Detecting Changes*. en. Apr. 2000. URL: https://variation.com/change-point-analysis-a-powerful-new-tool-for-detecting-changes/ (visited on 03/06/2021).

[74] E. S. Page. “Continuous Inspection Schemes”. In: *Biometrika* 41.1/2 (June 1954), p. 100. ISSN: 00063444. DOI: 10.2307/2333009. URL: https://www.jstor.org/stable/2333009?origin=crossref (visited on 03/25/2021).

[75] E. S. Page. “A Test for a Change in a Parameter Occurring at an Unknown Point”. In: *Biometrika* 42.3/4 (Dec. 1955), p. 523. ISSN: 00063444. DOI: 10.2307/2333401. URL: https://www.jstor.org/stable/2333401?origin=crossref (visited on 03/25/2021).

[76] E. S. Page. “On problems in which a change in a parameter occurs at an unknown point”. en. In: *Biometrika* 44.1-2 (1957), pp. 248–252. ISSN: 0006-3444, 1464-3510. DOI: 10.1093/biomet/44.1-2.248. URL: https://academic.oup.com/biomet/article-lookup/doi/10.1093/biomet/44.1-2.248 (visited on 03/25/2021).

[77] Group The MathWorks Inc. *Audio Toolbox Reference Guide*. en. R2021a. Natick, MA: The MathWorks, Inc., 2021. URL: https://www.mathworks.com/help/pdf_doc/audio/audio_ref.pdf (visited on 04/17/2021).

[78] John M. Grey and John W. Gordon. “Perceptual Effects of Spectral Modifications on Musical Timbres”. en. In: *The Journal of the Acoustical Society of America* 63.5 (May 1978), pp. 1493–1500. ISSN: 0001-4966. DOI: 10.1121/1.381843. URL: http://asa.scitation.org/doi/10.1121/1.381843 (visited on 04/05/2021).

[79] Michał Kowalewski and Phil Novack-Gottshall. “Resampling Methods in Paleontology”. en. In: *The Paleontological Society Papers* 16 (Oct. 2010), pp. 19–54. ISSN: 1089-3326, 2399-7575. DOI: 10.1017/S1089332600001807. URL: https://www.cambridge.org/core/product/identifier/S1089332600001807/type/journal_article (visited on 01/03/2021).

[80] *MIL-STD-810H Test Method Standard: Environmental Engineering Considerations and Laboratory Tests*. The US Department of Defense, 2019.

[81] Travis W. Beck et al. “An Examination of the Runs Test, Reverse Arrangements Test, and Modified Reverse Arrangements Test for Assessing Surface Emg Signal Stationarity”. en. In: *Journal of Neuroscience Methods* 156.1-2 (Sept. 2006), pp. 242–248. ISSN: 01650270. DOI: 10.1016/j.jneumeth.2006.03.011. URL: https://linkinghub.elsevier.com/retrieve/pii/S0165027006001506 (visited on 04/05/2021).

[82] V. Rouillard. “Quantifying the Non-stationarity of Vehicle Vibrations with the Run Test”. en. In: *Packaging Technology and Science* 27.3 (Mar. 2014), pp. 203–219. ISSN: 08943214. DOI: 10.1002/pts.2024. URL: http://doi.wiley.com/10.1002/pts.2024 (visited on 12/28/2020).

[83] Ben Bruscella, Vincent Rouillard, and Michael Sek. “Analysis of road surface profiles”. en. In: *Journal of Transportation Engineering* 125.1 (Jan. 1999), pp. 55–59. ISSN: 0733-947X, 1943-5436. DOI: 10.1061/(ASCE)0733-947X(1999)125:1(55). URL: http://ascelibrary.org/doi/10.1061/%28ASCE%290733-947X%281999%29125%3A1%2855%29 (visited on 02/28/2021).

[84] Julien Lepine. “An optimised machine learning algorithm for detecting shocks in road vehicle vibration”. PhD thesis. 2016.

[85] Ben Bruscella. “Analysis and Simulation of the Spectral and Statistical Properties of Road Roughness for Package Performance Testing”. Master of Engineering in Mechanical Engineering. Victoria: Victoria University of Technology, 1997.

[86] Vincent Rouillard, Ben Bruscella, and Michael Sek. “Classification of road surface profiles”. en. In: *Journal of Transportation Engineering* 126.1 (Jan. 2000), pp. 41–45. ISSN: 0733-947X, 1943-5436. DOI: 10.1061/(ASCE)0733-947X(2000)126:1(41). URL: http://ascelibrary.org/doi/10.1061/%28ASCE%290733-947X%282000%29126%3A1%2841%29 (visited on 12/28/2020).

[87] Hao Zhou and Zhi-Wei Wang. “A new approach for road-vehicle vibration simulation: a new approach for road-vehicle vibration simulation”. en. In: *Packaging Technology and Science* 31.5 (May 2018), pp. 246–260. ISSN: 08943214. DOI: 10.1002/pts.2310. URL: http://doi.wiley.com/10.1002/pts.2310 (visited on 02/28/2021).

[88] Hao Zhou and Zhi-Wei Wang. “Comparison study on simulation effect of improved simulation methods for packaging random vibration test”. en. In: *Packaging Technology and Science* 32.3 (Mar. 2019), pp. 119–131. ISSN: 08943214. DOI: 10.1002/pts.2421. URL: http://doi.wiley.com/10.1002/pts.2421 (visited on 02/28/2021).

[89] Raouf A. Ibrahim. *Handbook of Structural Life Assessment*. en. Chichester, UK: John Wiley & Sons, Ltd, Mar. 2017. ISBN: 978-1-119-13547-0 978-1-119-13546-3. DOI: 10.1002/9781119135470. URL: http://doi.wiley.com/10.1002/9781119135470 (visited on 02/28/2021).

[90] Fridtjof Thomas. “Automated Road Segmentation Using a Bayesian Algorithm”. en. In: *Journal of Transportation Engineering* 131.8 (Aug. 2005), pp. 591–598. ISSN: 0733-947X, 1943-5436. DOI: 10.1061/(ASCE)0733-947X(2005)131:8(591). URL: http://ascelibrary.org/doi/10.1061/%28ASCE%290733-947X%282005%29131%3A8%28591%29 (visited on 12/30/2020).

[91] Darrel Charles. “Derivation of environment descriptions and test severities from measured road transportation data”. en. In: *Journal of the IEST* 36.1 (Jan. 1993), pp. 37–42. ISSN: 1052-2883. DOI: 10.17764/jiet.2.36.1.k285j24551552377. URL: https://meridian.allenpress.com/jiest/article/36/1/37/186811/Derivation-of-Environment-Descriptions-and-Test (visited on 12/28/2020).

[92] Vincent Rouillard. “On the Non-Gaussian Nature of Random Vehicle Vibrations”. In: vol. II. World Congress on Engineering, WCE 2007. London: WCE, 2007. ISBN: 978-988-98671-2-6.

[93] Michael A. Sek. “A modern technique of transportation simulation for package performance testing”. en. In: *Packaging Technology and Science* 9.6 (Nov. 1996), pp. 327–343. ISSN: 08943214, 10991522. DOI: 10.1002/pts.2770090604. URL: http://doi.wiley.com/10.1002/pts.2770090604 (visited on 12/27/2020).

[94] V. Rouillard and M. A. Sek. “Monitoring and simulating non-stationary vibrations for package optimization”. en. In: *Packaging Technology and Science* 13.4 (July 2000). Publisher: John Wiley & Sons, Ltd, pp. 149–156. ISSN: 1099-1522. DOI: 10.1002/1099-1522(200007)13:4<149::AID-PTS508>3.0.CO;2-A. URL: https://onlinelibrary.wiley.com/doi/10.1002/1099-1522(200007)13:4%3C149::AID-PTS508%3E3.0.CO;2-A (visited on 12/28/2020).

[95] V. Rouillard and M. A. Sek. “Statistical modelling of predicted non-stationary vehicle vibrations”. en. In: *Packaging Technology and Science* 15.2 (Mar. 2002), pp. 93–101. ISSN: 0894-3214, 1099-1522. DOI: 10.1002/pts.573. URL: http://doi.wiley.com/10.1002/pts.573 (visited on 12/28/2020).

[96] Vincent Rouillard. “On the statistical distribution of stationary segment lengths of road vehicles vibrations”. en. In: *Proceedings of the World Congress on Engineering.* Vol. II. London, Feb. 2007. ISBN: 978-988-98671-2-6.

[97] Vincent Rouillard. “On the synthesis of non-Gaussian road vehicle vibrations”. File under permanent embargo. PhD thesis. 2007. URL: https://bridges.monash.edu/articles/thesis/On_the_synthesis_of_non-Gaussian_road_vehicle_vibrations/5309899 (visited on 12/28/2020).

[98] Vincent Rouillard. “The Synthesis of Road Vehicle Vibrations Based on the Statistical Distribution of Segment Lengths”. en. In: *5th Australasian Congress on Applied Mechanics.* Brisbane, Australia, Dec. 2007.

[99] Vincent Rouillard. “Statistical Models for Nonstationary and Non-Gaussian Road Vehicle Vibrations”. en. In: *Engineering Letters* 17.4 (2009). URL: http://www.engineeringletters.com/issues_v17/issue_4/EL_17_4_03.pdf.

[100] Liu Wei, T. F. Fwa, and Zhao Zhe. “Wavelet Analysis and Interpretation of Road Roughness”. en. In: *Journal of Transportation Engineering* 131.2 (Feb. 2005), pp. 120–130. ISSN: 0733-947X, 1943-5436. DOI: 10.1061/(ASCE)0733-947X(2005)131:2(120). URL: http://ascelibrary.org/doi/10.1061/%28ASCE%290733-947X%282005%29131%3A2%28120%29 (visited on 12/30/2020).

[101] Vincent Rouillard and Robert Richmond. “A Novel Approach to Analysing and Simulating Railcar Shock and Vibrations”. en. In: *Packaging Technology and Science* 20.1 (Jan. 2007), pp. 17–26. ISSN: 08943214, 10991522. DOI: 10.1002/pts.739. URL: http://doi.wiley.com/10.1002/pts.739 (visited on 12/28/2020).

[102] Vincent Rouillard and Michael A. Sek. “The Use of Intrinsic Mode Functions to Characterize Shock and Vibration in the Distribution Environment”. en. In: *Packaging Technology and Science* 18.1 (Jan. 2005), pp. 39–51. ISSN: 0894-3214, 1099-1522. DOI: 10.1002/pts.677. URL: http://doi.wiley.com/10.1002/pts.677 (visited on 12/28/2020).

[103] Katharine Rhiannon Griffiths. “Improved Method for Simulation of Vehicle Vibration Using a Journey Database and Wavelet Analysis for the Pre-Distribution Testing of Packaging”. PhD thesis. University of Bath, Oct. 2012.

[104] K.R. Griffiths et al. “Wavelet Analysis to Decompose a Vibration Simulation Signal to Improve Pre-Distribution Testing of Packaging”. en. In: *Mechanical Systems and Signal Processing* 76-77 (Aug. 2016), pp. 780–795. ISSN: 08883270. DOI: 10.1016/j.ymssp.2015.12.035. URL: https://linkinghub.elsevier.com/retrieve/pii/S0888327015006007 (visited on 12/30/2020).

[105] Chao Mao et al. “Modeling and Simulation of Non-Stationary Vehicle Vibration Signals Based on Hilbert Spectrum”. en. In: *Mechanical Systems and Signal Processing* 50-51 (Jan. 2015), pp. 56–69. ISSN: 08883270. DOI: 10.1016/j.ymssp.2014.05.005. URL: https://linkinghub.elsevier.com/retrieve/pii/S0888327014001344 (visited on 02/28/2021).

[106] Julien Lepine and Vincent Rouillard. “Evaluation of shock detection algorithm for road vehicle vibration analysis”. en. In: *Vibration* 1.2 (Oct. 2018), pp. 220–238. ISSN: 2571-631X. DOI: 10.3390/vibration1020016. URL: http://www.mdpi.com/2571-631X/1/2/16 (visited on 12/28/2020).

[107] Neil Salkind. *Encyclopedia of Research Design*. 2455 Teller Road, Thousand Oaks California 91320 United States: SAGE Publications, Inc., 2010. ISBN: 978-1-4129-6127-1. DOI: 10.4135/9781412961288.

[108] David S Moore. *The Basic Practice of Statistics*. Fifth. New York: W. H. Freeman and Company, 2010. ISBN: 978-1-4292-0121-6.

[109] Hae-Young Kim. “Statistical notes for clinical researchers: post-hoc multiple comparisons”. In: *Restorative Dentistry & Endodontics* 40.2 (2015), p. 172. ISSN: 2234-7658. DOI: 10.5395/rde.2015.40.2.172.

[110] Tom Irvine. *Vibrationdata.com*. Publication Title: August 2004 Newsletter. 2004.

[111] Inc. The MathWorks. *MATLAB 9.5.0. (R2018b)*. Publisher: The MathWorks Inc. Natick, Massachusetts, 2020.

[112] Jean Dickinson Gibbons and Subhabrata Chakraborti. *Nonparametric Statistical Inference, Fourth Edition: Revised and Expanded*. 4th ed. New York: Marcel Dekker, Inc., 2003. ISBN: 0-8247-4052-1.

[113] David M. Lane. *Introduction to Statistics*. Online Edi. (1) Rice University, (2) University of Houston, Downtown Campus, 0.

[114] Shi Yi Chen, Zhe Feng, and Xiaolian Yi. “A general introduction to adjustment for multiple comparisons”. In: *Journal of Thoracic Disease* 9.6 (2017), pp. 1725–1729. ISSN: 20776624. DOI: 10.21037/jtd.2017.05.34.

[115] C. E. Bonferroni. “Teoria statistica delle classi e calcolo delle probabilità”. In: *Pubblicazioni del R Istituto Superiore di Scienze Economiche e Commerciali di Firenze* (1936).

[116] Sture Holm. “A Simple Sequentially Rejective Multiple Test Procedure”. In: *Scandinavian Journal of Statistics* 6.2 (1979), pp. 65–70.

[117] Sangseok Lee and Dong Kyu Lee. “What is the proper way to apply the multiple comparison test?” In: *Korean Journal of Anesthesiology* 71.5 (2018), pp. 353–360. ISSN: 20057563. DOI: 10.4097/kja.d.18.00242.

[118] B. L. Welch. “The generalization of ‘Student’s’ problem when several different population varlances are involved”. en. In: *Biometrika* 34.1-2 (1947), pp. 28–35. ISSN: 0006-3444, 1464-3510. DOI: 10.1093/biomet/34.1-2.28.

[119] William F. Guthrie. “NIST/SEMATECH e-Handbook of Statistical Methods (NIST Handbook 151)”. en. In: (2020). Publisher: National Institute of Standards and Technology. URL: https://www.itl.nist.gov/div898/handbook/.

[120] Inc. The MathWorks. *Statistics toolbox: for use with Matlab*. The MathWorks, Inc, July 2005.

[121] Harvey Motulsky. *Intuitive biostatistics: a nonmathematical guide to statistical thinking*. Fourth edition. New York: Oxford University Press, 2018. ISBN: 978-0-19-064356-0.

[122] Wendy L Martinez and Angel R Martinez. *Computational Statistics Handbook with MATLAB, Third Edition*. English. OCLC: 1058841318. 2015. ISBN: 978-1-4665-9274-2. URL: https://ebookcentral.proquest.com/lib/qut/detail.action?docID=5345267 (visited on 01/03/2022).

[123] Richard A. Armstrong. “When to use the Bonferroni correction”. en. In: *Ophthalmic and Physiological Optics* 34.5 (Sept. 2014), pp. 502–508. ISSN: 02755408. DOI: 10.1111/opo.12131. URL: https://onlinelibrary.wiley.com/doi/10.1111/opo.12131 (visited on 01/03/2022).

[124] Ilker Unal. “Defining an Optimal Cut-Point Value in ROC Analysis: An Alternative Approach”. en. In: *Computational and Mathematical Methods in Medicine* 2017 (2017), pp. 1–14. ISSN: 1748-670X, 1748-6718. DOI: 10.1155/2017/3762651. URL: https://www.hindawi.com/journals/cmmm/2017/3762651/ (visited on 01/03/2022).

[125] Rakesh Aggarwal and Priya Ranganathan. “Understanding diagnostic tests – Part 3: Receiver operating characteristic curves”. en. In: *Perspectives in Clinical Research* 9.3 (2018), p. 145. ISSN: 2229-3485. DOI: 10.4103/picr.PICR_87_18. URL: http://www.picronline.org/text.asp?2018/9/3/145/236486 (visited on 01/04/2022).

[126] Alexander Steinwolf. “Random Vibration Testing Beyond PSD Limitations”. en. In: *Sound and Vibration* 40.Dynamic Testing Reference Issue (2006), pp. 12–21.

[127] Philip D. Van Baren. “System and Method for Simultaneously Controlling Spectrum and Kurtosis of a Random Vibration”. US 2007/0185620 A1 (Wyoming, MI (US)).

[128] Philip Van Baren. “The Missing Knob on Your Random Vibration Controller”. In: *Sound and Vibration* October.Dynamic Testing Reference Issue (2005), pp. 2–7.

[129] David O Smallwood. “Generating Non-Gaussian Vibration for Testing Purposes”. en. In: *Sound and Vibration* October (2005), pp. 18–24.

[130] Brian Wallin. “Developing a Random Vibration”. In: *IAPRI Symposium*. East Lansing, MI: International Safe Transit Association, 2007, pp. 42–54.

[131] William I Kipp. “Random Vibration Testing of Packaged-Products: Considerations for Methodology Improvement”. In: Bangkok, Thailand, June 2008, pp. 1–12.

[132] V. Rouillard and M. A. Sek. “Synthesizing Nonstationary, Non-Gaussian Random Vibrations”. en. In: *Packaging Technology and Science* 23.8 (Dec. 2010), pp. 423–439. ISSN: 08943214. DOI: 10.1002/pts.907. URL: http://doi.wiley.com/10.1002/pts.907 (visited on 12/28/2020).

[133] Vincent Rouillard and Michael Sek. “Creating Transport Vibration Simulation Profiles from Vehicle and Road Characteristics”. en. In: *Packaging Technology and Science* 26.2 (Mar. 2013), pp. 82–95. ISSN: 08943214. DOI: 10.1002/pts.1967. URL: http://doi.wiley.com/10.1002/pts.1967 (visited on 12/28/2020).

[134] Mao Chao et al. “Synthesis of severely non-stationary vehicle vibration signals based on Higher-order moments and Hilbert spectrum”. en. In: *Mechanical Systems and Signal Processing* 164 (Feb. 2022), p. 108238. ISSN: 08883270. DOI: 10.1016/j.ymssp.2021.108238. URL: https://linkinghub.elsevier.com/retrieve/pii/S0888327021006105 (visited on 04/13/2022).

[135] Hwanpyo Kim and Michael D. Shields. “Modeling strongly non-Gaussian non-stationary stochastic processes using the Iterative Translation Approximation Method and Karhunen–Loève expansion”. en. In: *Computers & Structures* 161 (Dec. 2015), pp. 31–42. ISSN: 00457949. DOI: 10.1016/j.compstruc.2015.08.010. URL: https://linkinghub.elsevier.com/retrieve/pii/S0045794915002370 (visited on 04/13/2022).

[136] Ming-Na Tong, Yan-Gang Zhao, and Zhao Zhao. “Simulating strongly non-Gaussian and non-stationary processes using Karhunen–Loève expansion and L-moments-based Hermite polynomial model”. en. In: *Mechanical Systems and Signal Processing* 160 (Nov. 2021), p. 107953. ISSN: 08883270. DOI: 10.1016/j.ymssp.2021.107953. URL: https://linkinghub.elsevier.com/retrieve/pii/S0888327021003484 (visited on 04/13/2022).

[137] Ronghui Zheng et al. “Multiple-input multiple-output non-stationary non-Gaussian random vibration control by inverse system method”. en. In: *Mechanical Systems and Signal Processing* 124 (June 2019), pp. 124–141. ISSN: 08883270. DOI: 10.1016/j.ymssp.2019.01.055. URL: https://linkinghub.elsevier.com/retrieve/pii/S0888327019300718 (visited on 04/13/2022).

[138] Manuel-Alfredo Garcia-Romeu-Martinez, Vincent Rouillard, and Vicente-Agustin Cloquell-Ballester. “A Model for the Statistical Distribution of Road Vehicle Vibrations”. en. In: (2007), p. 6.

[139] A. K. Jain, M. N. Murty, and P. J. Flynn. “Data clustering: a review”. en. In: *ACM Computing Surveys* 31.3 (Sept. 1999), pp. 264–323. ISSN: 0360-0300, 1557-7341. DOI: 10.1145/331499.331504. URL: https://dl.acm.org/doi/10.1145/331499.331504 (visited on 10/10/2021).

[140] Peter J. Rousseeuw. “Silhouettes: A graphical aid to the interpretation and validation of cluster analysis”. en. In: *Journal of Computational and Applied Mathematics* 20 (Nov. 1987), pp. 53–65. ISSN: 03770427. DOI: 10.1016/0377-0427(87)90125-7. URL: https://linkinghub.elsevier.com/retrieve/pii/0377042787901257 (visited on 10/10/2021).

[141] Christian Hennig et al., eds. *Handbook of Cluster Analysis*. en. 0th ed. Chapman and Hall/CRC, Dec. 2015. ISBN: 978-0-429-18547-2. DOI: 10.1201/b19706. URL: https://www.taylorfrancis.com/books/9781466551893 (visited on 10/10/2021).

[142] T. Calinski and J. Harabasz. “A dendrite method for cluster analysis”. en. In: *Communications in Statistics - Theory and Methods* 3.1 (1974), pp. 1–27. ISSN: 0361-0926. DOI: 10.1080/03610927408827101. URL: http://www.tandfonline.com/doi/abs/10.1080/03610927408827101 (visited on 10/10/2021).

[143] J. C. Dunn. “Well-Separated Clusters and Optimal Fuzzy Partitions”. en. In: *Journal of Cybernetics* 4.1 (Jan. 1974), pp. 95–104. ISSN: 0022-0280. DOI: 10.1080/01969727408546059. URL: https://www.tandfonline.com/doi/full/10.1080/01969727408546059 (visited on 10/10/2021).

[144] Leonard Kaufman and Peter J. Rousseeuw. *Finding groups in data: an introduction to cluster analysis*. Wiley series in probability and mathematical statistics. Hoboken, N.J: Wiley, 2005. ISBN: 978-0-471-73578-6.

[145] Maria Halkidi and Michalis Vazirgiannis. “A density-based cluster validity approach using multi-representatives”. en. In: *Pattern Recognition Letters* 29.6 (Apr. 2008), pp. 773–786. ISSN: 01678655. DOI: 10.1016/j.patrec.2007.12.011. URL: https://linkinghub.elsevier.com/retrieve/pii/S0167865508000020 (visited on 10/10/2021).

[146] Yanchi Liu et al. “Understanding and Enhancement of Internal Clustering Validation Measures”. In: *IEEE Transactions on Cybernetics* 43.3 (June 2013), pp. 982–994. ISSN: 2168-2267, 2168-2275. DOI: 10.1109/TSMCB.2012.2220543. URL: http://ieeexplore.ieee.org/document/6341117/ (visited on 10/10/2021).

[147] Bernard Desgraupes. *Clustering Indices: Package clusterCrit for R.* URL: https://cran.r-project.org/web/packages/clusterCrit/vignettes/clusterCrit.pdf (visited on 10/10/2021).

[148] Inc The MathWorks. *Statistics and Machine Learning Toolbox User's Guide.* R2020a. Natick, MA: The MathWorks, Inc., 2020.

[149] Georg Peters et al. "Soft clustering – Fuzzy and rough approaches and their extensions and derivatives". en. In: *International Journal of Approximate Reasoning* 54.2 (Feb. 2013), pp. 307–322. ISSN: 0888613X. DOI: 10.1016/j.ijar.2012.10.003. URL: https://linkinghub.elsevier.com/retrieve/pii/S0888613X12001739 (visited on 10/12/2021).

***